High transverse momentum η meson production in $p+p$, $d+$Au, and Au+Au collisions at $\sqrt{s_{NN}} = 200$ GeV

S. S. Adler,[5] S. Afanasiev,[20] C. Aidala,[5,10] N. N. Ajitanand,[47] Y. Akiba,[23,42] J. Alexander,[47] A. Al-Jamel,[37] R. Amirikas,[14] K. Aoki,[27] L. Aphecetche,[49] R. Armendariz,[37] S. H. Aronson,[5] R. Averbeck,[48] T. C. Awes,[38] R. Azmoun,[48] V. Babintsev,[17] A. Baldisseri,[11] K. N. Barish,[6] P. D. Barnes,[30] B. Bassalleck,[36] S. Bathe,[6,33] S. Batsouli,[10] V. Baublis,[41] F. Bauer,[6] A. Bazilevsky,[5,17,43] S. Belikov,[17,19] Y. Berdnikov,[44] S. Bhagavatula,[19] M. T. Bjorndal,[10] J. G. Boissevain,[30] H. Borel,[11] S. Borenstein,[28] M. L. Brooks,[30] D. S. Brown,[37] N. Bruner,[36] D. Bucher,[33] H. Buesching,[5,33] V. Bumazhnov,[17] G. Bunce,[5,43] J. M. Burward-Hoy,[29,30,48] S. Butsyk,[48] X. Camard,[49] J.-S. Chai,[21] P. Chand,[4] W. C. Chang,[2] S. Chernichenko,[17] J. Chiba,[23] C. Y. Chi,[10] M. Chiu,[10] I. J. Choi,[56] J. Choi,[22] R. K. Choudhury,[4] T. Chujo,[5] V. Cianciolo,[38] Y. Cobigo,[11] B. A. Cole,[10] M. P. Comets,[39] P. Constantin,[19] M. Csanád,[13] T. Csörgő,[24] J. P. Cussonneau,[49] K. Das,[14] G. David,[5] F. Deák,[13] H. Delagrange,[49] A. Denisov,[17] D. d'Enterria,[10,49] A. Deshpande,[43] E. J. Desmond,[5] A. Devismes,[48] O. Dietzsch,[45] J. L. Drachenberg,[1] O. Drapier,[28] A. Drees,[48] K. A. Drees,[5] R. duRietz,[32] A. Durum,[17] D. Dutta,[4] V. Dzhordzhadze,[50] Y. V. Efremenko,[38] K. El Chenawi,[53] A. Enokizono,[16] H. En'yo,[42,43] B. Espagnon,[39] S. Esumi,[52] L. Ewell,[5] D. E. Fields,[36,43] C. Finck,[49] F. Fleuret,[28] S. L. Fokin,[26] B. D. Fox,[43] Z. Fraenkel,[55] J. E. Frantz,[10] A. Franz,[5] A. D. Frawley,[14] Y. Fukao,[27,42,43] S.-Y. Fung,[6] S. Gadrat,[31] S. Garpman,[32,*] M. Germain,[49] T. K. Ghosh,[53] A. Glenn,[50] G. Gogiberidze,[50] M. Gonin,[28] J. Gosset,[11] Y. Goto,[42,43] R. Granier de Cassagnac,[28] N. Grau,[19] S. V. Greene,[53] M. Grosse Perdekamp,[18,43] W. Guryn,[5] H.-Å. Gustafsson,[32] T. Hachiya,[16] J. S. Haggerty,[5] H. Hamagaki,[8] A. G. Hansen,[30] E. P. Hartouni,[29] M. Harvey,[5] K. Hasuko,[42] R. Hayano,[8] N. Hayashi,[42] M. Heffner,[29] T. K. Hemmick,[48] J. M. Heuser,[42,48] X. He,[15] M. Hibino,[54] P. Hidas,[24] H. Hiejima,[18] J. C. Hill,[19] R. Hobbs,[36] W. Holzmann,[47] K. Homma,[16] B. Hong,[25] A. Hoover,[37] T. Horaguchi,[42,43,51] T. Ichihara,[42,43] V. V. Ikonnikov,[26] K. Imai,[27,42] M. Inaba,[52] M. Inuzuka,[8] D. Isenhower,[1] L. Isenhower,[1] M. Ishihara,[42] M. Issah,[47] A. Isupov,[20] B. V. Jacak,[48] W. Y. Jang,[25] Y. Jeong,[22] J. Jia,[48] O. Jinnouchi,[42,43] B. M. Johnson,[5] S. C. Johnson,[29] K. S. Joo,[34] D. Jouan,[39] F. Kajihara,[8] S. Kametani,[8,54] N. Kamihara,[42,51] M. Kaneta,[43] J. H. Kang,[56] S. S. Kapoor,[4] K. Katou,[54] M. Kaufman,[10] T. Kawabata,[8] A. V. Kazantsev,[26] S. Kelly,[9,10] B. Khachaturov,[55] A. Khanzadeev,[41] J. Kikuchi,[54] D. H. Kim,[34] D. J. Kim,[56] D. W. Kim,[22] E. Kim,[46] G.-B. Kim,[28] H. J. Kim,[56] E. Kinney,[9] A. Kiss,[13] E. Kistenev,[5] A. Kiyomichi,[42,52] K. Kiyoyama,[35] C. Klein-Boesing,[33] H. Kobayashi,[42,43] L. Kochenda,[41] V. Kochetkov,[17] D. Koehler,[36] T. Kohama,[16] R. Kohara,[16] B. Komkov,[41] M. Konno,[52] M. Kopytine,[48] D. Kotchetkov,[6] A. Kozlov,[55] P. J. Kroon,[5] C. H. Kuberg,[1,*] G. J. Kunde,[30] K. Kurita,[42,43] Y. Kuroki,[52] M. J. Kweon,[25] Y. Kwon,[56] G. S. Kyle,[37] R. Lacey,[47] V. Ladygin,[20] J. G. Lajoie,[19] A. Lebedev,[19,26] Y. Le Bornec,[39] S. Leckey,[48] D. M. Lee,[30] S. Lee,[22] M. J. Leitch,[30] M. A. L. Leite,[45] H. Lim,[46] A. Litvinenko,[20] M. X. Liu,[30] Y. Liu,[39] X. H. Li,[6] C. F. Maguire,[53] Y. I. Makdisi,[5] A. Malakhov,[20] V. I. Manko,[26] Y. Mao,[7,40,42] G. Martinez,[49] M. D. Marx,[48] H. Masui,[52] F. Matathias,[48] T. Matsumoto,[8,54] M. C. McCain,[1] P. L. McGaughey,[30] E. Melnikov,[17] F. Messer,[48] Y. Miake,[52] J. Milan,[47] T. E. Miller,[53] A. Milov,[48,55] S. Mioduszewski,[5] R. E. Mischke,[30] G. C. Mishra,[15] J. T. Mitchell,[5] A. K. Mohanty,[4] D. P. Morrison,[5] J. M. Moss,[30] F. Mühlbacher,[48] D. Mukhopadhyay,[55] M. Muniruzzaman,[6] J. Murata,[42,43] S. Nagamiya,[23] J. L. Nagle,[9,10] T. Nakamura,[16] B. K. Nandi,[6] M. Nara,[52] J. Newby,[50] P. Nilsson,[32] A. S. Nyanin,[26] J. Nystrand,[32] E. O'Brien,[5] C. A. Ogilvie,[19] H. Ohnishi,[5,42] I. D. Ojha,[3,53] H. Okada,[27,42] K. Okada,[42,43] M. Ono,[52] V. Onuchin,[17] A. Oskarsson,[32] I. Otterlund,[32] K. Oyama,[8] K. Ozawa,[8] D. Pal,[55] A. P. T. Palounek,[30] V. Pantuev,[48] V. Papavassiliou,[37] J. Park,[46] W. J. Park,[25] A. Parmar,[36] S. F. Pate,[37] H. Pei,[19] T. Peitzmann,[33] V. Penev,[20] J.-C. Peng,[18,30] H. Pereira,[11] V. Peresedov,[20] A. Pierson,[36] C. Pinkenburg,[5] R. P. Pisani,[5] F. Plasil,[38] M. L. Purschke,[5] A. K. Purwar,[48] J. M. Qualls,[1] J. Rak,[19] I. Ravinovich,[55] K. F. Read,[38,50] M. Reuter,[48] K. Reygers,[33] V. Riabov,[41,44] Y. Riabov,[41] G. Roche,[31] A. Romana,[28,*] M. Rosati,[19] S. S. E. Rosendahl,[32] P. Rosnet,[31] V. L. Rykov,[42] S. S. Ryu,[56] M. E. Sadler,[1] B. Sahlmueller,[33] N. Saito,[27,42,43] T. Sakaguchi,[8,54] M. Sakai,[35] S. Sakai,[52] V. Samsonov,[41] L. Sanfratello,[36] R. Santo,[33] H. D. Sato,[27,42] S. Sato,[5,52] S. Sawada,[23] Y. Schutz,[49] V. Semenov,[17] R. Seto,[6] M. R. Shaw,[1,30] T. K. Shea,[5] I. Shein,[17] T.-A. Shibata,[42,51] K. Shigaki,[16,23] T. Shiina,[30] M. Shimomura,[52] A. Sickles,[48] C. L. Silva,[45] D. Silvermyr,[30,32] K. S. Sim,[25] C. P. Singh,[3] V. Singh,[3] M. Sivertz,[5] A. Soldatov,[17] R. A. Soltz,[29] W. E. Sondheim,[30] S. P. Sorensen,[50] I. V. Sourikova,[5] F. Staley,[11] P. W. Stankus,[38] E. Stenlund,[32] M. Stepanov,[37] A. Ster,[24] S. P. Stoll,[5] T. Sugitate,[16] J. P. Sullivan,[30] S. Takagi,[52] E. M. Takagui,[45] A. Taketani,[42,43] M. Tamai,[54] K. H. Tanaka,[23] Y. Tanaka,[35] K. Tanida,[42] M. J. Tannenbaum,[5] A. Taranenko,[47] P. Tarján,[12] J. D. Tepe,[1,30] T. L. Thomas,[36] M. Togawa,[27,42] J. Tojo,[27,42] H. Torii,[27,42,43] R. S. Towell,[1] V.-N. Tram,[28] I. Tserruya,[55] Y. Tsuchimoto,[16] H. Tsuruoka,[52] S. K. Tuli,[3] H. Tydesjö,[32] N. Tyurin,[17] T. J. Uam,[34] H. W. van Hecke,[30] J. Velkovska,[5,48] M. Velkovsky,[48] V. Veszprémi,[12] L. Villatte,[50] A. A. Vinogradov,[26] M. A. Volkov,[26] E. Vznuzdaev,[41] X. R. Wang,[15] Y. Watanabe,[42,43] S. N. White,[5] N. Willis,[39] F. K. Wohn,[19] C. L. Woody,[5] W. Xie,[6] Y. Yang,[7] A. Yanovich,[17] S. Yokkaichi,[42,43] G. R. Young,[38] I. E. Yushmanov,[26] W. A. Zajc,[10,†] C. Zhang,[10] S. Zhou,[7] S. J. Zhou,[55] J. Zimányi,[24,*] L. Zolin,[20] and X. Zong[19]

(PHENIX Collaboration)

[1]*Abilene Christian University, Abilene, Texas 79699, USA*

[2]*Institute of Physics, Academia Sinica, Taipei 11529, Taiwan*

[3]*Department of Physics, Banaras Hindu University, Varanasi 221005, India*

[4]*Bhabha Atomic Research Centre, Bombay 400 085, India*

[5]*Brookhaven National Laboratory, Upton, New York 11973-5000, USA*

[6]*University of California-Riverside, Riverside, California 92521, USA*

[7]*China Institute of Atomic Energy (CIAE), Beijing, People's Republic of China*
[8]*Center for Nuclear Study, Graduate School of Science, University of Tokyo, 7-3-1 Hongo, Bunkyo, Tokyo 113-0033, Japan*
[9]*University of Colorado, Boulder, Colorado 80309, USA*
[10]*Columbia University, New York, NY 10027 and Nevis Laboratories, Irvington, New York 10533, USA*
[11]*Dapnia, CEA Saclay, F-91191, Gif-sur-Yvette, France*
[12]*Debrecen University, H-4010 Debrecen, Egyetem tér 1, Hungary*
[13]*ELTE, Eötvös Loránd University, H-1117 Budapest, Pázmány P. s. 1/A, Hungary*
[14]*Florida State University, Tallahassee, Florida 32306, USA*
[15]*Georgia State University, Atlanta, Georgia 30303, USA*
[16]*Hiroshima University, Kagamiyama, Higashi-Hiroshima 739-8526, Japan*
[17]*IHEP Protvino, State Research Center of Russian Federation, Institute for High Energy Physics, Protvino, RU-142281, Russia*
[18]*University of Illinois at Urbana-Champaign, Urbana, IL 61801, USA*
[19]*Iowa State University, Ames, Iowa 50011, USA*
[20]*Joint Institute for Nuclear Research, RU-141980 Dubna, Moscow Region, Russia*
[21]*KAERI, Cyclotron Application Laboratory, Seoul, South Korea*
[22]*Kangnung National University, Kangnung 210-702, South Korea*
[23]*KEK, High Energy Accelerator Research Organization, Tsukuba, Ibaraki 305-0801, Japan*
[24]*KFKI Research Institute for Particle and Nuclear Physics of the Hungarian Academy of Sciences (MTA KFKI RMKI), H-1525 Budapest 114, P. O. Box 49, Budapest, Hungary*
[25]*Korea University, Seoul, 136-701, Korea*
[26]*Russian Research Center "Kurchatov Institute," Moscow, Russia*
[27]*Kyoto University, Kyoto 606-8502, Japan*
[28]*Laboratoire Leprince-Ringuet, Ecole Polytechnique, CNRS-IN2P3, Route de Saclay, F-91128, Palaiseau, France*
[29]*Lawrence Livermore National Laboratory, Livermore, California 94550, USA*
[30]*Los Alamos National Laboratory, Los Alamos, New Mexico 87545, USA*
[31]*LPC, Université Blaise Pascal, CNRS-IN2P3, Clermont-Fd, F-63177 Aubiere Cedex, France*
[32]*Department of Physics, Lund University, Box 118, SE-221 00 Lund, Sweden*
[33]*Institut für Kernphysik, University of Muenster, D-48149 Muenster, Germany*
[34]*Myongji University, Yongin, Kyonggido 449-728, Korea*
[35]*Nagasaki Institute of Applied Science, Nagasaki-shi, Nagasaki 851-0193, Japan*
[36]*University of New Mexico, Albuquerque, New Mexico 87131, USA*
[37]*New Mexico State University, Las Cruces, New Mexico 88003, USA*
[38]*Oak Ridge National Laboratory, Oak Ridge, Tennessee 37831, USA*
[39]*IPN-Orsay, Universite Paris Sud, CNRS-IN2P3, BP1, F-91406, Orsay, France*
[40]*Peking University, Beijing, People's Republic of China*
[41]*PNPI, Petersburg Nuclear Physics Institute, Gatchina, Leningrad region, RU-188300, Russia*
[42]*RIKEN (The Institute of Physical and Chemical Research), Wako, Saitama 351-0198, JAPAN*
[43]*RIKEN BNL Research Center, Brookhaven National Laboratory, Upton, New York 11973-5000, USA*
[44]*Saint Petersburg State Polytechnic University, St. Petersburg, Russia*
[45]*Universidade de São Paulo, Instituto de Física, Caixa Postal 66318, São Paulo CEP05315-970, Brazil*
[46]*System Electronics Laboratory, Seoul National University, Seoul, South Korea*
[47]*Chemistry Department, Stony Brook University, Stony Brook, SUNY, New York 11794-3400, USA*
[48]*Department of Physics and Astronomy, Stony Brook University, SUNY, Stony Brook, New York 11794, USA*
[49]*SUBATECH (Ecole des Mines de Nantes, CNRS-IN2P3, Université de Nantes) BP 20722, F-44307, Nantes, France*
[50]*University of Tennessee, Knoxville, Tennesee 37996, USA*
[51]*Department of Physics, Tokyo Institute of Technology, Oh-okayama, Meguro, Tokyo 152-8551, Japan*
[52]*Institute of Physics, University of Tsukuba, Tsukuba, Ibaraki 305, Japan*
[53]*Vanderbilt University, Nashville, Tennessee 37235, USA*
[54]*Waseda University, Advanced Research Institute for Science and Engineering, 17 Kikui-cho, Shinjuku-ku, Tokyo 162-0044, Japan*
[55]*Weizmann Institute, Rehovot 76100, Israel*
[56]*Yonsei University, IPAP, Seoul 120-749, Korea*
(Received 6 November 2006; published 27 February 2007)

Inclusive transverse momentum spectra of η mesons in the range $p_T \approx 2$–12 GeV/c have been measured at midrapidity ($|\eta| < 0.35$) by the PHENIX experiment at RHIC in $p+p$, $d+$Au, and Au+Au collisions at $\sqrt{s_{NN}} = 200$ GeV. The η mesons are reconstructed through their $\eta \to \gamma\,\gamma$ channel for the three colliding systems as well as through the $\eta \to \pi^0\pi^+\pi^-$ decay mode in $p+p$ and $d+$Au collisions. The nuclear modification factor in $d+$Au collisions, $R_{d\mathrm{Au}}(p_T) \approx 1.0$–1.1, suggests at most only modest p_T broadening ("Cronin enhancement").

In central Au+Au reactions, the η yields are significantly suppressed, with $R_{\mathrm{AuAu}}(p_T) \approx 0.2$. The ratio of η to π^0 yields is approximately constant as a function of p_T for the three colliding systems in agreement with the high-p_T world average of $R_{\eta/\pi^0} \approx 0.5$ in hadron-hadron, hadron-nucleus, and nucleus-nucleus collisions for a wide range of center-of-mass energies ($\sqrt{s_{NN}} \approx$ 3–1800 GeV) as well as, for high scaled momentum x_p, in e^+e^- annihilations at $\sqrt{s} = 91.2$ GeV. These results are consistent with a scenario where high-p_T η production in nuclear collisions at the Relativistic Heavy Ion Collider is largely unaffected by initial-state effects but where light-quark mesons (π^0, η) are equally suppressed due to final-state interactions of the parent partons in the dense medium produced in Au+Au reactions.

DOI: 10.1103/PhysRevC.75.024909 PACS number(s): 25.75.−q, 12.38.Mh, 13.85.−t, 13.87.Fh

I. INTRODUCTION

Single-hadron production at large transverse momenta ($p_T \gtrsim 2$ GeV/c) in high-energy hadronic and nuclear collisions results from the fragmentation of quarks and gluons issuing from parton-parton scatterings with large momentum transfer Q^2. Because the cross sections for such hard processes can be calculated perturbatively within quantum chromodynamics (QCD) [1], inclusive high-p_T hadrons (as well as jets, real and virtual direct photons, and heavy quarks) have long been considered sensitive, well-calibrated probes of the small-distance QCD processes. The study of inclusive hadron production at large p_T in proton-proton interactions provides valuable information about perturbative QCD (pQCD), parton distribution functions (PDF) in the proton, and fragmentation functions (FF) of the partons [2]. Furthermore, the use of polarized beams ($\vec{p} + \vec{p}$) allows one to investigate the spin structure of the proton [3]. High-energy collisions of protons or deuterons on nuclear targets (p, d+A) also provide interesting insights on initial- and final-state QCD effects such as modifications of the nuclear PDFs [4,5] and parton rescattering in the cold nuclear medium [6]. Both effects are sensitive to physics such as parton structure and evolution at small values of fractional momentum x in the hadronic wave functions [7] and the dynamics of hadronization in cold nuclei [8,9]. Last, high-p_T hadron production in nucleus-nucleus (A+A) reactions is a sensitive probe of the properties of the strongly interacting QCD matter produced in the collision. Indeed, because perturbative processes happen at time scales $\tau \approx 1/p_T \lesssim 0.1$ fm/c, the hard-scattered partons traverse and are potentially modified by the bulk matter formed shortly after the collision. In this context, the suppression of leading hadrons has been postulated [10] as a signal of "jet quenching" in a quark-gluon-plasma (QGP) due to medium-induced energy-loss of the parent parton [11–13].

All the aforementioned research topics have been addressed in detail by the rich physics program carried out at the Relativistic Heavy Ion Collider (RHIC) at Brookhaven National Laboratory (BNL) during its first 6 years of operation (2000–2006). For example, the study of inclusive high-p_T neutral pion production at midrapidity in $p+p$ [14], $\vec{p} + \vec{p}$ [15], d+Au [16,17], and Au+Au [18–21] collisions at $\sqrt{s_{NN}} =$ 200 GeV has provided valuable information respectively on (i) the gluon-to-pion FF [14,22], (ii) the gluon contribution to the proton spin [23–25], (iii) initial-state effects in cold nuclear matter such as shadowing of the nuclear PDFs [26–29], Cronin broadening [30–32], and gluon saturation [33–35], and (iv) the thermodynamical and microscopic properties of hot and dense QCD matter [36], such as the initial gluon rapidity density dN^g/dy [37] and the transport coefficient $\langle \hat{q} \rangle$ [38,39] of the produced medium; and the mechanism of hadronization in a dense parton medium [40].

In this article, we extend previous PHENIX analyses of high-p_T hadron production in $p+p$ [14,15], d+Au [16], and Au+Au [19–21,41] collisions at $\sqrt{s_{NN}} = 200$ GeV to include an additional identified particle, the η meson, measured in the range $p_T =$ 2–12 GeV/c. The spectra presented here are the hardest (i.e., have the highest p_T) ever measured for the η meson[1] in $p+p$, p+A, and A+A collisions. The high p_T reach of the η helps to characterize the mechanisms of truly perturbative parton-parton scatterings and parton fragmentation in different QCD environments ($p+p$, d+A, and Au+Au). The η data from $p+p$ collisions are presented here as a baseline for medium effects in d+Au and Au+Au. Once a parametrization of the η FF in e^+e^- is performed (see Sec. IV E2), the observed $p+p$ cross section will additionally allow a test of pQCD predictions. Such a FF parametrization would be useful in particular in the light of upcoming high-p_T η asymmetry data obtained with polarized beams of relevance for the proton spin program [44].

For d+Au and Au+Au reactions, we present the single η spectra, the η nuclear modification factors, and the η-to-π^0 ratio measured as a function of p_T in different centralities. Within uncertainties, the d+Au spectra for all centralities are consistent with the $p+p$ yields scaled by the corresponding number of incoherent nucleon-nucleon (NN) collisions. The maximum amount of p_T broadening seen in the η data is 10%, $R_{dAu}(p_T) \approx$ 1.0–1.1. Such a result confirms the limited influence of cold nuclear matter effects, such as shadowing, Cronin broadening or recombination, on high-p_T meson production at midrapidity at RHIC [16,17]. However, the factor of ∼5 deficit of inclusive η yields observed above $p_T \approx$ 4 GeV/c in central Au+Au compared to binary-scaled $p+p$ collisions, $R_{\mathrm{AuAu}}(p_T) \approx 0.2$, is the same as that found for

*Deceased.
†Electronic address: zajc@nevis.columbia.edu.

[1]Before this measurement, only the ISR AFS Collaboration $p+p \to \eta$+X measurement for $p_T =$ 3–11 GeV/c at $\sqrt{s} =$ 62.4 GeV [42] and the single CDF η/π^0 point measured at $p_T =$ 12 GeV/c in $\bar{p}+p$ collisions at $\sqrt{s} = 1800$ GeV [43] had comparable maximum p_T values.

high-p_T π^0 [19,21] and for inclusive charged hadrons [41,45]. Such a common suppression pattern for π^0, η and $h^{\pm}$ is expected if the energy loss takes place at the parton level in the dense medium formed in the reaction *prior* to its fragmentation into a given hadron in the vacuum. Indeed, in this case the high-p_T deficit will just depend on the energy lost by the parent light-quark or gluon (i.e., on the initial density of scatterers in the produced medium) and not on the nature of the final leading hadron whose production will be described by the same *universal* probabilities (fragmentation functions) that govern vacuum hadron production in more elementary systems. Such an interpretation is supported by the fact that the ratio of p_T-differential cross sections of η mesons with respect to π^0 in Au+Au, d+Au, and p+p collisions is approximately constant, $R_{\eta/\pi^0} \approx 0.40$–$0.48$, which is consistent with the world average measured: (i) in hadron-hadron, hadron-nucleus, and nucleus-nucleus collisions above $p_T \approx 3$ GeV/c; as well as (ii) in electron-positron annihilations at the Z pole ($\sqrt{s} = 91.2$ GeV) for *energetic* η and π^0 with scaled momenta $x_p = p_{\text{hadron}}/p_{\text{beam}} \gtrsim 0.35$. Comparison of our data to a world compilation of η/π^0 ratios is done in the last section of the article.

In addition to their interest as a *signal* in their own right, reliable knowledge of the production of η mesons in p+p, d+Au, and Au+Au reactions is also required to determine and statistically remove the *background* of secondary $e^{\pm}$ and γ for other measurements such as single electrons (from heavy-quark decays) [46,47], dielectrons [47], and direct photons [48,49]. Indeed, η mesons constitute the second most important source after the π^0 of decay electrons (Dalitz and conversion) and photons contributing to these backgrounds.

The article is organized as follows. Section II presents a description of the experimental setup and detector systems used in this work. Section III provides an explanation of the analysis methods employed to obtain the η data. Section IV presents and compares the η results (p_T spectra, nuclear modification factors, and η/π^0 ratios) measured in p+p, d+Au, and Au+Au at $\sqrt{s_{NN}} = 200$ GeV and discusses the relative role of cold nuclear (d+Au) and hot and dense medium (Au+Au) effects on high-p_T meson production. In particular, Sec. IV E discusses the measured η-to-π^0 ratios in the context of different phenomenological models of high-p_T hadron production as well as in comparison to other experimental results measured in high-energy particle collisions at different center-of-mass energies. A less detailed presentation of a subset of these η results has already been published in [20].

II. EXPERIMENTAL SETUP

The PHENIX experiment at the RHIC facility [50] at BNL is specifically designed to measure hard QCD probes such as high-p_T hadrons, direct photons, leptons, and heavy flavor production. PHENIX achieves good mass and particle identification (PID) resolutions as well as small granularity by combining 13 detector subsystems (~350,000 channels) divided into (i) two central arm spectrometers for electron, photon, and hadron measurements at midrapidity ($|\eta| < 0.35$, $\Delta\phi = \pi$); (ii) two forward-backward ($|\eta| = 1.2$–2.2, $\Delta\phi = 2\pi$) spectrometers for muon detection; and (iii) two global (inner) detectors for trigger and centrality selection. A detailed description of the complete detector can be found elsewhere [51]. The data presented in this article were obtained during the Run-2 (2001–2002, Au+Au) and Run-3 (2003, d+Au, p+p) operations at RHIC. The layout of the PHENIX detector during these run periods is shown in Fig. 1. The primary detectors used to obtain the present results are the PHENIX central arm spectrometers, particularly the electromagnetic calorimeters (EMCal) [52] and the charged-particle tracking devices [the drift chamber (DC) [53] and pad chambers (PC) [54]]. In addition, the beam-beam counters (BBC) [55] and the zero-degree calorimeters (ZDC) [56] are used for triggering, event characterization and (Au+Au and d+Au) centrality determination.

A. Electromagnetic calorimeter (EMCal)

The η mesons are detected in PHENIX via their $\gamma\gamma$ (branching ratio BR = 39.43%) and $\pi^0\pi^+\pi^-$ (BR = 22.6%) decays [57]. Photons from the direct $\gamma\gamma$ channel as well as from the secondary (daughter) π^0 decays are measured in the PHENIX EMCal, which has a pseudorapidity acceptance of $-0.35 < \eta < 0.35$ and covers π radians in azimuth. The electromagnetic calorimeter is divided into eight sectors with two distinct detection technologies (see Fig. 1). A lead-scintillator calorimeter (PbSc) consists of 15,552 individual lead-scintillator sandwich modules ($5.54 \times 5.54 \times 37.5$ cm, $18X_0$), grouped in six sectors located at a radial distance of 5.1 m from the beam line, covering a total solid angle of $\Delta\eta \approx 0.7$ and $\Delta\phi \approx 3\pi/4$. A lead-glass Čerenkov calorimeter (PbGl) comprising two sectors, with a total of 9,216 modules ($4 \times 4 \times 40$ cm, $14.4X_0$), is located at a radial distance of ~5 m from the beam pipe and covers a total solid angle at midrapidity of $\Delta\eta \approx 0.7$ and $\Delta\phi = \pi/4$. The corresponding $\Delta\eta \times \Delta\phi$ acceptance of a single tower at $\eta = 0$ is 0.011×0.011 and 0.0075×0.0075 for the PbSc and PbGl calorimeters, respectively. The chosen transverse size of the towers is not much larger than their corresponding Molière radius ($\rho_M = 3.0$ cm and 3.7 cm for PbSc and PbGl, respectively) so that most of the electromagnetic showers extend over several modules, resulting in an improved position resolution based on a "center of gravity" reconstruction of the impact point of the photon clusters.

The energy calibration of the PbSc modules was obtained from the original beam-test values and redundantly confirmed with (i) the position of the reconstructed π^0 mass peak, (ii) the energy deposit from minimum-ionizing charged particles traversing the calorimeter, as well as with (iii) the expected $E_{\text{PbSc}}/p_{\text{tracking}} \sim 1$ value measured for electrons and positrons identified in the Ring-Imaging Čerenkov (RICH) detector and whose momentum was measured in the tracking detectors. In the PbGl modules, the reference energy calibration from the original beam-test values is corrected with the time-dependent gain corrections obtained with a light-emission-diode (LED) system for the lead-glass calorimeter. The LEDs emit light with known intensity, so gain fluctuations can be detected. The final

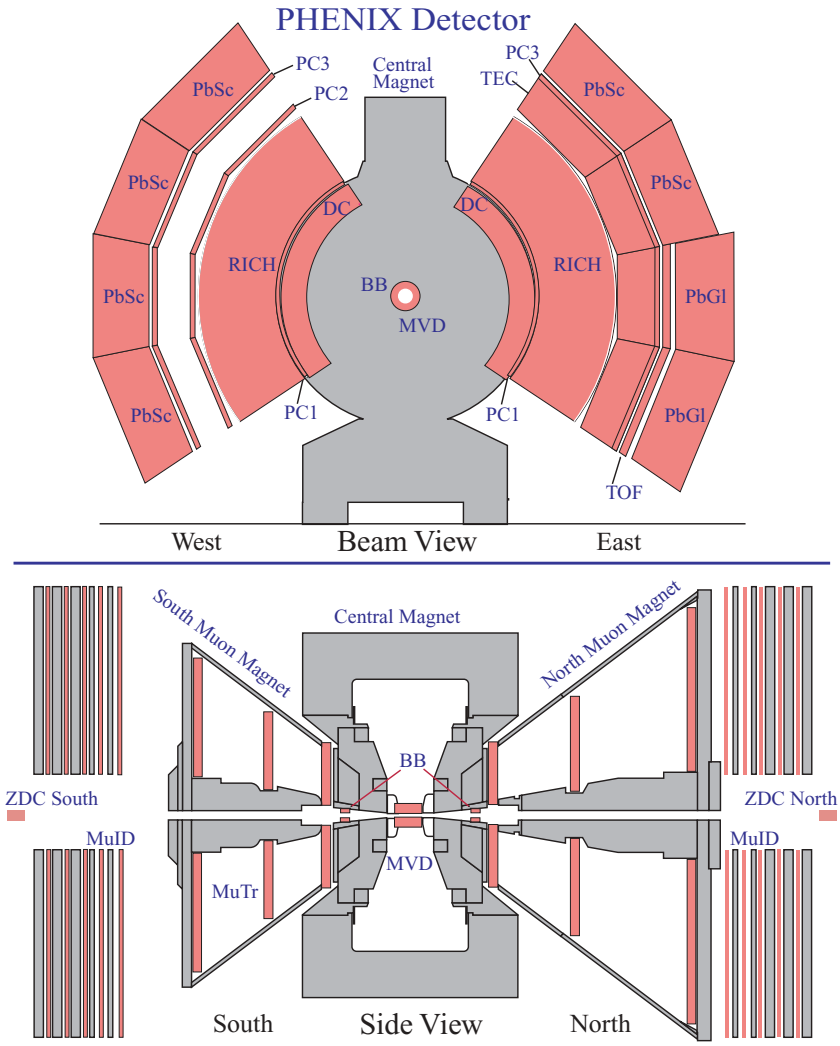

FIG. 1. (Color online) The PHENIX experimental setup during Run-2 and Run-3 at RHIC. The detectors used in the present analysis are the 8 EMCal (PbSc, PbGl) sectors for photon detection ($\eta \to \gamma\,\gamma$), the drift chamber (DC), and two layers of multiwire proportional chambers with pad readout (PC) for charged pion detection ($\eta \to \pi^0\pi^+\pi^-$); as well as the two beam-beam counters (BBC) and the two zero-degree calorimeters (ZDC) for global event characterization.

PbGl calibration is obtained by comparing the measured π^0 peak position to its nominal value.

B. Central arm tracking

Charged pions are measured with the PHENIX central tracking system combining information from the drift and pad chambers. The momenta of the $\pi^{\pm}$ are measured at a radius of 2.0 m from the event vertex by the DC. The DC, located outside the field of PHENIX central magnets, uses several layers of wires to reconstruct the angle of the track, which is inversely proportional to its momentum. The DC momentum resolution is determined to be $0.7 \oplus 1.1\% p_T$ (GeV/c). The polar angle of the track is measured by pad chamber 1 (PC1), a multiwire proportional chamber located just beyond the DC. The last pad-chamber layer, PC3, at a radius of 5.0 m and directly in front of the EMCal, is used in this analysis for two purposes: to confirm the track by matching to a PC3 hit, as well as to veto an EMCal cluster produced by a charged particle track.

The DC momentum scale is checked by the reconstruction of the correct mass of (i) $\pi^{\pm}$, $K^{\pm}$, p, $\bar{p}$ identified with the time-of-flight (TOF) system [58] and (ii) ω, ϕ, J/Ψ mesons decaying into the e^+e^- channel identified with the RICH and EMCal. The momentum scale is thus known with an accuracy better than 0.2%. Because at low p_T, the momentum resolution is better when measured with the tracking system than that using the energy measured via calorimetry, and given that the momentum range of the three η decay products has a relatively low p_T, the uncertainties in the tracking system calibration are less important in the $\pi^0\pi^+\pi^-$ measurement than in the $\gamma\gamma$ decay channel. As a result, the tracking devices provide better accuracy for the η mass reconstruction than the EMCal.

C. Global detectors

Triggering and global event characterization is achieved using the BBC and the ZDC. The two BBC are placed around the beam pipe 1.44 m in each direction from the nominal interaction point. Each BBC consists of 64 hexagonal quartz Čerenkov radiators closely packed in an approximately azimuthally symmetric configuration. The BBC are used to count the charged particle multiplicity in the pseudo-rapidity range $3.0 < |\eta| < 3.9$, to provide the start time for TOF

TABLE I. Events sampled and integrated luminosity (after vertex cuts) in the η analyses for $p+p$, d+Au, and Au+Au collisions. The equivalent $p+p$ luminosities in d+Au (Au+Au) have been obtained normalizing their corresponding luminosities by 2 A (A^2) factors as expected for hard cross-section scaling.

Collision system	Events sampled		Total integrated luminosities		BBC attributes	
	MB (LVL1) trigger	High-p_T (γ) trigger	Absolute	Equivalent $p+p$	Cross section	Efficiency
$p+p$	25.2×10^6	49.3×10^8	216 nb^{-1}	216 nb^{-1}	23.0 mb $\pm$ 9.7%	(55 $\pm$ 5)%
d+Au	58.3×10^6	29.2×10^8	1.5 nb^{-1}	590 nb^{-1}	1.99 b $\pm$ 5.2%	(88 $\pm$ 4)%
Au+Au	34×10^6	30×10^6	9 μb^{-1}	230 nb^{-1}	6.315 b $\pm$ 8.4%	(92 $\pm$ 3)%

measurement, and to give the collision vertex position along the interaction diamond with a typical resolution of 0.6 (2) cm in Au+Au ($p+p$) collisions [55]. In d+Au collisions, the centrality of the collision is determined by measuring the charge deposited in the BBC in the *Au* beam direction [59]; whereas in Au+Au reactions, the correlation between the BBC charge sum and the ZDC total energy is used for centrality determination [60] (see the next section). The ZDC are small hadronic calorimeters that measure the energy carried by spectator neutrons at very forward angles. They are placed 18 m up- and downstream of the interaction point along the beam line ($|\theta| < 2$ mrad). Each ZDC consists of three modules with a depth of 2 hadronic interaction lengths read out by a single photomultiplier tube (PMT). Both time and amplitude are digitized for each PMT along with the analog sum of the three PMT signals for each ZDC.

III. DATA ANALYSIS

In this section, we describe the event selection criteria, the reaction centrality determination in d+Au and Au+Au collisions, the η identification and reconstruction procedures in the $\eta \to \gamma\,\gamma$ and $\eta \to \pi^0\pi^+\pi^-$ channels and the various corrections (geometrical acceptance, reconstruction efficiency, trigger, absolute cross-section normalization) applied to the raw data. The systematic uncertainties of the measurements are discussed at the end of the section.

A. Event selection

The data presented in this article were collected under two general trigger conditions. The first sample, consisting of minimum-bias (MB) events with vertex position along the beam axis $|z| < 30$ cm, was conditioned on a local-level-1 (LVL1) trigger generated by coincidences between the two BBC (in the case of $p+p$ and d+Au) or by coincidences between the BBC and ZDC detectors (in the case of Au+Au). The MB trigger cross sections measured by the BBC in $p+p$ and d+Au collisions are, respectively, 23.0 mb $\pm$ 9.7% mb and 1.99 b $\pm$ 5.2% [61], whereas the Run-2 Au+Au minimum bias trigger has some inefficiency for the most peripheral interactions and records only $92.2^{+2.5}_{-3.0}$% of $\sigma_{\mathrm{Au\ Au}}$ [19]. In other words, the LVL1 triggers accept, respectively, (55$\pm$5)%, (88$\pm$4)%, and (92$\pm$3)% of the total inelastic cross sections: $\sigma_{pp}^{\mathrm{inel}} = 42 \pm 3$ mb, $\sigma_{dAu}^{\mathrm{inel}} = 2260 \pm 100$ mb, and $\sigma_{\mathrm{Au\ Au}}^{\mathrm{inel}} = 6850 \pm 540$ mb. A second "photon-triggered" sample, requiring electromagnetic showers above a given threshold in the EMCal (with or without the MB BBC requirement), has been used to extend the η measurements to higher p_T. The details of this level-2 (LVL2) software trigger are described in Ref. [21]. The total number of events collected in the MB and photon-triggered samples (after vertex cuts) as well as the integrated luminosities for each collision system are listed in Table I.

B. Centrality determination (d+Au, Au+Au)

The events in d+Au collisions are classified into four different centrality classes given in percentiles of the total cross section: 0–20%, 20–40%, 40–60% and 60–88%, with the latter being the most peripheral. The reaction centrality is related to the number of hits in the south beam-beam counter (BBCS), which is proportional to the number of participant nucleons in the gold nucleus [59]. The distribution of the normalized charge in the BBCS and the classification into different centrality classes is shown in Fig. 2. To obtain reasonably large

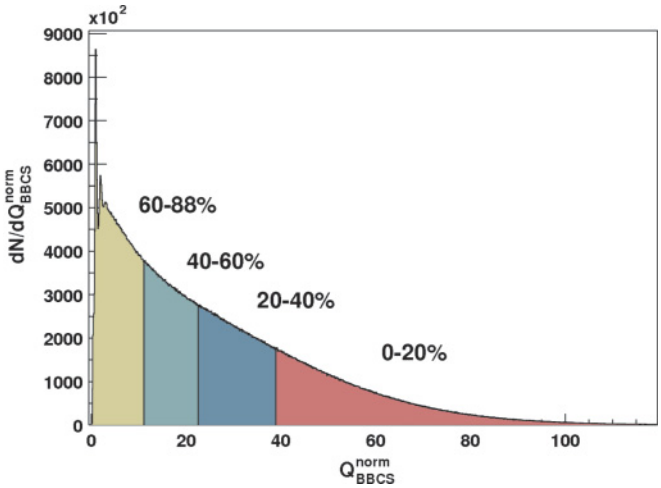

FIG. 2. (Color online) Distribution of the normalized charge in the south beam-beam counter (BBCS) in d+Au collisions at $\sqrt{s_{NN}} =$ 200 GeV. The normalization is done such that the normalized charge corresponds to the number of hits.

TABLE II. Values of the average nuclear overlap function $\langle T_{dA}\rangle$ and $\langle T_{AA}\rangle$ for the different centralities considered in d+Au and Au+Au reactions, respectively.

Centrality bin	$\langle T_{dA}\rangle$ (mb^{-1})	$\langle T_{AA}\rangle$ (mb^{-1})
Min bias	0.20 ± 0.01	6.14 ± 0.45
0–20%	0.36 ± 0.02	18.5 ± 1.3
20–40%	0.25 ± 0.017	—
20–60%	—	4.6 ± 0.4
40–60%	0.17 ± 0.014	—
60–88%	0.073 ± 0.007	—
60–92%	—	0.3 ± 0.1

statistics in each Au+Au centrality class, three centralities are used in the current Au+Au analysis: 0–20% (central), 20–60% (semicentral), and 60–92% (peripheral), determined by cuts in the correlated distribution of the charge detected in the BBC and the energy measured in the ZDC [60]. A Glauber Monte Carlo model combined with a simulation of the BBC (plus ZDC) response allows determination of the mean value of the associated nuclear overlap function $\langle T_{dA}\rangle$ ($\langle T_{AA}\rangle$) for each d+Au (Au+Au) centrality bin. Table II lists the mean value of the nuclear overlap function for different centralities in both systems.

C. $\eta \to \gamma\,\gamma$ Reconstruction

The main mode of η-meson reconstruction in PHENIX is via the electromagnetic channel $\eta \to \gamma\,\gamma$. PHENIX has published the results of a number of $\pi^0 \to \gamma\,\gamma$ measurements in the EMCal for different colliding systems [14–21]. The technique for identifying the photons and reconstructing the π^0 yields as a function of p_T and centrality is now well established and is exactly the same one used here to obtain the corresponding η yields. Although the reconstruction methods are identical, the p+p and d+Au analyses do not suffer from the large particle multiplicity background that the Au+Au η reconstruction faces, and there are a few differences between Au+Au and the other studies. In the Au+Au case, the applied analysis cuts (photon identification, invariant mass reconstruction, and other cuts) are tighter than in the p+p and d+Au cases. Additionally, to deal with cluster overlap effects appropriately, the Au+Au analysis uses a full GEANT [62] Monte Carlo (MC) simulation, in which the simulated single η are embedded into real events rather than a tuned fast MC simulation without embedding. These differences are explained in separate subsections below.

1. Photon reconstruction in EMCal

Electromagnetic clusters are reconstructed in the EMCal sectors by finding contiguous calorimeter towers with pulse heights above the ADC pedestal value. The energy of each EMCal cluster is corrected for angular dependence and nonlinearity based on test-beam results and simulation. The linearity correction for the two detector types is different, with the PbGl having a stronger dependence on the energy. The correction factors for a photon with a detected energy of 1 GeV (10 GeV) are 1.00 (0.95) for the PbSc and 1.05 (0.975) for the PbGl, respectively. The PbGl calorimeter also shows a stronger variation of the measured photon energy with the angle of incidence on the detector surface: at 20° the measured energy is reduced by 5% compared to perpendicular incidence (0°), whereas in the PbSc this reduction is only of the order of 2%.

Because we are interested in high-p_T η production, only EMCal clusters with energy above 1 GeV are selected for further analysis. In addition, fiducial cuts excluding the edges of each EMCal sector, as well as an area of 3×3 towers around the towers that have been determined to be hot or dead, were applied to exclude clusters with incorrectly reconstructed energies. Among the clusters passing the cuts, photon candidates are identified by applying standard particle identification (PID) cuts based on TOF and shower profile. Both cuts are applied to reject slower and broader showers that are mostly of hadronic origin. For the PbSc we require the measured cluster TOF to be $t_{\rm clust} < L/c \pm 1.2$ ns where L is the straight-line path from the collision vertex to the reconstructed cluster centroid. For the PbGl we require reconstructed clusters to have times, $t_{\rm clust} < L/c \pm 2$ ns; the difference is due to the difference in intrinsic timing resolution of the two calorimeter technologies. Shower profile cuts are based on rejecting those clusters whose energy deposition among the modules, and in particular in the most central tower of the cluster, is not consistent, within a given χ^2-test limit, with the shower shape expected for electromagnetic showers as parametrized from test-beam data [52].

In the most central Au+Au events, the EMCal typically detects $\gtrsim$300 clusters, corresponding to a detector occupancy of $\sim$10% in terms of hit towers, resulting in a non-negligible probability of particles making clusters which overlap. To minimize the effects of cluster overlaps due to high multiplicity, two methods are used to determine the cluster energy. First the energy of each cluster in the PbSc calorimeter is determined from the sum of all contiguous towers with deposited energy above a given threshold ($E_{\rm tower} = 15$ MeV, typically). Alternatively, an extrapolation (using a standard electromagnetic shower profile for an event with zero background) from the measured core energy (*ecore*) in the four central towers to the full cluster energy is used. For the latter case, the *ecore* energy was computed from the experimentally measured center of gravity, central shower energy, and impact angle in the calorimeter using a parametrized shower profile function obtained from electromagnetic showers measured in the beam tests. Such an *ecore* energy represents an estimate of the true energy of a photon impinging on the PbSc unbiased by background contributions from other particles produced in the same event and depositing energy in the neighborhood of a given cluster. The use of *ecore* instead of the total cluster energy for photon reconstruction helped considerably to minimize the effects of cluster overlaps in central Au+Au collisions.

2. Raw η yield extraction (p+p and d+Au)

The η yields are obtained by an invariant mass analysis of photon candidate pairs having asymmetries $\alpha = |E_{\gamma_1} -$

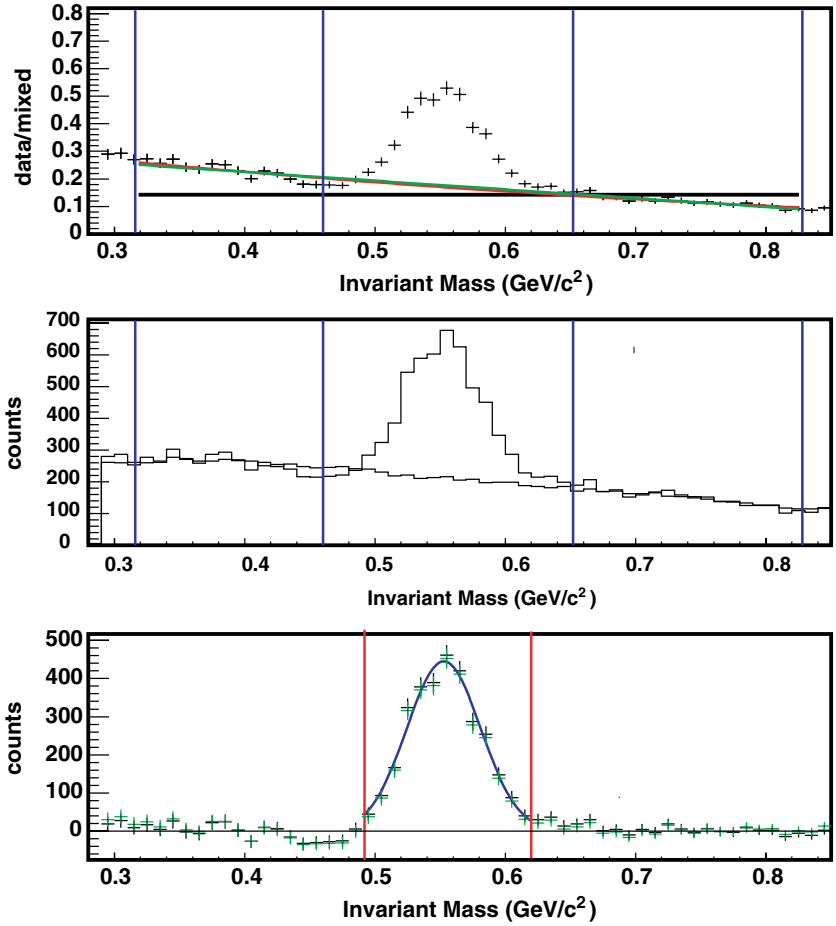

FIG. 3. (Color online) Invariant mass distribution of photon candidate pairs measured in $p+p$ collisions for the default PID cuts with pair transverse momenta 4.0 GeV/c < p_T < 4.5 GeV/c. (Top) Ratio of real and mixed event distributions, and background fits. The red fit is used for the background parametrization and the green fit for estimating the systematic uncertainty. (Middle) Real invariant mass spectrum and scaled background. (Bottom) Final distribution with the scaled background subtracted from the real event distribution (black entries); the green entries result from the background fit for estimating the systematic error. Additionally, the peak is fitted with a Gaussian to get its mean and σ.

$E_{\gamma_2}|/(E_{\gamma_1} + E_{\gamma_2}) < 0.7$. The cut on the asymmetry α reduces the background because high-p_T combinatorial pairs are strongly peaked near $\alpha = 1$ due to the steeply falling spectrum of single-photon candidates. The resulting invariant mass spectra obtained for proton-proton and deuteron-gold collisions are shown in Figs. 3 and 4, respectively, for two typical p_T bins. A peak is seen at about 550 MeV/c^2, the expected mass of the η meson. The measured peak position is modified by detector effects that lead to energy smearing. The combined effects of the energy resolution of the detector, the steeply falling single-photon spectrum, and the finite size of the energy bins lead to a smearing of the measured photon energies that widens the η signal. As a result the average peak position in the invariant mass spectra is about 9 MeV/c^2 larger than the nominal mass of the η meson, an effect that is well reproduced by the simulation.

The combinatorial background below the peak signal is estimated with the event mixing method in which clusters from different events with similar event vertex (and centrality class in d+Au) are combined to produce a "background" invariant mass distribution. This background is normalized to the real invariant mass spectrum and then subtracted from the invariant mass spectrum of the real events. To estimate the normalization of the background, the distribution of the real events is first divided by the mixed event distribution. This ratio is shown in the upper panel of Figs. 3 and 4. The normalization function is estimated by a fit in the region outside the peak. The spectrum, fitted to a second-degree polynomial, is shown in the region denoted by the vertical lines in the upper and the middle panels of Figs. 3 and 4. The final real event mass distribution after the background subtraction is shown in the lower panel of Figs. 3 and 4.

The interval over which the background is adjusted is limited by two considerations: the expected η peak position m and width σ. Both were estimated in a first analysis of the spectra and set to $m = 556$ MeV/c^2 and $\sigma = 32$ MeV/c^2. The background interval includes the region between $m - 7.5\sigma$ and $m + 8.5\sigma$ (320 and 830 MeV/c^2) excluding the peak region $m \pm 3\sigma$ (460 MeV/c^2 < m_{inv} < 650 MeV/c^2). For higher transverse momenta, the background almost vanishes and thus the estimation of the normalization by a fit leads to large errors. Hence an alternative method is used where the fit function is replaced by the ratio of the number of photon pairs in the normalization region in the real and the mixed event distributions.

Finally, the total number of η in a given p_T bin is obtained by integration of the invariant mass distribution within 3σ around the η peak position. The statistical error of the peak extraction is estimated as done for the π^0 and described in Ref. [21]. The uncertainty of the background parametrization is estimated by calculating the error on the ratio of the integrals of the real and the mixed event distributions in the region of the background fit. Above $p_T = 10$ GeV/c in $p+p$ collisions, the mixed event background does not work as expected as there

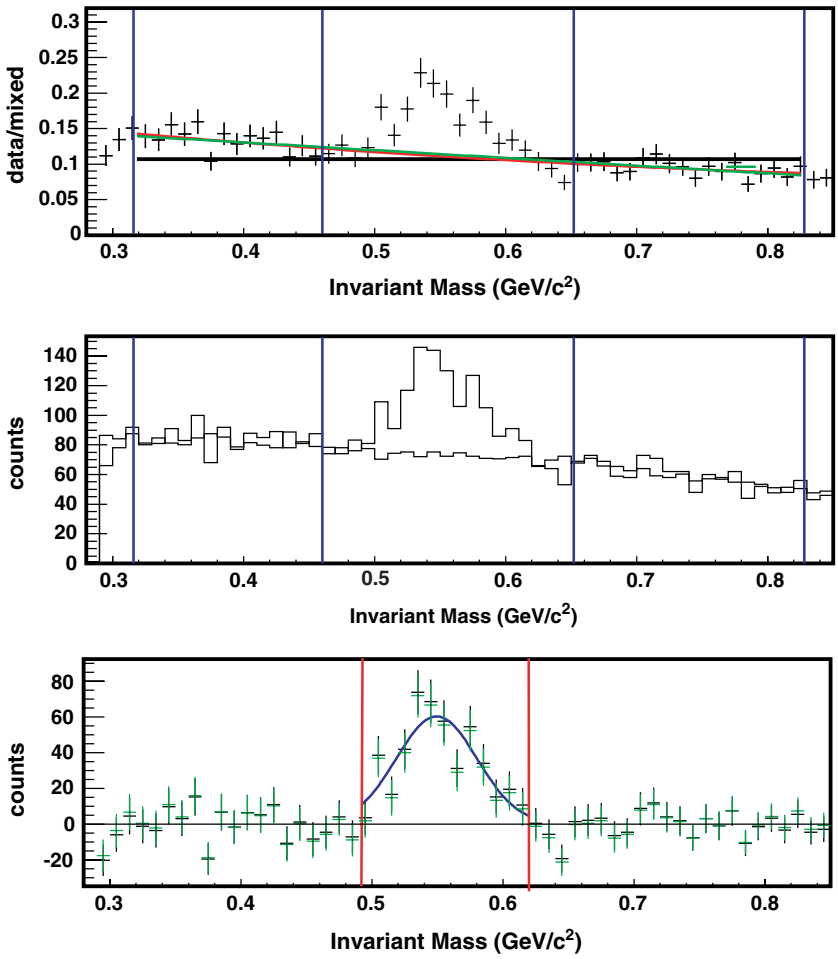

FIG. 4. (Color online) Invariant mass distribution of photon candidate pairs measured in minimum bias d+Au collisions for the default PID cuts with pair transverse momenta 3.5 GeV/c < p_T < 4.0 GeV/c. (Top) Ratio of real and mixed event distribution and background fits (the red fit is used for the background parametrization, the green fit for estimating the systematic uncertainty). (Middle) Real invariant mass spectrum and scaled background. (Bottom) Final distribution with the scaled background subtracted from the real event distribution (black entries). The green entries result from the background fit for estimating the systematic error. Additionally, the peak is fitted with a Gaussian to get its mean and sigma.

are some entries in the mixed event background but not in the η region. For these cases, the background was estimated by integrating the real event distribution outside the peak (in the fit region mentioned above) and scaling this to the η integration region. This background is then subtracted from the real event distribution to get the number of η. The error in this case is estimated with $\sigma^2_{\mathrm{Sig}} = S + 2B$, S being the η signal and B being the background. The integral of the invariant mass distribution after the background subtraction is calculated in a reduced interval $m - 2\sigma; m + 2\sigma$ (492–620 MeV/c^2).

3. *Raw η yield extraction (Au+Au)*

The η yields for Au+Au are determined by calculating the invariant mass of photon pairs with asymmetries $\alpha = |E_{\gamma 1} - E_{\gamma 2}|/(E_{\gamma 1} + E_{\gamma 2}) < 0.5$, a value tighter than that used for the p+p and d+Au cases to reduce the larger uncorrelated background in Au+Au collisions, and binned in p_T. The η yield in each p_T bin is determined by integrating the background-subtracted $\gamma\,\gamma$ invariant mass distribution around the η peak. The combinatorial background is obtained by combining uncorrelated photon pairs from different events with similar centrality and vertex and normalizing the distribution in a region below ($m_{\mathrm{inv}} = 400$–450 MeV/c^2) and above ($m_{\mathrm{inv}} = 750$–1000 MeV/c^2) the η mass peak (Fig. 5 top). After the mixed background subtraction, the resulting distribution is fitted to a Gaussian plus an exponential (or linear, see below) function to account for the residual background—more important at low p_T—not completely removed by the event-mixing technique. The bottom plot in Fig. 5 depicts the η signal after mixed (and residual) background subtraction. To estimate the uncertainty in the subtraction of the residual background, different pair asymmetries and an alternative linear parametrization were used (see Sec. III F). The signal-to-background (S/B) ratio in peripheral (central) Au+Au collisions is approximately 1.3 (1.5) and 0.05 (0.002) for the highest and lowest p_T, respectively. The signal-to-background ratio is comparable for central and peripheral collisions at the highest p_T because the spectrum in the central data extends to higher p_T than that in the peripheral.

The scaled mixed-event distribution is subtracted from the real-event distribution to produce a statistical measure of the true η yield. The result of such a subtraction procedure is shown in the bottom plot of Fig. 5. The raw η yield is obtained by integrating the subtracted invariant mass distribution in a range determined by the mean and the width of the η peak and given by $m_{\mathrm{inv}} \in [m_\eta - 2\sigma_\eta, m_\eta + 2\sigma_\eta]$. The analysis described above is applied in bins of $\Delta p_T = 1$ GeV/c for $p_T =$ 2–4 GeV/c and $\Delta p_T = 2$ GeV/c above. We cease attempting to extract η yields at high p_T when the number of pairs within the

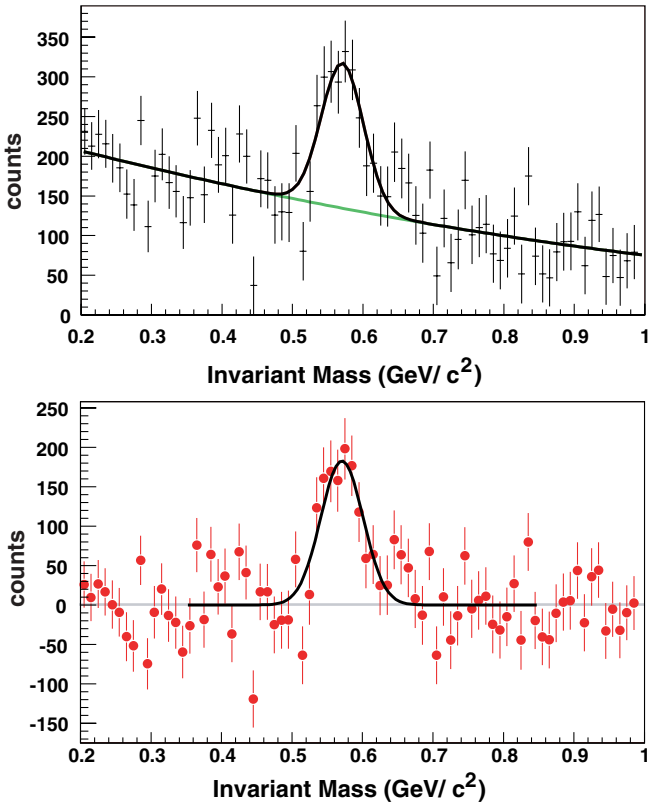

FIG. 5. (Color online) (Top) Invariant mass distribution of pairs of photon candidates measured in minimum bias Au+Au with pair momenta $p_T = 3.5$–4.5 GeV/c around the η mass fitted to a Gaussian plus exponential. (Bottom) Final η signal after mixed-event (and residual) background subtraction.

selected (background-subtracted) η mass window falls below 4 counts.

4. Acceptance correction

The geometric acceptance is evaluated using a fast Monte Carlo (fastMC) program based on routines from the JETSET library [64] to simulate the $\eta \to \gamma\gamma$ decays and determine the geometric acceptance of the calorimeter for the decaying photons. The acceptance correction accounts for the fraction of produced η mesons whose decay photons will not actually hit the detector due to the finite solid angle covered by the detector. A decay photon will be accepted by the EMCal in the fastMC when it hits the active surface of the detector covering the pseudorapidity range $-0.35 < \eta < 0.35$ (computed using a realistic distribution of event vertices within $|z| < 30$ cm) and $2 \times 90^\circ$ in azimuth. The acceptance shows a strong dependence on the transverse momentum because the opening angle of the decay photons decreases with increasing p_T. Thus, the probability that both decay photons hit the detector decreases for small values of p_T. The acceptance for $p+p$ and $d+$Au collisions is shown in Fig. 6. The acceptance is influenced by the geometry of the whole detector as well as by dead and hot modules in the $p+p$ and $d+$Au cases (for Au+Au the efficiency losses due to dead and hot modules are computed from the full GEANT3 simulation plus "embedding" and

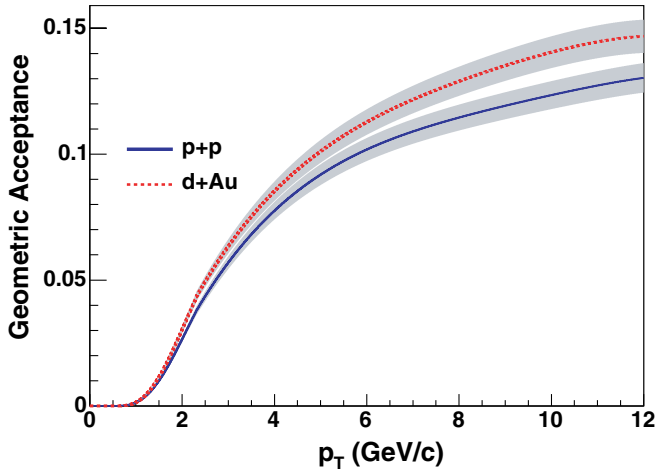

FIG. 6. (Color online) Geometric acceptance (including dead channels) for the η meson as a function of p_T measured in the EMCal in both $d+$Au (dashed curve) and $p+p$ (solid curve) collisions at PHENIX in Run-3.

are accounted for in the *efficiency* loss correction). Due to a different number of masked out modules, the acceptance is not exactly the same in $p+p$ and $d+$Au collisions.

5. Efficiency corrections of the raw η yields ($p+p$, $d+$Au)

a. Reconstruction efficiency correction. The reconstruction efficiency takes into account that the measured η spectrum in the detector is different from the real physical spectrum, i.e., the reconstruction efficiency is defined as the ratio between the output and the input η spectra:

$$\varepsilon(p_T) = \frac{dN_\eta/dp_T|_{\text{output}}}{dN_\eta/dp_T|_{\text{input}}} \tag{1}$$

as obtained using the fastMC, which parametrizes all the detector effects on the input spectrum (EMCal energy and position resolution, efficiency losses due to γ identification cuts and $\gamma\gamma$ reconstruction procedure, etc.). A realistic input η spectrum $dN/dp_T|_{\text{input}}$ is used as an initial spectrum for the efficiency calculation and an iterative procedure is performed, in which the corrected output spectrum is used as the input spectrum of the next iteration. To simulate detector effects, the smeared energies and hit positions of the decay photons are parametrized in the fastMC. The energy smearing has a constant and an energy-dependent term and follows the functional form

$$\sigma_E/E = \frac{A}{\sqrt{E/\text{GeV}}} \oplus B\,. \tag{2}$$

The parameters for Eq. (2) are given in Table III for the different collision systems and the two EMCal detector types. The initial values have been taken from the detector response obtained in the beam tests [52] and retuned for real run conditions in previous π^0 analyses [14,15]. During the cross-checks between simulated and real data it was found that the energy scale of the EMCal was slightly shifted compared to the parametrized results. Because the energy

TABLE III. Parameters for energy smearing, Eq. (2), as used in the fastMC for the different EMCal detector types and the different collision systems.

Collision system	Detector type	Energy-dependent term (A)	Constant term (B)
$p+p$	PbGl	0.085	0.059
$p+p$	PbSc	0.082	0.050
d+Au	PbGl	0.085	0.059
d+Au	PbSc	0.082	0.050

scale is estimated experimentally by fitting the location of the π^0 peak, and the position of the peak is also affected by reconstructed secondary neutral pions from K^0_s decays that themselves decay off vertex, an additional correction is applied in the fastMC shifting the energy scale by 0.7%. After this correction, the position and the width of the simulated η peaks are confirmed to be consistent with the position and the width measured in the data for all p_T bins.

The efficiency correction also takes into account the different cuts used for particle identification. The simulation must consider the loss of photons and thus of η due to the applied shower shape (or "dispersion") and energy threshold cuts. The effect of the dispersion cut is estimated by a comparison of uncorrected spectra without a PID cut with the spectra obtained with the different PID cuts. The spectra are obtained with a sharp asymmetry (α) cut and as a function of $(E_1 + E_2)/2$. The resulting loss of η is translated into a photon loss probability, which is then used in the simulation. The energy cut is reproduced by rejecting photon hits according to an energy-dependent survival probability in the simulation. Finally, the simulation reconstructs the invariant mass and the transverse momentum of the η from the reconstructed (smeared) information. Only particles inside the interval used for the integration of the real peak are accepted. The overall η efficiency losses obtained by this method are of the order of $\varepsilon_{\eta\to\gamma\gamma} = 76\% \pm 3\%$ (dominated by the asymmetry cut and the invariant mass yield extraction procedure) and are flat within 1–2% in the whole p_T range measured for both ($p+p$ and d+Au) colliding systems.

b. Photon conversion correction. Some of the produced η are not reconstructed due to conversions of one or both decay photons in the inner regions of the PHENIX detector. Such an effect is not included in the fastMC and is computed independently using a full simulation of the detector including a realistic description of the material in front of the EMCal. The correction factors obtained from this analysis are 1.067 ± 0.003 for PbSc West, 1.052 ± 0.004 for PbSc East, and 1.076 ± 0.005 for PbGl, as the material between the collision vertex and the EMCal is different in the east and the west arm and between PbGl and PbSc.

6. *Efficiency corrections of the raw η yields (Au+Au)*

In the Au+Au case, the detection efficiency is determined using a full PISA (PHENIX Integrated Simulation Application) GEANT3-based Monte Carlo (MC) program of the PHENIX detector to simulate the complete response of the calorimeter to single η decays. The nominal energy resolution was adjusted in the simulation by adding an additional p_T-independent energy smearing of ~3% for each PbSc tower. The shape, position, and width of the η peak measured for all p_T and centralities were thus well reproduced by the simulated data. The data from each simulated η is embedded into real Au+Au events and the efficiency for detecting the embedded η is evaluated analyzing the merged events with the same analysis cuts used to obtain the real yields. Using this technique we determine efficiency corrections that account not only for the energy resolution and position resolution of the calorimeter but also for the losses due to overlapping clusters in a real Au+Au event environment. The embedding also permits a precise determination of the effect of edge cuts and bad modules. Though these effects can in principle be considered as geometric acceptance corrections (as done in the $p+p$ and d+Au analyses), they depend not only on the geometry but also on the energy deposition of an electromagnetic shower in the different calorimeter towers. Last, in the full-simulation plus embedding procedure we additionally have control over the effects of photon conversions, as the GEANT simulation considers the material in front of the EMCal and the information whether a decay-photon converts is kept for evaluation in the efficiency determination.

The input η spectrum embedded in real events is weighted to match a functional form fit to the measured η spectrum so that the correct folding of the η spectrum with the resolution is obtained. This procedure is iterated, with the fit of the p_T dependence of the input weights adjusted as the estimate of the efficiency correction improves, until the procedure converges within the nearly p_T-independent statistical error of the embedded sample, approximately 3%. The final overall η yield reconstruction efficiency correction factor was ~3 with a centrality dependence of $\lesssim$20%. The losses were dominated by fiducial and asymmetry cuts.

D. $\eta \to \pi^0\pi^+\pi^-$ Reconstruction

1. *Raw η yield extraction*

The second mode of η-meson reconstruction in PHENIX is via the three-body decay channel $\eta \to \pi^0\pi^+\pi^-$ with branching ratio BR = 22.6% ± 0.4%. This mode has been used for the $p+p$ and d+Au data but not for the Au+Au where the large detector occupancy makes the signal very difficult to extract. Reconstruction starts with identifying the π^0 candidates among the pairs of EMCal γ clusters with energy $E_\gamma > 0.2$ GeV in the same way described in the previous section for the direct $\eta \to \gamma\gamma$ channel. The mass of a candidate is required to be within two standard deviations from the peak position of π^0. The peak position and its width are determined by the π^0 decay kinematics and EMCal resolution for each of the clusters and its position. These parameters were found to be consistent with the expected values. Selected π^0 candidates with transverse momentum $p_T > 1.0$ GeV/c are assigned the exact mass of the meson and measured p_T of the pair. These candidates are further combined into triplets with

positive and negative particle tracks measured by DC and PC1 to have momentum in the range $0.2\ \text{GeV}/c < p_T < 4.0\ \text{GeV}/c$. No particle identification was used on the charged tracks.

To extract the raw η yields the mixed-event subtraction technique was not used in this case because it does not adequately reproduce the shape of the background in the real events. The most important physical reason for this is that there are a significant number of correlated tracks among the $\pi^+\pi^-$ pairs coming from various heavier particle decays. The yield extraction was done by simultaneous fitting of the peak and the background in the adjacent region. The characteristic peak in the three-particle mass distribution is shown in the top panel of Fig. 7. The position of the peak is consistent with the nominal mass of the η meson within the statistical error of the fit shown in the figure. The measured 8 MeV/c^2 width of the peak is narrower than in the $\eta \to \gamma\,\gamma$ decay channel. Unlike the $\gamma\,\gamma$ channel, where the full width of the peak is defined

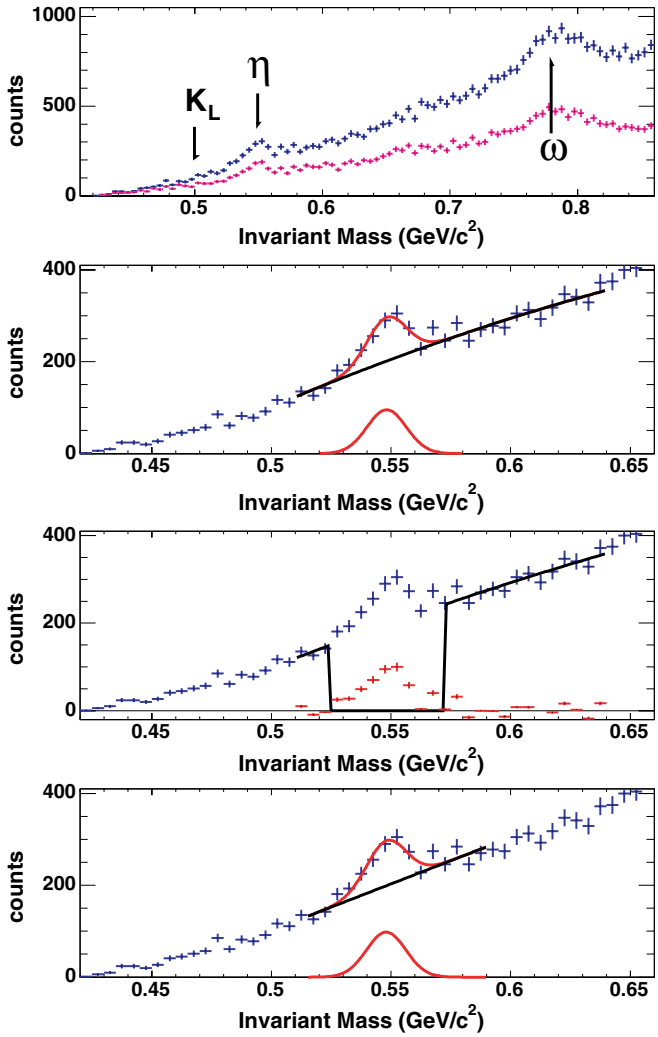

FIG. 7. (Color online) Invariant mass distribution of pion triplets ($\pi^0\pi^+\pi^-$) measured in $p+p$ collisions at $\sqrt{s} = 200$ GeV in the range $m_{\text{inv}} = 0$–0.9 GeV/c^2 (top panel) showing η- and ω-meson peaks. Lower panels showing η-mass region $m_{\text{inv}} = 0.42$–0.66 GeV/c^2 demonstrate three different methods of the extraction of the raw yields. See text for a detailed explanation of each method.

by the EMCal resolution alone, in $\pi^0\pi^+\pi^-$ only 1/4 of the measured mass is derived from an EMCal-based measurement. Given the relatively low p_T of the decay products, tracking has better resolution than the calorimeter. These two effects result in higher accuracy of the mass measurement and smaller width of the peak compared to the $\eta \to \gamma\,\gamma$ analyses.

The raw yield numbers were extracted by simultaneously fitting the signal with a Gaussian function and the background to a quadratic function. The fit was limited to the mass window of $510\ \text{MeV}/c^2 < m_{3\pi} < 640\ \text{MeV}/c^2$. The lower limit is chosen to avoid the region where the $K^0_L \to \pi^0\pi^+\pi^-$ decay (branching ratio BR = 13%) yields an additional signal at and above $m_{K^0_L} = 498\ \text{MeV}/c^2$. The upper limit is chosen at a safe distance from the $\omega \to \pi^0\pi^+\pi^-$ (BR = 89.1%) peak at 782 MeV/c^2 with a width of 20–25 MeV/c^2. An example of the fit is shown in the second panel in Fig. 7. We also compared the result of such a combined signal+background fit with separate fitting of the background. For that, the region under the peak, $530\ \text{MeV}/c^2 < m_{3\pi} < 570\ \text{MeV}/c^2$, was rejected from the fit and the background was approximated by the quadratic function. The function was interpolated and subtracted from the histogram in Fig. 7 (third panel). The histogram counts in the region initially rejected were summed up to calculate the yield.

In addition, simultaneous fitting was done in the restricted window below $m_{3\pi} < 580\ \text{MeV}/c^2$, with the background approximated by a linear function. The same three fits were repeated applying an additional condition in the analysis. Each charged track was required to match a hit in PC3 or in the EMCal in case a track missed the active area of PC3. The resultant invariant mass spectrum is shown by the lower curve in the top panel of Fig. 7. The amplitude of the signal is reduced by about a factor of 2 because many tracks fall outside the acceptance of these two detectors, but the background is also reduced and, more importantly, modified in its shape. The overall significance of the results with and without matching is approximately the same. Signal loss due to matching can be corrected with the simulation with small systematic uncertainty and the results can be compared to deduce the accuracy of the yield extraction procedure. Thus, for each p_T point we obtain six statistically correlated measurements of the raw yields. The first measurement with its statistical error is used in further analysis and the variance of the six measurements provides the estimate of the systematic errors of the yield extraction.

2. *Acceptance and efficiency corrections of the raw η yields*

Similar corrections as described for the $\gamma\,\gamma$ decay channel need to be applied to the $\eta \to \pi^0\pi^+\pi^-$ raw yields. However, for the three-pion analysis, we use the full detector simulation and both corrections, namely the acceptance and the efficiency corrections, are computed at the same time. A MC hadron decay generator was used to produce initial η mesons with a p_T distribution providing satisfactory statistical significance in all bins after acceptance and trigger losses. The full GEANT-based PISA simulation was updated with the three-body decay of the η meson and used to decay η mesons. PISA also performs the full simulation of the PHENIX detector and generates the response of all its subsystems up to the electronics-signal

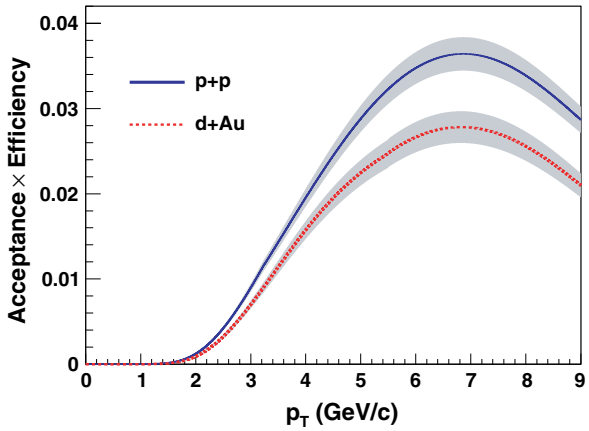

FIG. 8. (Color online) Acceptance×efficiency for the $\eta \to \pi^0\pi^+\pi^-$ as a function of p_T in both d+Au (dashed curve) and p+p (solid curve) collisions at PHENIX in Run-3.

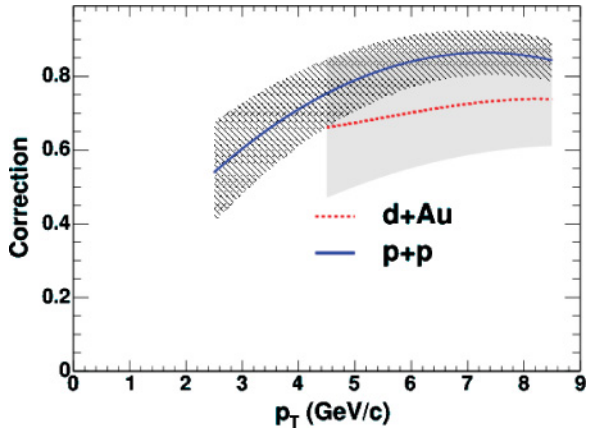

FIG. 10. (Color online) Phase-space density correction for p+p (solid curve) and d+Au (dashed curve) event samples as a function of p_T.

level, which was then processed by standard PHENIX reconstruction software. Special attention was paid to verify that the simulation code represented the real configuration of the detector, and that the π^0 peak parameters in the real data and simulation were consistent with each other. The reconstruction of the simulated data was carried out using the same steps and tools as the real data.

Figure 8 shows the combined efficiency×acceptance as a function of p_T for the three-pion decay analysis. To compare this with the $\gamma\,\gamma$ decay channel reconstruction efficiency one needs to multiply the acceptance curve shown in Fig. 6 with the obtained $\varepsilon_{\eta\to\gamma\,\gamma} = 76\% \pm 3\%$ overall efficiency loss. The three-body decay combined acceptance is significantly lower than the acceptance of the $\gamma\,\gamma$ decay channel. With comparable branching ratios of the two modes the resulting statistics in the three-body decay mode is expected to be smaller. The decrease of the efficiency at high p_T is due to the momentum cut on the $\pi^{\pm}$ to be below 4.0 GeV/c. Above that threshold the track sample is contaminated by products of in-flight decays of long-lived particles with mismeasured momentum.

3. *Phase-space density correction*

The $\eta \to \pi^0\pi^+\pi^-$ decay channel required an additional correction to take into account the uneven distribution of the momenta of the three pions within the kinematically allowed region. Such a distribution, taken from Refs. [65–67], is shown in the left panel of Fig. 9. The vertical axis is the fraction of kinetic energy carried by the π^0 in the η-meson rest frame. The horizontal axis shows the difference between kinetic energies of π^- and π^+ divided by the total in the same system. The left plot of Fig. 9 shows that on average the π^0 meson carries less kinetic energy, and thus momentum, than the two charged π mesons. The right panel shows the PHENIX reconstruction efficiency including geometrical acceptance, high-p_T trigger efficiency (see the next section), and analysis cuts. The latter two effectively select higher momentum π^0 and lower momentum $\pi^{\pm}$ in the lab frame. In the η-meson rest frame these translate into the effect opposite of what is shown in the left panel. To correct for that we used the following approach. The uniform distribution of the phase-space density produced by the simulated event generator was weighted according to the known probabilities of the π-meson momenta to be observed in the η-meson decay. The corresponding correction was deduced by comparing the reconstruction efficiencies with and without applying weights. The systematic uncertainties associated with the measurement of the phase-space density accuracy were thus obtained. This correction is shown in Fig. 10. The correction factor is calculated in the range where data is available.

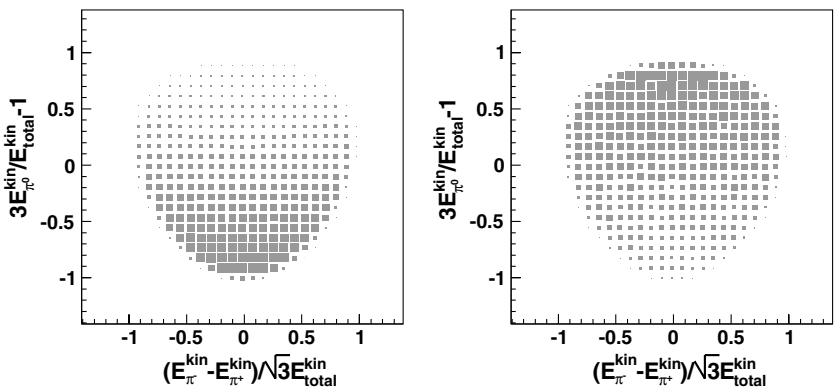

FIG. 9. The phase-space density of the $\eta \to \pi^0\pi^+\pi^-$ decay [65–67] (left panel). PHENIX reconstruction and trigger efficiencies in p+p for the $\eta \to \pi^0\pi^+\pi^-$ decay (right panel).

TABLE IV. Correction factors ($\varepsilon_{\rm trig}/\varepsilon_\eta$), due to the efficiency of the MB trigger for different d+Au centralities [59].

Collision system	Correction factor
d+Au 0–20% central	0.95
d+Au 20–40% semicentral	0.99
d+Au 40–60% semiperipheral	1.03
d+Au 60–88% peripheral	1.04

E. Trigger corrections and absolute cross-section normalization

1. *Minimum-bias trigger efficiency*

The minimum bias trigger does not detect every collision; only a certain fraction $\varepsilon_{\rm trig}$ of the inelastic collisions and a fraction ε_η of the η mesons can be observed. The spectra have to be corrected for both of these effects. The correction factors $\varepsilon_{\rm trig}/\varepsilon_\eta$, determined in Ref. [59] for d+Au collisions, are shown in Table IV. In the case of p+p collisions, as well as in MB d+Au collisions, one can directly determine the inelastic η cross section. Therefore, one does not apply the correction factors mentioned above but rather multiplies the spectra by the total cross section observed by the BBC, found to be 23.0 mb ± 9.7% in Run-3 p+p collisions and 1.99 b ± 0.10 b in Run-3 d+Au collisions [63]. An additional correction has to be applied for the bias of the BBC to high-p_T η. It is found to be 0.79 for p+p [17] and 0.94 for d+Au [63] collisions.

2. *High-p_T γ-trigger efficiency*

The efficiency of the high-p_T trigger has to be studied as well to get η spectra for the γ-triggered data at high transverse momenta, as previously performed for PHENIX π^0 analyses [14,21]. The γ triggers in PHENIX are implemented by adding together amplitudes in 4×4 adjacent EMCal towers during data taking and comparing them to a preset threshold. In the case of p+p the threshold was set to correspond to $E_\gamma = 1.5$ GeV, whereas for d+Au it was set at $E_\gamma = 3.5$ GeV. In the case of Au+Au, triggering was performed by a LVL2 software algorithm run over the MB-triggered events during data taking, such that the number of rejected minimum bias events were recorded. This allowed two different threshold triggers to be employed based on event centrality in Au+Au: $E_\gamma = 1.5$ GeV for the 60–92% peripheral sample and $E_\gamma = 3.5$ GeV for the more central event selections.

The trigger efficiency curves versus the energy of a single photon for two different threshold settings used in p+p and d+Au collisions are shown in the top panel of Fig. 11. Based on these curves, the 2-γ efficiency is calculated as for the previous π^0 analyses [14,21] using the fastMC calculation. For this calculation, the single-photon trigger turn-on curve is represented by an integrated Gaussian for the d+Au analysis and by the integrated sum of two Gaussians for the p+p analysis. In the case of the Au+Au LVL2 triggers, the high-statistics measurement of the single-photon efficiency, which

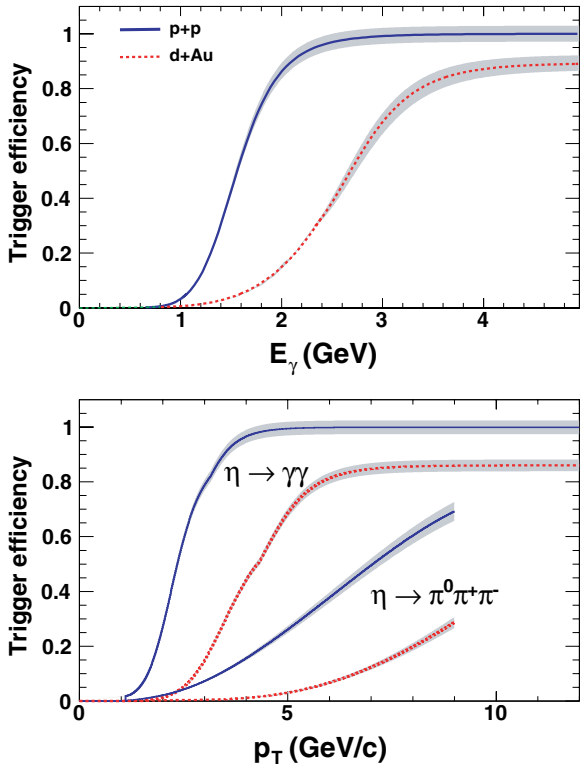

FIG. 11. (Color online) Simulation result for the efficiency of the γ trigger in d+Au collisions. The γ trigger efficiency for a single γ is shown in the top panel for p+p (solid curve) and d+Au (dashed curve). The gray band is the error of the measurement. The lower panel shows the recalculated trigger efficiency for $\gamma\,\gamma$ and $\pi^0\pi^+\pi^-$ channels for both collision systems.

for the central trigger reaches ∼100% above threshold, is used itself as shown in the top panel of Fig. 12. The derived π^0 efficiency is checked by comparing the ratio of the number of π^0 in MB events that carry the trigger flag to the number of π^0 in all MB events. In this way the normalization of the LVL2 data sample relative to the MB data sample is confirmed to be accurate to 2%.

In the same way we determine the $\eta \to \gamma\gamma$ trigger efficiency, which is shown in the lower panels of Figs. 11 and 12. In the $\eta \to \pi^0\pi^+\pi^-$ decay channel where the statistics is very limited, we use the measured single-photon trigger efficiency curves shown in the top panel and full detector MC to determine the efficiency of the trigger. The derived curves for p+p and d+Au are also shown in the lower panel of Fig. 11. One can see that the trigger efficiency plateaus at a p_T of the η about twice the energy of the threshold in the case of the $\gamma\gamma$ decay channel, but in the three-body decay mode where the trigger can only be fired by one of the γ from $\pi^0 \to \gamma\gamma$, it requires the p_T of the η to be approximately four times the threshold. In central Au+Au the η efficiency reaches 50% (∼100%) for η above $p_T = 5$ (7–8) GeV/c, as shown in Fig. 12 (bottom panel). The LVL2 data were used only for p_T regions where the trigger had better than ∼50% η efficiency: $p_T > 5$ GeV/c for the central trigger and $p_T > 2$ GeV/c for peripheral.

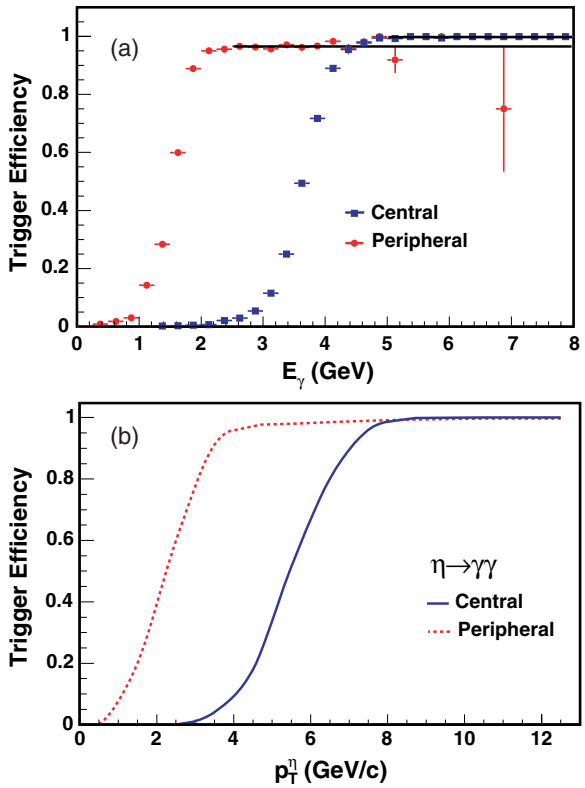

FIG. 12. (Color online) Level-2 trigger photon (top) and η (bottom) efficiencies for central Au+Au ($E_\gamma = 3.5$ GeV threshold) and peripheral Au+Au ($E_\gamma = 1.5$ GeV) collisions as in Fig. 11. For deriving the η efficiencies, the histograms in the top panel were directly used, with the black lines denoting constant fits to the above-threshold asymptotic value, at >99.7% for the central trigger. The central (peripheral) LVL2 η sample was used only above $p_T >$ 5 (2) GeV/c.

3. Cross-section normalization

The invariant cross sections for η production as a function of p_T in MB $p+p$ and $d+$Au collisions are obtained from the measured number of counts in each p_T bin via

$$E\frac{d^3\sigma}{d^3p} \equiv \frac{1}{2\pi\, p_T N_{\rm evt}}\frac{1}{\mathcal{L}}\frac{1}{BR}\frac{1}{Acc(p_T)\varepsilon(p_T)\varepsilon_{\rm trig}(p_T)}\frac{N(\Delta p_T)}{\Delta p_T \Delta y}, \quad (3)$$

where Acc, ε, and $\varepsilon_{\rm trig}$ are the acceptance, reconstruction efficiency, and trigger efficiency, respectively, determined in the previous section; $BR = 0.3943 \pm 0.0026$ is the known $\gamma\gamma$ decay branching ratio of the η meson, and $\mathcal{L}$ is the integrated luminosity obtained using the absolute inelastic cross-section normalization (see Sec. III A). The invariant *yields* as a function of p_T for a given bin in collision centrality in $d+$Au and Au+Au collisions are obtained via

$$\frac{1}{2\pi\, p_T}\frac{d^2N_{\rm cent}}{dp_T dy} \equiv \frac{1}{2\pi\, p_T N_{\rm cent}^{\rm event}}\frac{1}{BR} \times \frac{1}{Acc(p_T)\varepsilon(p_T, {\rm cent})\varepsilon_{\rm trig}(p_T)}\frac{N(\Delta p_T, {\rm cent})}{\Delta p_T \Delta y}. \quad (4)$$

A final bin-shift correction is needed to take into account the fact that the data points of the η spectra are plotted at the center of each given p_T interval (bins whose width is as large as $\Delta p_T = 2$ GeV/c), which, due to the exponentially falling spectrum, does not represent the true physical value of the yield in the interval [68]. Usually, either the correction is applied displacing the x values horizontally (i.e., the center of the p_T bin is decreased) keeping their y value, or the y values are moved vertically (i.e., the yields are decreased) keeping the p_T values at the center of the bin. The second method (yield correction) is preferred here because it facilitates taking bin-to-bin p_T ratios of spectra (with slightly different shapes) from different collisions systems. The net effect of this recipe is a small (few %) shift downwards of the invariant η yields in each p_T bin.

F. Systematic uncertainties

1. $\eta \to \gamma\,\gamma$ analysis ($p+p$ and $d+$Au)

All systematic errors for the $p+p$ and the $d+$Au analysis are summarized in Table V. Hereafter, the errors are categorized by type:

(i) (**A**) point-to-point error uncorrelated between p_T bins,
(ii) (**B**) p_T correlated, all points move in the same direction but not by the same factor,
(iii) (**C**) an overall normalization error in which all points move by the same factor independent of p_T.

The cross-section measurement of the MB trigger has a type-C uncertainty of 9.7% in $p+p$ and 5.2% in $d+$Au. All other systematic errors are of type B, i.e. they are p_T correlated.

The error of the raw yield (peak) extraction was estimated, as described in Ref. [21], calculating the error of the ratio of the integrals of the real and the mixed event distributions in the region of the background fit. The systematic error in peak extraction differs from the systematic error estimated for neutral pions in Ref. [21] because the background in the η region cannot be estimated as well as the background in the π^0 region. This type-B error, estimated to be 4% higher than for pions, becomes dominant at very low transverse momenta due to the small S/B ratio. The error on the acceptance correction includes fiducial cuts on the edges of the EMCal sector as well as cuts around towers that have been determined to be hot or dead. The uncertainty in the MC (GEANT) description of the detector geometry is estimated varying these cuts slightly in the fastMC and in the embedded events (Au+Au). Those variations are found to result in differences in the yields of less than 5%. Different combinations of particle ID cuts were used in the analysis to estimate the uncertainty related to the photon identification. The differences among the various samples are less than 4% for all the different PID cuts for $p+p$ as well as for $d+$Au reactions. The error in the reconstruction efficiency contains this difference. The most important source of uncertainty at high p_T is related to the energy scale. The η peak positions and widths observed in the data are not reproduced to better than 1.5%. An error in the energy scale of 1.5% leads to an error of 4% in the yield at $p_T = 2$ GeV/c

TABLE V. Systematic errors of the η measurement in $p+p$ and $d+$Au (Run-3) for different p_T bins. The error of the peak extraction has a very steep slope at low p_T.

Error source	p_T independent	3 GeV/c	5 GeV/c	10 GeV/c	type
Peak extraction		14.5% ($p+p$), 9.5% ($d+$Au)	6%	6%	B
Geometric acceptance		4.5%	4.5%	4.5%	B
η reconstruction efficiency		1.3%	2.3%	3.6%	B
Global energy scale		5.5%	7.0%	8.4%	B
Energy scale linearity		1.5%	0.4%	4.3%	B
γ-trigger efficiency		9% ($p+p$), - ($d+$Au)	0% ($p+p$), 2.5% ($d+$Au)	0%	B
Conversion correction	2.0%				B
Absolute cross-section normalization	9.7% ($p+p$), 5.2% ($d+$Au)				C

and of 8% at $p_T = 10$ GeV/c. The error of the high-p_T trigger efficiency in $p+p$ is different from in $d+$Au: it amounts to 7.5% at $p_T = 3.5$ GeV/c and becomes negligible at $p_T = 5$ GeV/c (see Sec. III E2).

2. $\eta \to \gamma\gamma$ analysis (Au+Au)

The sources of systematic errors in the Au+Au analysis are listed in Table VI. The main sources of systematic errors in the η measurement are the uncertainties in the yield extraction (10–30%), the yield correction (∼10%), and the energy scale (a maximum of ∼8%). The energy scale uncertainty is basically the same as discussed before for the $p+p$ and $d+$Au analyses. The uncertainty on the raw yield extraction was studied by varying the normalization region of the mixed event background and by comparing yields extracted from 2σ and 3σ integration windows. The yields were found to vary within 10% of the expectation for all centralities. The final results obtained with different PID cut combinations are found to be consistent within ∼8%, and this was the assigned systematic uncertainty for the photon identification procedure. The final combined systematic errors on the spectra are at the level of ∼10–15% (type-A, point to point) and ∼10–15% (type-B, p_T correlated).

TABLE VI. List of systematic uncertainties in the PbSc η measurement in Au+Au collisions (Run-2). Ranges generally correspond to uncertainties from the lower p_T to the higher p_T values of the measurement.

Error source	Percentage error	Type
Raw yield (peak) extraction (point to point)	0–31%	A
Raw yield (peak) extraction (p_T correlated)	10–20%	B
Energy scale	3–8%	B
PID cuts	8%	A
Geometric acceptance	4–2%	B
Trigger efficiency	5–2%	B
Reconstruction efficiency	2%	A

3. $\eta \to \pi^0\pi^+\pi^-$ analysis ($p+p$ and $d+$Au)

Systematic errors for the $\pi^0\pi^+\pi^-$ channel are summarized in Table VII. The $p+p$ and $d+$Au data samples have different systematic errors which are usually larger in $d+$Au. This is due to the larger high-p_T trigger threshold set during $d+$Au data taking. The PC3-EMCal matching uncertainty is used to evaluate peak extraction uncertainty. The dominant systematic uncertainties in the $p+p$ ($d+$Au) measurement are in the yield extraction and the phase-space corrections, with uncertainties of 10–30% (10–30%) and ∼10% (∼25%), respectively. The final combined systematic errors on the spectra are at the level of ∼30% ($p+p$) and ∼40% ($d+$Au).

IV. RESULTS AND DISCUSSION

In this section, the fully corrected spectra for η production differential in p_T in $p+p$, $d+$Au and Au+Au are presented, as well as the nuclear modification factors for $d+$Au and Au+Au collisions. The measured η/π^0 ratio as a function of p_T for the three colliding systems is presented and discussed in comparison with a compilation of world data for hadron-hadron, hadron-nucleus, nucleus-nucleus, and e^+e^- collisions and to phenomenological (PYTHIA and "m_T-scaling") expectations.

A. Transverse momentum spectra ($p+p$, $d+$Au, Au+Au)

The fully corrected spectra for the η meson are shown in Fig. 13 for MB events in proton-proton and deuteron-gold collisions at $\sqrt{s_{NN}} = 200$ GeV. The figure shows the spectra obtained in both the $\eta \to \gamma\gamma$ and $\eta \to \pi^0\pi^+\pi^-$ decay channels. For the $\gamma\gamma$ result, the error bars represent the total error, given by the quadratic sum of the statistical and the systematic uncertainties. For the pion-triplet spectra, the error bars (bands) represent the statistical (systematic) uncertainties. These results agree well in spite of very different analysis approaches and sources of systematic uncertainties. Due to higher acceptance and lower trigger threshold (see Figs. 6, 8, and 11), the $\gamma\gamma$ channel has superior statistics and therefore these results alone are used henceforth.

The invariant yields measured in four different centrality classes in $d+$Au collisions at $\sqrt{s_{NN}} = 200$ GeV are shown

TABLE VII. Systematic errors of the $\eta \to \pi^0\pi^+\pi^-$ measurement in $p+p$ and $d+$Au collisions (Run-3). The first number corresponds to the $p+p$ data and the number in parentheses to $d+$Au in cases where it is different from $p+p$.

Error source	p_T independent	3 GeV/c	4 GeV/c	5 GeV/c	6 GeV/c	7 GeV/c	8 GeV/c	Type
EMCal geometrical acceptance	4% (4%)							C
DC-PC1 acceptance	2% (2%)							B
Acceptance variation	0.5% (3%)							B
PC3-EMCal matching	2% (2%)							B
π^0 selection		3%	3%	3% (3%)	3% (3.5%)	3% (4%)	3% (4%)	B
Conversion uncertainty	3% (3%)							C
EMCal energy resolution		2%	2.5%	3% (5%)	4% (5%)	5% (5%)	5% (5%)	B
EMCal energy scale		3%	3%	3% (4%)	3.5% (4%)	4% (4%)	5% (4.5%)	B
γ-trigger efficiency		5%	5%	5% (5%)	5% (5%)	5% (5%)	4% (4.5%)	B
γ-trigger run-by-run variation	4% (4%)							B
Peak extraction in data (fit)		10%	13%	20% (30%)	13% (20%)	23% (20%)	30% (15%)	A
Peak extraction in data (width)		10%	10%	10% (15%)	10% (15%)	10% (10%)	12% (20%)	A
Peak extraction in simulation	3% (5%)							B
Branching ratio uncertainty	1.8% (1.8%)							C
Phase-space corrections		20%	15%	11% (27%)	8% (24%)	7% (20%)	7% (19%)	B
MB trigger	9.7% (5.2%)							C
Trigger bias	2.5% (1%)							C
Total		28%	26%	29% (45%)	24% (38%)	30% (33%)	36% (35%)	

in Fig. 14. In Fig. 15 the fully corrected invariant spectra for MB and three different centrality classes in Au+Au collisions at $\sqrt{s_{NN}} = 200$ GeV are shown. The error bars represent the quadratic sum of the statistical and the point-to-point systematic uncertainties.

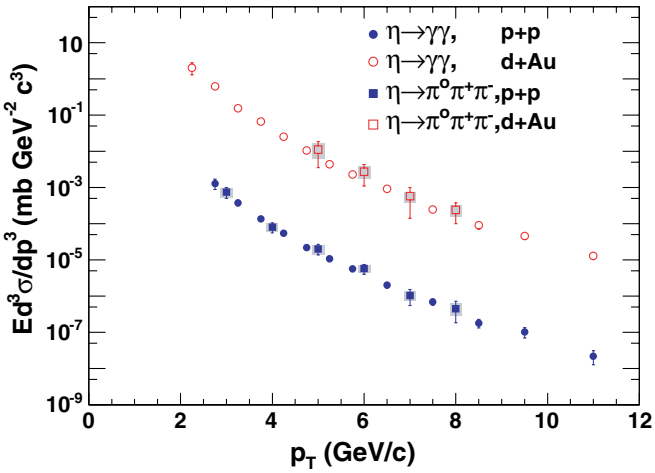

FIG. 13. (Color online) Invariant η cross section as a function of transverse momentum in $p+p$ and $d+$Au collisions at $\sqrt{s_{NN}} = 200$ GeV measured in the $\eta \to \gamma\gamma$ (circles) and $\eta \to \pi^0\pi^+\pi^-$ (squares) decay channels. The error bars of the $\eta \to \gamma\gamma$ are the quadratic sum of statistical and systematic uncertainties. The error bars (bands) of the $\pi^0\pi^+\pi^-$ spectra represent the statistical (systematic) uncertainties of the measurement.

B. Nuclear modification factor in $d+$Au, $R_{d\mathrm{Au}}(p_T)$

Medium effects in $d+$A collisions are quantitatively determined using the *nuclear modification factor* given as the ratio of the measured $d+$A invariant yields, d^2N_{dA}/dp_Tdy, over the measured $p+p$ cross sections, $d^2\sigma_{pp}/dp_Tdy$, scaled by the nuclear thickness function $\langle T_{dA}\rangle$ in the centrality bin under

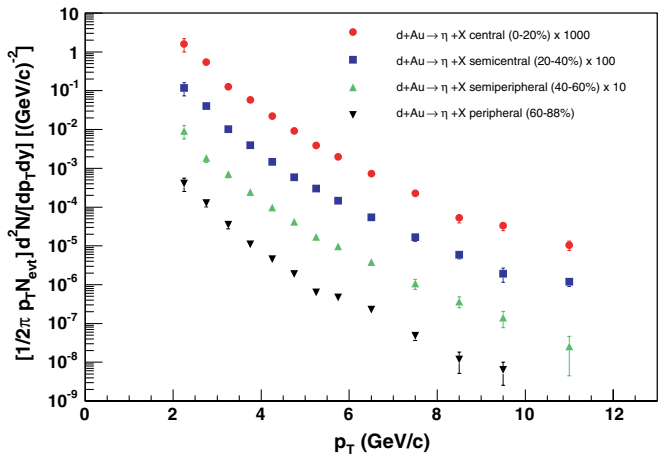

FIG. 14. (Color online) Invariant η yields as a function of transverse momentum in $d+$Au collisions at $\sqrt{s_{NN}} = 200$ GeV in four different centralities (0–20, 20–40, 40–60, 60–88%). The error bars are the quadratic sum of statistical and all systematic uncertainties. For clarity, the data points are scaled vertically as noted in the figure.

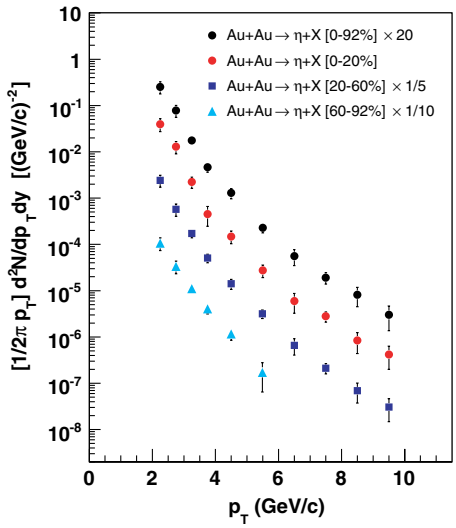

FIG. 15. (Color online) Invariant η yields as a function of transverse momentum in Au+Au collisions at $\sqrt{s_{NN}} = 200$ GeV for MB and three centralities (0–20, 20–60, 60–92%). The error bars are the quadratic sum of statistical and point-to-point systematic uncertainties. For clarity, the data points are scaled vertically as noted in the figure.

consideration:

$$R_{dA}(p_T) = \frac{d^2N_{dA}/dy\,dp_T}{\langle T_{dA}\rangle \cdot d^2\sigma_{pp}/dy\,dp_T}. \tag{5}$$

Deviations from $R_{dA}(p_T) = 1$ quantify the degree of departure of the hard d+A yields from an incoherent superposition of *NN* collisions. The values of the nuclear thickness function for different centralities are obtained in a Glauber MC calculation and tabulated in Table II. The resulting $R_{dA}(p_T)$ for η mesons in d+Au collisions is plotted for different centralities in Fig. 16.

The data points at lower transverse momenta have large statistical errors. This is caused by the poor S/B ratio of the η peak in the sample that is not triggered with the γ trigger. The systematic uncertainties shown in the plot are computed propagating the experimental uncertainties in the p+p and d+Au measurements described in Sec. III F. Some of these uncertainties cancel out when calculating the nuclear modification factor [Eq. (5)]. The error due to the η reconstruction efficiency as well as the error due to uncertainties in the energy scale are very similar for the measurement of η mesons in p+p and d+Au collisions as the measured data have been taken in the same experimental run, and they cancel almost completely in the ratio.

In the case of *minimum bias* d+Au collisions, the nuclear modification factor, shown in Fig. 17, is more simply defined as the ratio of d+Au over p+p *cross sections* normalized by the total number of nucleons ($2 \cdot A$ for a d+A collision) with $A = 197$ for a gold nucleus:

$$R_{dA}(p_T) = \frac{d\sigma_{dA}}{2 \cdot A \cdot d\sigma_{pp}}. \tag{6}$$

All the d+Au nuclear modification factors shown in Figs. 16 and 17 are approximately 1 and show a very weak p_T and/or centrality dependence. Similar trends have been observed for π^0 production [17]. As shown in the comparison plot of Fig. 18, the π^0 nuclear modification factors indicate

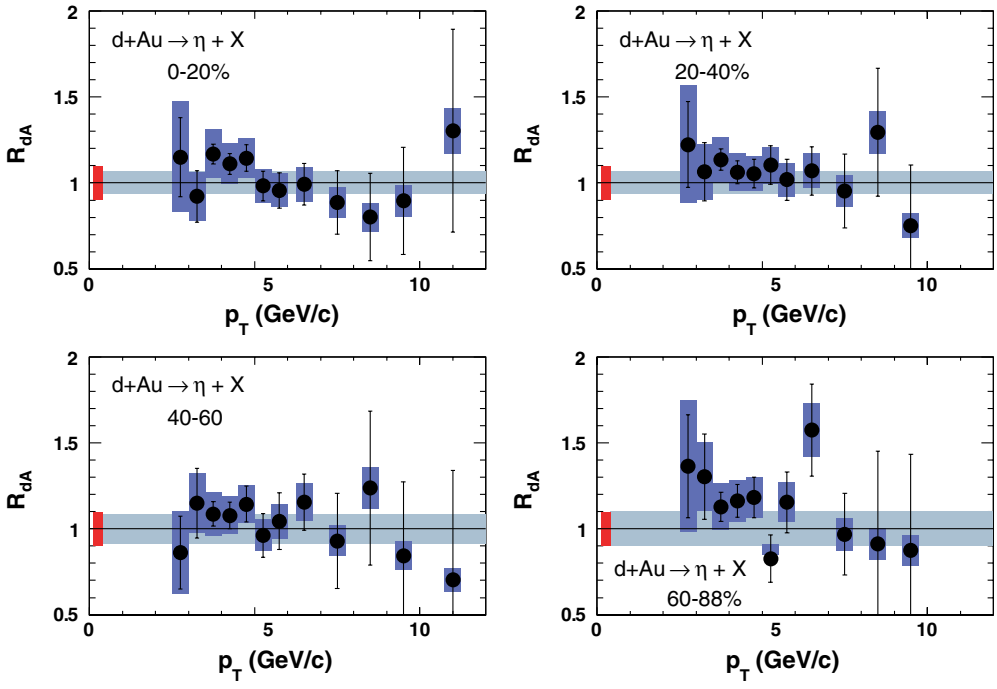

FIG. 16. (Color online) Nuclear modification factors for η production for four d+Au centralities: 0–20, 20–40, 40–60, 60–88%. The error bars (bands) around each point are the statistical (type-B systematic) uncertainties. The error band at $R_{dA} = 1$ indicates the uncertainty in $\langle T_{dA}\rangle$ for each centrality. The error box at $R_{dA} = 1$ indicates the p+p cross-section uncertainty of 9.7%.

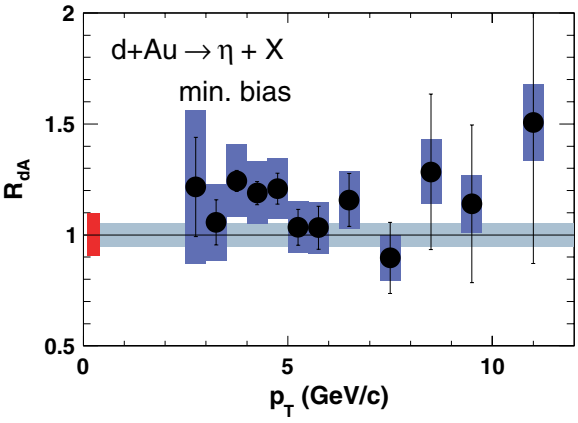

FIG. 17. (Color online) Nuclear modification factor R_{dA} for η mesons as a function of p_T for minimum-bias $\sqrt{s_{NN}} = 200$ GeV d+Au collisions. The uncertainties are the same described in Fig. 16.

small shape modifications with centrality, with a possible Cronin enhancement on the level of 10% around 4 GeV/c disappearing for $p_T > 10$ GeV/c. At high p_T the π^0 MB result can be described well by next-to-leading-order pQCD calculations [27,69] without implementation of the Cronin effect. The contribution of (anti-)shadowing effects [26,27] in the η or π^0 production is very small, as expected for this kinematical region with $x_T = 2p_T/\sqrt{s} \approx 0.02$–$0.2$.

The small role of initial-state cold nuclear effects observed in the midrapidity spectra of neutral mesons at high p_T is also consistent with other similar observations in d+Au reactions at $\sqrt{s_{NN}} = 200$ GeV such as (i) the absence of significant nuclear modifications in the yields of J/Ψ compared to p+p collisions [63] and (ii) the very similar characteristics of near-side and away-side jetlike correlations in p+p and d+Au [70]. Those results indicate that the nuclear medium has little influence on the hard processes in d+Au collisions at top RHIC energies and $y = 0$.

C. Nuclear modification factor in Au+Au, $R_{AA}(p_T)$

The nuclear modification factor, $R_{AA}(p_T)$, for η production in each centrality class in Au+Au collisions is computed using the standard formula:

$$R_{AA}(p_T) = \frac{d^2N_{AA}/dydp_T}{\langle T_{AA}\rangle \cdot d^2\sigma_{pp}/dydp_T}, \qquad (7)$$

where (i) the Au+Au spectra $d^2N/dydp_T$ are used in the numerator (Fig. 15), (ii) the p+p invariant spectrum $d^2\sigma/dydp_T$ (Fig. 13) is used in the denominator, and (iii) $\langle T_{AA}\rangle$ are the values of the average Glauber overlap function for each Au+Au centrality (Table II). The $R_{AA}(p_T)$ is computed taking the bin-to-bin ratio of Au+Au and p+p spectra and propagating the corresponding uncertainties. Only the acceptance uncertainty (~5%) cancels in the Au+Au/p+p ratio of spectra. Figure 19 compares the nuclear modification factor for η measured in central (0–20%), semicentral (20–60%) and peripheral (60–92%) Au+Au collisions. The error bars are the total point-to-point errors (including type-**A** systematic and statistical uncertainties) of the Au+Au and p+p measurements. The error bands on the left are the uncertainties in $\langle T_{AuAu}\rangle$ for each centrality class. The error box on the right is the Run-3 p+p cross-section uncertainty of 9.7%. As observed for high-p_T π^0 [19,21], the Au+Au η yields are consistent with the expectation of independent NN scatterings in peripheral reactions ($R_{AA} \approx 1$) but they are increasingly depleted with respect to this expectation for more central collisions. There is no p_T dependence of R_{AA}, as seen also for neutral pions.

Figure 20 contrasts the nuclear modification factors measured in central Au+Au at $\sqrt{s_{NN}} = 200$ GeV for η, π^0 [19,21], and γ [48]. Whereas direct photons are unsuppressed compared to the scaled reference given by a NLO pQCD calculation [48,71] that reproduces the PHENIX p+p γ results well [49], neutral pions and η are suppressed by a similar factor of ~5 compared to the corresponding cross sections measured in p+p. Within the current uncertainties, light-quark neutral mesons at RHIC show a flat suppression in the range $p_T \approx 4$–15 GeV/c, independent of their mass (note that the η is ~4 times heavier than the π^0). Those results are in agreement with parton energy loss calculations in a system with initial effective gluon densities of the order $dN^g/dy \sim 1000$ (solid curve in the figure) [37]. The equal suppression of η and π^0 mesons and the agreement with parton energy loss calculations suggest that the final fragmentation of the quenched parton into a leading meson occurs in the vacuum according to the same probabilities (fragmentation functions) that govern high-p_T hadroproduction in more elementary systems (p+p, e^+e^-). This conclusion is examined in more detail in the next two sections.

D. Ratio of η to π^0 (p+p, d+Au, Au+Au)

A useful way to determine possible differences in the suppression pattern of π^0 and η is to study the centrality dependence of the η/π^0 ratio, $R_{\eta/\pi^0}(p_T)$, in d+Au and Au+Au reactions and compare it with the values measured in more elementary systems (p+p, e^+e^-). The "world" η/π^0 ratio in hadronic and proton-nucleus collisions increases rapidly with p_T and flattens out above $p_T \approx 2.5$ GeV/c at values R_{η/π^0} ~0.40–0.50 (see Sec. IV E1). Likewise, in electron-positron annihilations at the Z pole ($\sqrt{s} = 91.2$ GeV), $R_{\eta/\pi^0} \sim 0.5$ for *energetic* η and π^0 (with $x_p = p_{\rm hadron}/p_{\rm beam} > 0.4$, consistent with the range of scaled momenta $\langle z\rangle = p_{\rm hadron}/p_{\rm jet}$ considered here), as discussed in Sec. IV E2. It is interesting to test if this ratio is modified in any way by initial- and/or final-state effects in d+Au and Au+Au collisions at RHIC energies.

The production ratio of η and π^0 mesons is shown in Fig. 21 for p+p and in Fig. 22 for d+Au (MB and four centrality classes). The ratio is calculated point by point for the d+Au measurements, propagating the corresponding errors. In the p+p case, a fit to the π^0 spectrum [21] was used. All the ratios are consistent with the PYTHIA [72] curve for p+p at $\sqrt{s} = 200$ GeV (dashed line, see discussion in Sec. IV E1) with an asymptotic $R^{\infty}_{\eta/\pi^0} = 0.5$ value.

Figure 23 shows the $R_{\eta/\pi^0}(p_T)$ ratio for MB and three Au+Au centralities, obtained using the latest PHENIX π^0 spectra [21] and removing those systematic uncertainties that

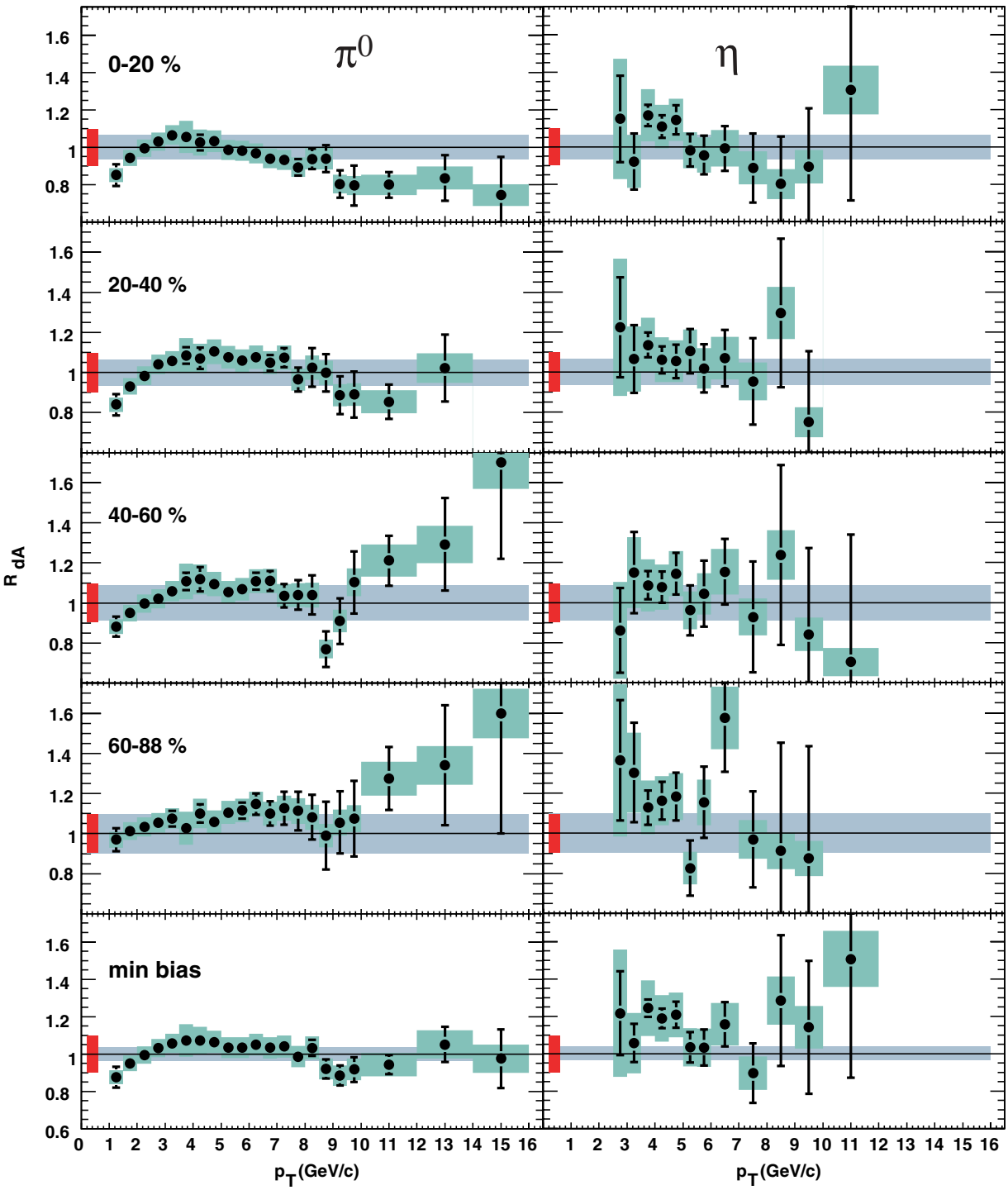

FIG. 18. (Color online) Nuclear modification factor $R_{\mathrm{dA}}(p_T)$ for π^0 (left) and η (right) production in different centrality selections and MB d+Au data. The bands around the data points show systematic uncertainties which can vary with p_T (type-B errors). The shaded band around unity indicates the $\langle T_{dA}\rangle$ uncertainty and the small box on the left side of the data points indicates the normalization uncertainty of the p+p total inelastic cross section.

cancel in the ratio. The $R_{\eta/\pi^0}(p_T)$ data for Au+Au is compared to a PYTHIA [72] calculation that reproduces the hadronic collision data well (see the next section). Within uncertainties, all the ratios are consistent with $R_{\eta/\pi^0} \approx 0.5$ (dashed line) and show no collision system, centrality, or p_T dependence. A simple fit to a constant above $p_T = 2$ GeV/c yields the following ratios:

(i) R_{η/π^0} (Au+Au cent) $= 0.40 \pm 0.04$ (stat) ± 0.02 (syst), χ^2/ndf $= 0.48$

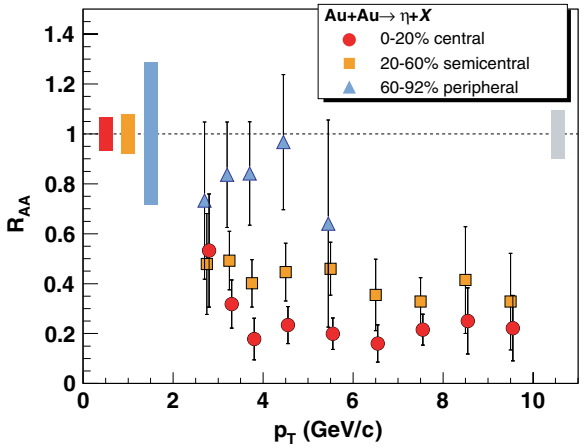

FIG. 19. (Color online) Nuclear modification factors for η in three Au+Au centralities (0–20, 20–60, 60–92%). The errors bars are point-to-point uncertainties. The absolute normalization error bands at $R_{AA} = 1$ are (i) the uncertainties in $\langle T_{AA} \rangle$ for each centrality (left side) and (ii) the p+p cross-section normalization uncertainty of 9.7% (right side). The $R_{AA}(p_T)$ for peripheral/central Au+Au have been slightly displaced to the left/right (±50 MeV/c) along the p_T axis to improve the clarity of the plot.

(ii) R_{η/π^0} (Au+Au semicent) = 0.39 ± 0.03 (stat) ± 0.02 (syst), χ^2/ndf = 0.26

(iii) R_{η/π^0} (Au+Au periph) = 0.40 ± 0.04 (stat) ± 0.02 (syst), χ^2/ndf = 0.42

(iv) R_{η/π^0} (p+p)= 0.48 ± 0.02 (stat) ± 0.02 (syst), χ^2/ndf = 0.89

(v) R_{η/π^0} (d+Au)= 0.47 ± 0.02 (stat) ± 0.02 (syst), χ^2/ndf = 0.84.

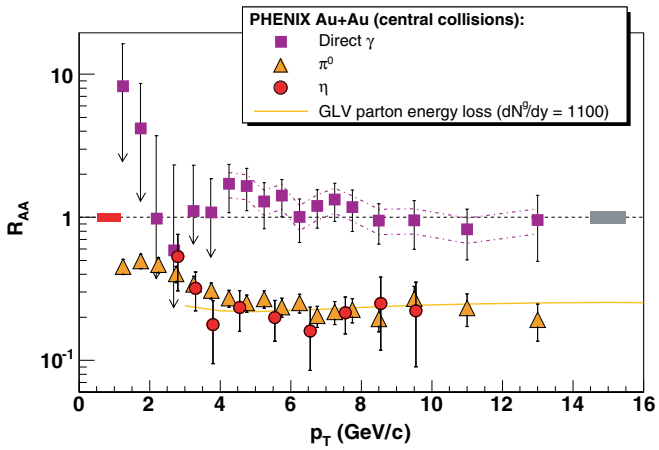

FIG. 20. (Color online) $R_{AA}(p_T)$ measured in central Au+Au at $\sqrt{s_{NN}} = 200$ GeV for η, π^0 [19,21], and for direct γ [48]. The error bars include all point-to-point uncertainties. The error bands at $R_{AA} = 1$ have the same meaning as in Fig. 19. The baseline p+$p \rightarrow \gamma + X$ reference used is a NLO pQCD calculation [48,71] that reproduces our own data well [49], with theoretical (scale) uncertainties indicated by the dash-dotted lines around the points. The solid yellow curve is a parton energy loss prediction for the suppression factor of leading pions in a medium with initial gluon density $dN^g/dy = 1100$ [37].

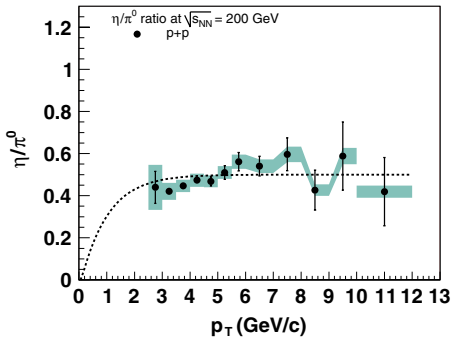

FIG. 21. (Color online) Ratio η/π^0 measured in p+p collisions at $\sqrt{s} = 200$ GeV. The error bars represent the point-to-point errors; the boxes represent the systematic uncertainties. The dashed line is the prediction of PYTHIA [72] for p+p at this center-of-mass energy.

E. World data on the η/π^0 ratio in high-energy particle collisions

In this last section of the article, we present a compilation of experimental η/π^0 ratios as a function of transverse momentum, $R_{\eta/\pi^0}(p_T)$, measured in different hadronic and nuclear colliding systems in a wide range of center-of-mass energies ($\sqrt{s_{NN}} \approx$ 3–1800 GeV). The collected world data on η/π^0 ratios includes (i) hadron-hadron collisions (26 p+p, p+$\bar{p}$, $\pi^{\pm}$+p data sets), (ii) hadron-nucleus collisions (17 $p, \pi^{\pm}$+A sets), and (iii) nucleus-nucleus collisions (7 A+A data sets).

In addition, we present also the $R_{\eta/\pi^0}(x_p)$ ratio obtained from inclusive π^0 and η cross sections in e^+e^- as a function of scaled momentum $x_p = 2\, p_{\rm had}/\sqrt{s}$ measured by the four LEP experiments at the Z pole ($\sqrt{s} = 91.2$ GeV). In all cases, the ratio R_{η/π^0} increases rapidly with p_T (or x_p) and saturates at $R_{\eta/\pi^0} \approx 0.4$–$0.5$ above $p_T \approx 3$ GeV/c ($x_p \approx 0.3$). The experimental $R_{\eta/\pi^0}(p_T)$ ratios are also compared to PYTHIA and to m_T-scaling expectations. PHENIX p+p, d+Au, and

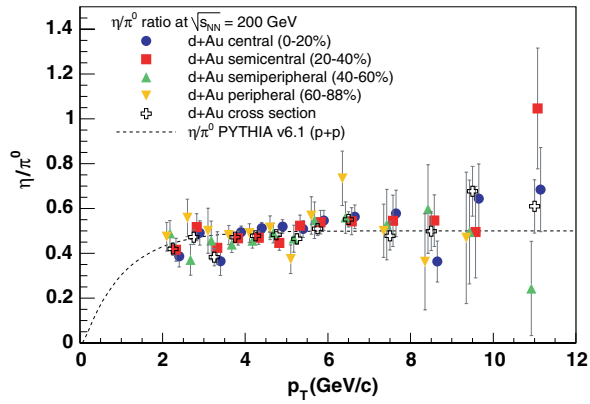

FIG. 22. (Color online) Ratio η/π^0 measured in different centralities in d+Au collisions at $\sqrt{s_{NN}} = 200$ GeV. The error bars represent all point-to-point uncertainties. The dashed line is the prediction of PYTHIA [72] for p+p at this center-of-mass energy. A few $R_{\eta/\pi^0}(p_T)$ ratios have been slightly displaced to the left or right (±<150 MeV/c) along the p_T axis to improve the clarity of the plot.

TABLE VIII. Hadron-hadron collisions with a published η/π^0 ratio and/or η and π^0 spectra. For each reaction we quote: the center-of-mass energy $\sqrt{s}$ (and $p_{\rm lab}$ for fixed-target experiments), the p_T and $x_T = 2p_T/\sqrt{s}$ ranges of the measurement (the x_T values are not quoted for "soft" spectra below $p_T = 1$ GeV/c), and the average η/π^0 ratio above $p_T = 2$ GeV/c obtained by fitting $R_{\eta/\pi^0}(p_T > 2\ \text{GeV}/c)$ to a constant.

System	$\sqrt{s}$ (GeV)	$p_{\rm lab}$ (GeV/c)	p_T range (GeV/c)	x_T range	$R_{\eta/\pi^0}(p_T > 2\ \text{GeV}/c)$	Authors	Collab./Exp.	Ref.
$p+p$	13.8	100	1.6–2.4	0.3–0.4	0.52 ± 0.13	Donaldson 78	FNAL M2	[79]
π^++p	13.8	100	1.6–3.0	0.3–0.4	0.49 ± 0.10	Donaldson 78	FNAL M2	[79]
π^-+p	13.8	100	2.0–3.0	0.3–0.4	0.41 ± 0.13	Donaldson 78	FNAL M2	[79]
π^++p	19.4	200	2.0–3.5	0.2–0.4	0.40 ± 0.07	Donaldson 78	FNAL M2	[79]
π^-+p	19.4	200	1.5–4.0	0.2–0.4	0.43 ± 0.04	Donaldson 78	FNAL M2	[79]
$p+p$	19.4	200	2.0–3.5	0.2–0.4	0.42 ± 0.04	Donaldson 78	FNAL M2	[79]
$p+p$	23.0	280	4.0–5.5	0.2–0.4	0.60 ± 0.04	Bonesini 88	CERN WA70	[80]
π^++p	23.0	280	4.0–5.5	0.2–0.4	0.43 ± 0.05	Bonesini 88	CERN WA70	[80]
π^-+p	23.0	280	4.0–5.5	0.2–0.4	0.57 ± 0.06	Bonesini 88	CERN WA70	[80]
$p+p$	24.3		2.5–4.0	0.2–0.3	0.45 ± 0.06	Antille 87	CERN UA6	[81]
$\bar{p}$+p	24.3		2.5–4.0	0.2–0.3	0.48 ± 0.04	Antille 87	CERN UA6	[81]
$p+p$	27.5	400	0.2–1.6	—	—	Aguilar 91	NA 27	[82]
$p+p$	30.6		0.8–3.0	~0.1–0.2	0.55 ± 0.04	Amaldi 79	ISR	[83]
$p+p$	30.6		3.0–4.0	0.2–0.3	0.54 ± 0.05	Kourkoumelis 79	ISR	[42]
$p+p$	31.6	530	3.0–8.0	0.2–0.5	0.41 ± 0.03	Apanasevich 02	FNAL 706	[84]
$p+p$	38.8	800	3.0–8.0	0.1–0.4	0.44 ± 0.03	Apanasevich 02	FNAL 706	[84]
$p+p$	52.7		3.0–6.0	0.1–0.3	0.58 ± 0.03	Kourkoumelis 79	ISR	[42]
$\bar{p}$+p	53.0		2.5–4.0	0.1–0.2	0.53 ± 0.03	Akesson 85	ISR AFS	[85]
$p+p$	53.0		2.5–4.0	0.1–0.2	0.55 ± 0.02	Akesson 85	ISR AFS	[85]
$p+p$	53.2		3.0–6.0	0.1–0.2	0.54 ± 0.03	Amaldi 79	ISR	[83]
$p+p$	62.4		3.0–11.0	0.2–0.4	0.55 ± 0.03	Kourkoumelis 79	ISR AFS	[42]
$p+p$	63.0		0.2–1.5	—	(0.07 ± 0.055)	Akesson 86	ISR AFS	[86]
$p+p$	63.0		2.0–4.0	0.06–0.13	0.47 ± 0.01	Akesson 83	ISR AFS	[87]
$p+p$	200		2.0–12.0	0.02–0.12	0.48 ± 0.03	S. S. Adler 07	PHENIX	This work
$\bar{p}$+p	540		3.0–6.0	0.01–0.02	0.60 ± 0.04 (stat) $\pm$ 0.15 (syst)	Banner 85	CERN UA2	[88]
$\bar{p}$+p	1800		12.0	0.01	1.02 ± 0.15 (stat) $\pm$ 0.23 (syst)	Abe 93	CDF	[43]

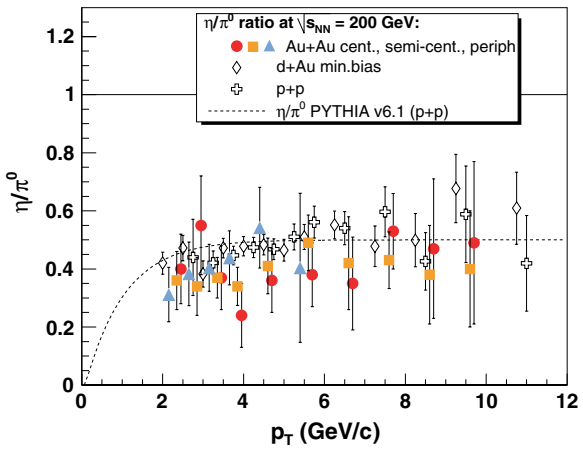

FIG. 23. (Color online) Au+Au R_{η/π^0} ratio in MB and three centrality classes (0–20, 20–60, 60–92%) as a function of p_T compared to the ratio in d+Au and $p+p$ collisions. The error bars include all point-to-point errors. The dashed line is the prediction of PYTHIA [72] for $p+p$ at this center-of-mass energy. A few $R_{\eta/\pi^0}(p_T)$ ratios have been slightly displaced to the left or right ($\pm$50 MeV/c) along the p_T axis to improve the clarity of the plot.

Au+Au η/π^0 ratios at $\sqrt{s} = 200$ GeV are found to be consistent with the obtained world data on R_{η/π^0}.

1. η/π^0 ratio in hadron-hadron, hadron-nucleus, and nuclear collisions ($\sqrt{s} \approx$ 3–1800 GeV)

In Tables VIII, IX, and X we list all data sets with published η and π^0 spectra and/or published $R_{\eta/\pi^0}(p_T)$ ratios in hadron-hadron, hadron-nucleus, and nucleus-nucleus collisions that we have found in the literature. Most of those measurements are performed around midrapidity. Roughly half of the $R_{\eta/\pi^0}(p_T)$ listed have been directly taken from the original works whose references are provided in the data tables. A few others have been constructed by taking the ratio of the published π^0 and η invariant cross-section spectra measured at the same $\sqrt{s}$. In the latter case, the error in the ratio has been computed by adding statistical and systematic uncertainties quadratically. There were a few cases where the p_T binning of the η spectrum did not match that of the π^0. In these cases, the π^0 spectrum was fitted with a functional form that reproduced the data well (usually a modified power law of

TABLE IX. Hadron-nucleus collisions with a published η/π^0 ratio and/or η and π^0 spectra. For each reaction we quote: the center-of-mass energy $\sqrt{s_{NN}}$ (and $p_{\rm lab}$ for fixed-target experiments), the p_T and $x_T = 2p_T/\sqrt{s}$ ranges of the measurement (the x_T values are not quoted for "soft" spectra below $p_T = 1$ GeV/c), and the average η/π^0 ratio above $p_T = 2$ GeV/c obtained by fitting $R_{\eta/\pi^0}(p_T > 2\ \text{GeV}/c)$ to a constant.

System	$\sqrt{s_{NN}}$ (GeV)	$p_{\rm lab}$ (GeV/c)	p_T range (GeV/c)	x_T range	$R_{\eta/\pi^0}(p_T >$ 2 GeV/c)	Authors	Collab./Exp.	Ref.
p+Be	19.4	200	2.5–4.0	0.2–0.4	0.28 ± 0.15	Povlis 83	FNAL E629	[89]
p+C	19.4	200	2.0–5.0	0.2–0.5	0.58 ± 0.05	Povlis 83	FNAL E629	[89]
p+Al	19.4	200	2.0–3.0	0.2–0.3	0.40 ± 0.18	Povlis 83	FNAL E629	[89]
π^-+C	19.4	200	2.0–4.0	0.2–0.5	0.32 ± 0.11	Povlis 83	FNAL E629	[89]
p+Be	23.8	300	2.5–5.0	0.2–0.4	0.47 ± 0.03	Deschamps 85	FNAL E515	[90]
p+Be	29.1	450	0.1–1.0	—	—	Agakichiev 98	TAPS/CERES	[91]
p+Au	29.1	450	0.1–1.2	—	—	Agakichiev 98	TAPS/CERES	[91]
p+Be	29.1	450	0.2–1.6	—	—	Tikhomirov 95	HELIOS	[92]
p+Be	30.7	500	4.0–7.0	0.3–0.5	0.40 ± 0.06	Alverson 93	FNAL E706	[93]
π^-+Be	30.7	500	4.0–8.0	0.2–0.5	0.43 ± 0.05	Alverson 93	FNAL E706	[93]
π^-+p	31.1	515	3.0–8.0	0.1–0.5	0.41 ± 0.05	Apanasevich 03	FNAL 706	[94]
π^-+Be	31.1	515	3.0–8.0	0.1–0.5	0.48 ± 0.01	Apanasevich 03	FNAL 706	[94]
π^-+Cu	31.1	515	3.0–8.0	0.1–0.5	0.50 ± 0.02	Apanasevich 03	FNAL 706	[94]
p+Be	31.6	530	3.0–8.0	0.1–0.5	0.42 ± 0.01	Apanasevich 03	FNAL 706	[94]
p+Cu	31.6	530	3.0–8.0	0.1–0.5	0.42 ± 0.02	Apanasevich 03	FNAL 706	[94]
p+Be	38.8	800	3.0–8.0	0.1–0.4	0.42 ± 0.01	Apanasevich 03	FNAL 706	[94]
p+Cu	38.8	800	3.0–8.0	0.1–0.4	0.45 ± 0.03	Apanasevich 03	FNAL 706	[94]
d+Au	200		2.0–12.0	0.02–0.1	0.47 ± 0.03	S. S. Adler 07	PHENIX	This work

the form discussed in Ref. [73]) and the η/π^0 ratio was then obtained by dividing the η spectrum data points by the values of the π^0 function at each point. In this case, the error was computed by dividing the quoted η error by the function value at that point. The uncertainty arising from the π^0 spectrum fit was obtained by computing the minimum and maximum ratio values at each point. Both errors were then added in quadrature.

In Tables VIII, IX and X, together with the general info on the collected data sets, we indicate for each measurement the approximate p_T and $x_T = 2p_T/\sqrt{s}$ ranges, as well as the average value of R_{η/π^0} at high p_T, obtained by fitting the data to a constant above $p_T = 2$ GeV/c. With the exception of the higher energy data ($\sqrt{s_{NN}} \gtrsim 100$ GeV), most of the experimental ratios have been measured in a fractional momentum range $x_T \approx 0.1$–0.3 where the parton distribution functions are dominated by valence quarks (rather than gluons) and, hence, the produced high-p_T π^0 and η mesons come largely from $q, \bar{q}$ fragmentation. Figures 24, 25, and 26 show the corresponding $R_{\eta/\pi^0}(p_T)$ ratios for each type of colliding system. All the ratios show a rapid increase with p_T and level off at $R_{\eta/\pi^0} \approx 0.4$–$0.5$ above $p_T \approx 3$ GeV/c. No difference is observed for different colliding systems. The PHENIX $p+p$, d+Au, and Au+Au high-p_T data presented in the previous section are consistent with those ratios. A fit of the PHENIX ratios to a constant gives $R_{\eta/\pi^0} = 0.47 \pm 0.03$ for both $p+p$ and d+Au and, slightly lower but still consistent, $R_{\eta/\pi^0} = 0.40 \pm 0.04$ for Au+Au. Together with the data points in Figs. 24–26, we also plot two phenomenological curves with PYTHIA 6.131 [72] based on the Lund fragmentation model [74,75], and on $m_{\rm T}$-scaling expectations for the η/π^0 ratio in $p+p$ collisions at $\sqrt{s} =$ 200 GeV.

a. Lund string fragmentation. The fragmentation mechanism in PYTHIA is based on the phenomenological Lund string

TABLE X. Nucleus-nucleus collisions with a published η/π^0 ratio and/or η and π^0 spectra. For each reaction we quote: the center-of-mass energy $\sqrt{s_{NN}}$ (and $p_{\rm lab}$ for fixed-target experiments), the p_T and $x_T = 2p_T/\sqrt{s_{NN}}$ ranges of the measurement (the x_T values are not quoted for "soft" spectra below $p_T = 1$ GeV/c), and the average η/π^0 ratio above $p_T = 2$ GeV/c obtained by fitting $R_{\eta/\pi^0}(p_T > 2\ \text{GeV}/c)$ to a constant.

System	$\sqrt{s_{NN}}$ (GeV)	$p_{\rm lab}$ (GeV/c)	p_T range (GeV/c)	x_T range	$R_{\eta/\pi^0}(p_T > 2$ GeV/c)	Authors	Collab./Exp.	Ref.
C+C	2.7	2.0	0.0–0.8	—	—	Averbeck 97	GSI TAPS	[95]
Ca+Ca	2.7	2.0	0.0–0.7	—	—	Averbeck 03	GSI TAPS	[96]
Ni+Ni	2.7	1.9	0.0–0.7	—	—	Averbeck 03	GSI TAPS	[96]
Pb+Pb	17.3	158	0.6–2.6	$\sim$0.1–0.3	0.53 ± 0.21	Aggarwal 00	CERN WA98	[97]
S+S	19.4	200	0.5–1.5	0.1–0.2	0.21 ± 0.06	Albrecht 95	CERN WA80	[98]
S+Au	19.4	200	0.5–3.5	0.1–0.3	0.61 ± 0.14	Albrecht 95	CERN WA80	[98]
Au+Au	200		2.0–10.0	0.02–0.1	0.40 ± 0.04	S. S. Adler 07	PHENIX	This work

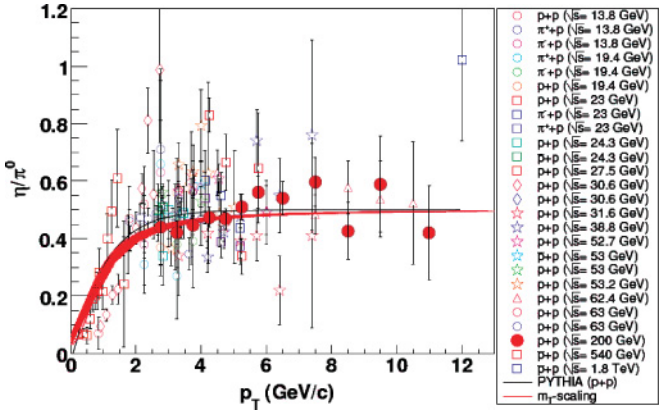

FIG. 24. (Color online) Values of the R_{η/π^0} ratios as a function of p_T measured in the hadron-hadron collisions reported in Table VIII. The black curve is the prediction of PYTHIA [72] for the ratio in $p+p$ at $\sqrt{s} = 200$ GeV, and the red shaded area indicates the empirical m_T-scaling prescription Eq. (10) with fixed $a = 1.2$, power-law exponent $n = 10$–14, and an asymptotic $R^{\infty}_{\eta/\pi^0} = 0.5$ ratio.

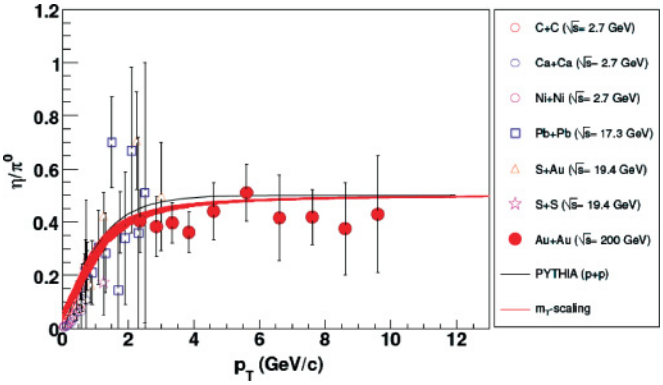

FIG. 26. (Color online) Values of the R_{η/π^0} ratios as a function of p_T measured in the nucleus-nucleus collisions reported in Table X. The black curve is the prediction of PYTHIA [72] for the ratio in $p+p$ at $\sqrt{s} = 200$ GeV, and the red shaded area indicates the empirical m_T-scaling prescription Eq. (10) with fixed $a = 1.2$, power-law exponent $n = 10$–14, and an asymptotic $R^{\infty}_{\eta/\pi^0} = 0.5$ ratio.

scheme [74,75] that considers the color field between the partons to be the fragmenting entity rather than the quarks and gluons themselves. The string is viewed as a color flux tube formed by gluon self-interaction between the partons. As the partons move apart the potential energy stored in the string increases. At some point the string breaks via the production of new $q\bar{q}$ pairs according to the probability of a quantum-mechanical tunneling process, $\exp(-\pi\, m^2_{\mathrm{q,T}}/\kappa)$, which depends on the transverse mass squared ($m^2_{\mathrm{q,T}} = m^2 + {p_T}^2$) and the string tension $\kappa \approx 1$ GeV/fm ≈ 0.2 GeV^2. The string breakup process proceeds repeatedly into color singlet systems as long as the invariant mass of the string pieces exceeds the on-shell mass of a hadron (each hadron corresponding to a small piece of string with a quark at one end and an antiquark at the other). At each branching,

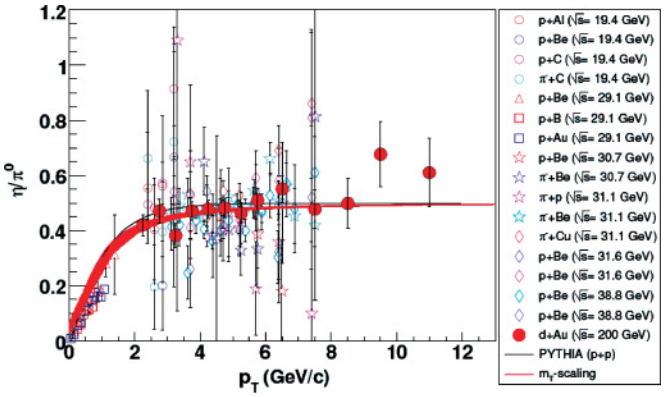

FIG. 25. (Color online) Values of the R_{η/π^0} ratios as a function of p_T measured in the hadron-nucleus collisions reported in Table IX. The black curve is the prediction of PYTHIA [72] for the ratio in $p+p$ at $\sqrt{s} = 200$ GeV, and the red shaded area indicates the empirical m_T-scaling prescription Eq. (10) with fixed $a = 1.2$, power-law exponent $n = 10$–14, and an asymptotic $R^{\infty}_{\eta/\pi^0} = 0.5$ ratio.

probabilistic rules are given for the production of flavors ($u\bar{u} : d\bar{d} : s\bar{s} = 1 : 1 : 0.3$ in the default settings), spin (e.g., a 3:1 mixture between the lowest lying vector and pseudoscalar multiplets is used, suggested by spin counting arguments), and for the sharing of energy and momentum among the products. Regarding the latter, the probability that a hadron picks a fraction z of $E + p_z$ out of the available $E + p$ (p_z is the momentum of the formed hadron along the direction of the quark q) is given by the "Lund symmetric fragmentation function:"

$$f(z) \propto z^{-1}(1-z)^a \exp(-b\, {m_T}^2/z), \tag{8}$$

where a and b are free parameters adjusted to bring the fragmentation into accordance with measured LEP data, e.g., $a = 0.3$ and $b = 0.58$ GeV^{-2} are the current default values for PYTHIA 6.3 [76]. In addition, for the flavor-diagonal meson states $u\bar{u} : d\bar{d} : s\bar{s}$, PYTHIA also includes mixing into the physical mesons. This is done according to a parametrization, based on the mixing angles given in the *Review of Particle Properties* [57]. In particular, the default choices correspond to $\eta = 1/2(u\bar{u} + d\bar{d}) - 1/\sqrt{2}(s\bar{s})$ and $\eta' = 1/2(u\bar{u} + d\bar{d}) + 1/\sqrt{2}(s\bar{s})$. Thus, in the $\pi^0 - \eta - \eta'$ system, no account is taken of the difference in masses, an approximation that seems to lead to an overestimate of η' rates in e^+e^- annihilation [103]. PYTHIA includes therefore parameters to allow an additional "tunable" suppression of η and η' states.

The PYTHIA Monte Carlo simulations of π^0 and η p_T-differential cross sections were carried out with the default settings. In particular, no ad hoc suppression of η was selected. Any uncertainty related to the choice of any (flavor-independent) settings should in principle cancel in the ratio of both p_T spectra. As seen in Figs. 24–26, within the (relatively large in some cases) experimental uncertainties, good agreement between the $R_{\eta/\pi^0}(p_T)$ data and the model prediction is found for all the colliding systems and p_T ranges, despite being at very different center-of-mass energies. We have also run PYTHIA at $\sqrt{s} = 30$ GeV as a reference for lower

energy results, but the resulting η/π^0 curve, though slightly lower at high-p_T ($R_{\eta/\pi^0} \approx 0.44$), is still relatively close to the one obtained at $\sqrt{s} = 200$ GeV. This is an indication that the p_T dependence of the production mechanisms for both neutral mesons is very similar for all systems and center-of-mass energies and, correspondingly, the ratio of p_T-differential cross sections is basically independent of the characteristics of the initial collision process but dominated by the ratio of η and π^0 (vacuum) FF, which is relatively constant in this kinematic range (see discussion in Sec. IV E2).

b. m_T scaling. The red shaded curve shown in Figs. 24, 25, and 26 corresponds to an empirical m_T-scaling observation [77] that assumes that the hadron differential cross sections, plotted as a function of the transverse mass of the produced particle $m_T = \sqrt{m_h^2 + {p_T}^2}$, all have the same shape, $f(m_T)$, with an absolute normalization factor C_h that can vary but is found to be the same for many species:

$$E\frac{d^3\sigma_h}{d^3p} = C_h \cdot f(m_T). \tag{9}$$

Assuming isospin symmetry for pion production, we have combined the measured PHENIX charged $(\pi^+ + \pi^-)/2$ (measured in the range $p_T = 0.2$–2.6 GeV/c) [78] and neutral ($p_T = 1$–14 GeV/c) [17] pion differential m_T cross sections in $p+p$ collisions and fitted them with a modified power-law functional form[2] that reproduces the full spectra well in the range $m_T \approx 0.2$–14 GeV/c^2:

$$f(m_T) = (m_T + a)^{-n}, \quad \text{with } a = 1.2 \quad \text{and } n = 10. \tag{10}$$

If one assumes that m_T scaling holds for η, then its $m_T = \sqrt{m_\eta^2 + {p_T}^2}$ spectrum can also be represented by Eqs. (9) and (10) (with, in principle, a different C_h) and, therefore, the η/π^0 ratio as a function of p_T should follow:

$$R_{\eta/\pi^0}(p_T) = R^{\infty}_{\eta/\pi^0} \cdot \left[\frac{a + \sqrt{m_\eta^2 + {p_T}^2}}{a + \sqrt{m_{\pi^0}^2 + {p_T}^2}}\right]^n, \tag{11}$$

where $R^{\infty}_{\eta/\pi^0} = C_\eta/C_{\pi^0}$ is the asymptotic value of the ratio of η over π^0 for large p_T. Note that because the assumption of m_T scaling is that both m_T-differential cross sections have the same shape, the same parameters $a = 1.2$ and $n = 10$ are valid for both spectra as well as for the ratio [Eq. (11)]. In all figures, the plotted m_T-scaling curve with an asymptotic value of $R^{\infty}_{\eta/\pi^0} = 0.5$ is found to be in good agreement with both the data and the PYTHIA predictions. We note that the agreement between PYTHIA and m_T-scaling is not unexpected in as much as the Lund "fragmentation function," Eq. (8), depends explicitly on the m_T of the produced hadron. The upper red curve shown in all plots is that with the a and n parameters of Eq. (11) that reproduce the power-law shape of the meson spectra at $\sqrt{s} = 200$ GeV. At lower $\sqrt{s}$, the spectra get increasingly steeper and a and n change accordingly [a and n are correlated with $\langle m_T \rangle$ which itself is a logarithmically increasing function of $\sqrt{s}$, i.e., $\langle m_T \rangle = f(\sqrt{s})$]. For illustrative purposes, we have (arbitrarily) fixed the parameter a to the value $a = 1.2$ and refitted the π^0 spectra measured at different center-of-mass energies with n as a free exponent. With fixed a the corresponding values of the power-law exponent increase with decreasing $\sqrt{s}$ as $n \approx 10$, 11.5, 13.5, and 14.0 at $\sqrt{s} = 200$, 63, 27, and 13 GeV, respectively. The shaded red area indicates the range of expected m_T-scaling ratios for power-law exponents $n = 10.$–14. The differences are negligible at large p_T—where the η and π^0 masses are much smaller than their p_T and the ratio Eq. (11) $R_{\eta/\pi^0}(p_T) \approx R^{\infty}_{\eta/\pi^0}$ is independent of n but increases at lower p_T ($p_T \lesssim 3$ GeV/c). Furthermore, it is worth noting that in the low-p_T region below 1 GeV/c, the agreement between the data and the m_T-scaling curve is not always perfect for all data sets, even taking into account different power-law exponents. This is due to the fact that at very low $m_T \approx 0.0$–0.4 GeV/c^2, the pion yield rises due to contributions from multiple resonance decays and the formula [Eq. (10)] does not reproduce the spectral shape of the data anymore. Instead, an exponential behavior of the form $Ed^3\sigma/d^3p = B \cdot \exp(-b\, m_T)$ [99] extrapolates the spectra better in the soft regime all the way down to $m_T = 0$ GeV/c^2. However, for all practical purposes in this analysis focused on high-p_T production, we consider Eq. (10) [(and correspondingly Eq. (11)] to be a good enough approximation.

Last we want to mention that in the case of nucleus-nucleus collisions the existence of a strong collective radial flow ($\beta_{\rm coll} \approx 0.6$ at RHIC [100]), absent in $p+p$ collisions, changes the spectral shape of different hadrons produced at low transverse momenta ($p_T \lesssim 2$ GeV/c) and should result in a violation of the m_T-scaling behavior [101]. Because hydrodynamical flow results in a larger boost for the (heavier) η than for π^0, one expects a comparatively larger $R_{\eta/\pi^0}(p_T)$ ratio in Au+Au than in $p+p$ collisions below $p_T \approx 2$ GeV/c. Unfortunately, we cannot test this assertion with RHIC data since our lowest p_T value ($p_T \approx 2$ GeV/c) is just in the range where radial flow effects start to die out. The same holds true also for the recent proposal [102] to study the η/π^0 ratio as a tool to test different parton recombination scenarios in hadron production in nucleus-nucleus collisions. Lower-p_T η measurements, which are intrinsically more difficult due to the reduced PHENIX acceptance and the larger $\gamma\gamma$ combinatorial background, would be needed to better address the role of collective flow and/or parton recombination effects on the spectral shape and yields of light neutral mesons in Au+Au collisions at RHIC.

2. η/π^0 ratio in e^+e^- collisions at the Z pole ($\sqrt{s} = 91.2$ GeV)

In this last section we are interested in determining the η/π^0 ratio in an elementary colliding system such as e^+e^- and comparing it to the corresponding ratios obtained in hadronic and nuclear collisions. In e^+e^- the dominant high-momentum hadron production mechanism is $q, \bar{q}$ fragmentation because gluon production (and subsequent fragmentation) occurs with a probability that is suppressed by a factor α_S and therefore plays a comparatively less significant role than in the (highest energy) hadronic and nuclear collisions discussed in the

[2]Note that the a and n parameters of Eq. (10) are not independent but strongly correlated. They are actually related to the mean transverse mass of the spectrum via $\langle m_T \rangle = 2a/(n-3)$.

TABLE XI. Experimental measurements at LEP of η, π^0 spectra in e^+e^- collisions at $\sqrt{s} = 91.2$ GeV.

Collaboration/Year	Particle	Authors [Ref.]
ALEPH 92	η	Buskulic *et al.* [103]
ALEPH 96a	π^0	Barate *et al.* [104]
ALEPH 96b	π^0, η	Barate *et al.* [105]
ALEPH 99	π^0, η	Barate *et al.* [106]
ALEPH 01	η	Heister *et al.* [107]
DELPHI 95	π^0	Adam *et al.* [108]
L3 91	π^0	Adeva *et al.* [109]
L3 92	η	Adriani *et al.* [110]
L3 94a	π^0, η	Acciarri*et al.* [111]
OPAL 98	π^0, η	Ackerstaff *et al.* [112]
OPAL 00	π^0, η	Abbiendi *et al.* [113]

previous section. Some of the experimental interest in the study of η production in e^+e^- collisions was in fact triggered by theoretical expectations that the isoscalar mesons contained a significant $g\,g$ component, and thus that gluon jets should exhibit an anomalously large tendency to fragment into η and $\eta'(958)$ mesons [120–122]. However, this hypothesis was not confirmed by a detailed analysis of the ALEPH e^+e^- gluon fragmentation data [106]. Table XI lists all the existing measurements of inclusive π^0 and η production in e^+e^- collisions at LEP at energies around the Z pole. At lower energies, there are several results on inclusive π^0 production in e^+e^- but few η measurements exist ($\sqrt{s} = 29$ and 35 GeV at SLAC PEP [114,115] and SLC [116–119], respectively), and we could not determine the corresponding ratios.

Figures 27 and 28 show the combined inclusive η and π^0 invariant cross sections measured as a function of the scaled particle momentum $x_p = 2\,p_{\rm had}/\sqrt{s}$. Note that the overall η and π^0 spectra have been measured in x_p ranges which

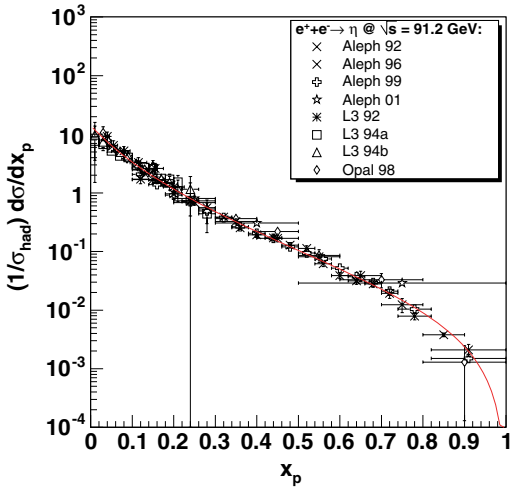

FIG. 27. (Color online) Differential inclusive η cross section as a function of the scaled momentum $x_p = 2\,p_{\rm had}/\sqrt{s}$ measured at the Z pole by the three LEP experiments listed in Table XI, fitted to Eq. (13) (solid curve).

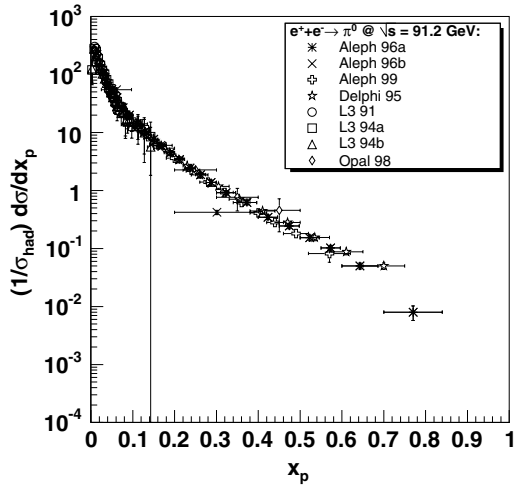

FIG. 28. Differential inclusive π^0 cross section as a function of the scaled momentum $x_p = 2\,p_{\rm had}/\sqrt{s}$ measured at the Z pole by the four LEP experiments listed in Table XI.

are not completely overlapping. There are more experimental measurements on inclusive η (π^0) production at large (small) $x_p \gtrsim 0.7 (x_p \lesssim 0.1)$. For this reason, to obtain the ratio of η over π^0 cross sections, we have parametrized the η cross section as

$$\frac{1}{\sigma_{\rm had}}\frac{d\sigma_\eta}{dx_p} = A \cdot (x_p + b)^n \cdot (1 - x_p)^m \qquad (12)$$

and taken the ratio of the individual π^0 data points over the resulting fit. We note that there is currently no η FF available in the standard FF sets at hand in the literature (BKK [123], KKP [124], Kretzer [125], BFGW [126]). Namely, the LEP data compiled in Fig. 27 have not been fitted and coded so far into any usable format that can be handled within a QCD collinear factorization approach. We are aware of only

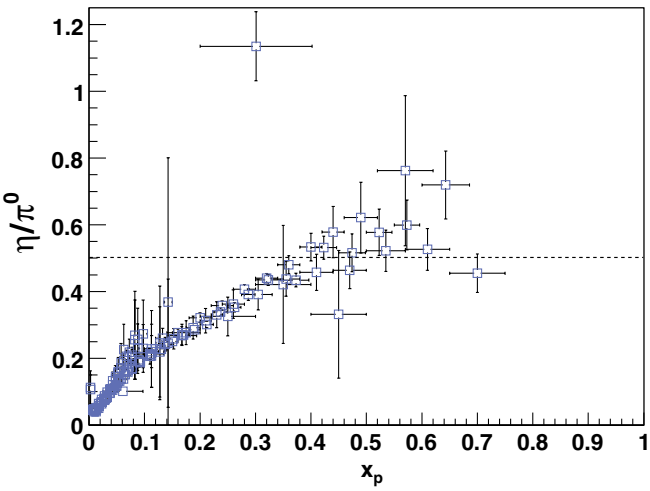

FIG. 29. (Color online) Ratio η/π^0 versus scaled momentum $x_p = 2\,p_{\rm had}/\sqrt{s}$ measured in e^+e^- collisions at LEP energies (Table XI), obtained from the π^0 results of Fig. 28 and the η fit, Eq. (13). The dashed line is the asymptotic $R_{\eta/\pi^0} = 0.5$ measured in hadronic and nuclear collisions.

TABLE XII. Invariant production cross section of η mesons in $p+p$ at $\sqrt{s} = 200$ GeV.

p_T (GeV/c)	$E\,d^3\sigma/d^3p$ (mb/GeV$^{-2}c^3$)	Tot. err.	Stat. err.	Sys. err.	ErrorA	Error B	Error C
			$\eta \to \gamma\gamma$				
2.75	1.30×10^{-3}	4.20×10^{-4}	2.25×10^{-4}	7.91×10^{-6}	0	3.34×10^{-4}	1.20×10^{-4}
3.25	3.78×10^{-4}	6.81×10^{-5}	8.09×10^{-6}	1.37×10^{-6}	0	5.79×10^{-5}	3.48×10^{-5}
3.75	1.37×10^{-4}	2.15×10^{-5}	3.53×10^{-6}	4.03×10^{-7}	0	1.70×10^{-5}	1.26×10^{-5}
4.25	5.49×10^{-5}	8.20×10^{-6}	1.81×10^{-6}	1.47×10^{-7}	0	6.20×10^{-6}	5.05×10^{-6}
4.75	2.22×10^{-5}	3.34×10^{-6}	1.03×10^{-6}	5.76×10^{-8}	0	2.43×10^{-6}	2.04×10^{-6}
5.25	1.08×10^{-5}	1.70×10^{-6}	6.82×10^{-7}	2.83×10^{-8}	0	1.20×10^{-6}	9.90×10^{-7}
5.75	5.66×10^{-6}	9.36×10^{-7}	4.39×10^{-7}	1.52×10^{-8}	0	6.42×10^{-7}	5.21×10^{-7}
6.5	2.02×10^{-6}	3.47×10^{-7}	1.75×10^{-7}	5.58×10^{-9}	0	2.36×10^{-7}	1.86×10^{-7}
7.5	6.99×10^{-7}	1.40×10^{-7}	9.14×10^{-8}	2.00×10^{-9}	0	8.45×10^{-8}	6.43×10^{-8}
8.5	1.81×10^{-7}	4.92×10^{-8}	4.04×10^{-8}	5.35×10^{-10}	0	2.26×10^{-8}	1.67×10^{-8}
9.5	1.02×10^{-7}	3.22×10^{-8}	2.80×10^{-8}	3.08×10^{-10}	0	1.30×10^{-8}	9.34×10^{-9}
11	2.21×10^{-8}	9.24×10^{-9}	8.52×10^{-9}	1.35×10^{-10}	0	2.94×10^{-9}	2.03×10^{-9}
			$\eta \to \pi^0\pi^+\pi^-$				
3.0	7.5×10^{-4}	2.4×10^{-4}	1.3×10^{-4}	2.1×10^{-4}	1.1×10^{-4}	1.6×10^{-4}	8.5×10^{-5}
4.0	8.1×10^{-5}	2.5×10^{-5}	1.4×10^{-5}	2.1×10^{-5}	1.3×10^{-5}	1.4×10^{-5}	9.1×10^{-6}
5.0	2.0×10^{-5}	6.6×10^{-6}	3.3×10^{-6}	5.8×10^{-6}	4.5×10^{-6}	2.9×10^{-6}	2.3×10^{-6}
6.0	5.8×10^{-6}	1.7×10^{-6}	1.1×10^{-6}	1.4×10^{-6}	9.5×10^{-7}	7.2×10^{-7}	6.5×10^{-7}
7.0	1.0×10^{-6}	5.0×10^{-7}	3.9×10^{-7}	3.2×10^{-7}	2.6×10^{-7}	1.3×10^{-7}	1.2×10^{-7}
8.0	4.5×10^{-7}	2.7×10^{-7}	2.1×10^{-7}	1.6×10^{-7}	1.5×10^{-7}	5.6×10^{-8}	5.1×10^{-8}

two works (Rolli *et al.* at NLO [127] and Indumathi and collaborators at LO [128]) that have tried to parametrize the η FF from these data. An updated version of the η FF would be useful as input to a NLO pQCD cross-section calculation for comparison to the results presented here and especially in the light of upcoming high-p_T η asymmetry results using polarized beams of relevance for the proton spin program at RHIC [44]. Fitting all the available η data with Eq. (12), we obtain the following empirical parametrization:

$$\frac{1}{\sigma_{\text{had}}}\frac{d\sigma_\eta}{dx_p} = 0.0975 \cdot (x_p + 0.186)^{-2.953} \cdot (1 - x_p)^{1.507}, \qquad \chi^2/\text{ndf} = 0.37. \tag{13}$$

TABLE XIII. Invariant production cross section of η mesons in d+Au at $\sqrt{s_{NN}} = 200$ GeV.

p_T (GeV/c)	$E\,d^3\sigma/d^3p$ (mb/GeV$^{-2}c^3$)	Tot. err.	Stat. err.	Sys. err.	Error A	Error B	Error C
			$\eta \to \gamma\gamma$				
2.25	2.06	7.49×10^{-1}	1.30×10^{-1}	3.37×10^{-4}	0	7.30×10^{-1}	1.08×10^{-1}
2.75	6.25×10^{-1}	1.09×10^{-1}	4.06×10^{-2}	4.41×10^{-5}	0	9.55×10^{-2}	3.28×10^{-2}
3.25	1.58×10^{-1}	2.40×10^{-2}	1.48×10^{-2}	7.84×10^{-6}	0	1.70×10^{-2}	8.27×10^{-3}
3.75	6.72×10^{-2}	8.21×10^{-3}	1.86×10^{-3}	3.31×10^{-6}	0	7.18×10^{-3}	3.53×10^{-3}
4.25	2.57×10^{-2}	3.18×10^{-3}	7.56×10^{-4}	1.28×10^{-6}	0	2.78×10^{-3}	1.35×10^{-3}
4.75	1.06×10^{-2}	1.34×10^{-3}	3.64×10^{-4}	5.39×10^{-7}	0	1.17×10^{-3}	5.55×10^{-4}
5.25	4.38×10^{-3}	5.65×10^{-4}	1.96×10^{-4}	2.20×10^{-7}	0	4.77×10^{-4}	2.30×10^{-4}
5.75	2.30×10^{-3}	3.08×10^{-4}	1.22×10^{-4}	1.18×10^{-7}	0	2.56×10^{-4}	1.21×10^{-4}
6.5	9.20×10^{-4}	1.27×10^{-4}	5.11×10^{-5}	4.86×10^{-8}	0	1.05×10^{-4}	4.83×10^{-5}
7.5	2.47×10^{-4}	4.39×10^{-5}	3.00×10^{-5}	1.35×10^{-8}	0	2.93×10^{-5}	1.30×10^{-5}
8.5	9.17×10^{-5}	1.89×10^{-5}	1.44×10^{-5}	5.18×10^{-9}	0	1.12×10^{-5}	4.82×10^{-6}
9.5	4.56×10^{-5}	9.14×10^{-6}	6.69×10^{-6}	2.65×10^{-9}	0	5.75×10^{-6}	2.40×10^{-6}
11	1.31×10^{-5}	2.88×10^{-6}	2.21×10^{-6}	7.92×10^{-10}	0	1.72×10^{-6}	6.88×10^{-7}
			$\eta \to \pi^0\pi^+\pi^-$				
5.0	1.1×10^{-2}	7.6×10^{-3}	5.7×10^{-3}	5.1×10^{-3}	3.7×10^{-3}	3.2×10^{-3}	9.9×10^{-4}
6.0	2.7×10^{-3}	1.6×10^{-3}	1.2×10^{-3}	1.0×10^{-3}	6.9×10^{-4}	7.3×10^{-4}	2.4×10^{-4}
7.0	5.8×10^{-4}	4.4×10^{-4}	3.9×10^{-4}	1.9×10^{-4}	1.3×10^{-4}	1.3×10^{-4}	5.1×10^{-5}
8.0	2.4×10^{-4}	1.4×10^{-4}	1.1×10^{-4}	8.4×10^{-5}	6.1×10^{-5}	5.4×10^{-5}	2.1×10^{-5}

TABLE XIV. Invariant yields, $(1/2\pi\, p_T)(d^2N_{\rm cent}/d\,p_T dy)$, measured in d+Au for different centrality classes from most central (0–20%) to most peripheral (60–88%).

p_T (GeV/c)	Inv. yield	Tot. err.	Stat. err.	Sys. err.	Error A	Error B	Error C
			0–20%				
2.25	1.59×10^{-3}	5.96×10^{-4}	1.85×10^{-4}	5.67×10^{-4}	0	5.67×10^{-4}	0
2.75	5.46×10^{-4}	1.02×10^{-4}	5.65×10^{-5}	8.49×10^{-5}	0	8.49×10^{-5}	0
3.25	1.27×10^{-4}	2.49×10^{-5}	2.05×10^{-5}	1.42×10^{-5}	0	1.42×10^{-5}	0
3.75	5.84×10^{-5}	6.89×10^{-6}	2.43×10^{-6}	6.45×10^{-6}	0	6.45×10^{-6}	0
4.25	2.22×10^{-5}	2.66×10^{-6}	9.62×10^{-7}	2.48×10^{-6}	0	2.48×10^{-6}	0
4.75	9.26×10^{-6}	1.15×10^{-6}	4.61×10^{-7}	1.06×10^{-6}	0	1.06×10^{-6}	0
5.25	3.85×10^{-6}	4.92×10^{-7}	2.36×10^{-7}	4.32×10^{-7}	0	4.32×10^{-7}	0
5.75	1.97×10^{-6}	2.70×10^{-7}	1.47×10^{-7}	2.26×10^{-7}	0	2.26×10^{-7}	0
6.5	7.29×10^{-7}	1.06×10^{-7}	6.15×10^{-8}	8.60×10^{-8}	0	8.60×10^{-8}	0
7.5	2.26×10^{-7}	4.57×10^{-8}	3.64×10^{-8}	2.76×10^{-8}	0	2.76×10^{-8}	0
8.5	5.29×10^{-8}	1.36×10^{-8}	1.19×10^{-8}	6.65×10^{-9}	0	6.65×10^{-9}	0
9.5	3.31×10^{-8}	8.26×10^{-9}	7.06×10^{-9}	4.27×10^{-9}	0	4.27×10^{-9}	0
11	1.05×10^{-8}	2.84×10^{-9}	2.47×10^{-9}	1.41×10^{-9}	0	1.41×10^{-9}	0
			20–40%				
2.25	1.18×10^{-3}	4.38×10^{-4}	1.37×10^{-4}	4.16×10^{-4}	0	4.16×10^{-4}	0
2.75	4.02×10^{-4}	7.52×10^{-5}	4.36×10^{-5}	6.13×10^{-5}	0	6.13×10^{-5}	0
3.25	1.02×10^{-4}	1.93×10^{-5}	1.59×10^{-5}	1.09×10^{-5}	0	1.09×10^{-5}	0
3.75	3.92×10^{-5}	4.60×10^{-6}	1.90×10^{-6}	4.18×10^{-6}	0	4.18×10^{-6}	0
4.25	1.47×10^{-5}	1.77×10^{-6}	7.97×10^{-7}	1.59×10^{-6}	0	1.59×10^{-6}	0
4.75	5.89×10^{-6}	7.53×10^{-7}	3.79×10^{-7}	6.50×10^{-7}	0	6.50×10^{-7}	0
5.25	2.99×10^{-6}	4.01×10^{-7}	2.35×10^{-7}	3.25×10^{-7}	0	3.25×10^{-7}	0
5.75	1.45×10^{-6}	2.06×10^{-7}	1.28×10^{-7}	1.61×10^{-7}	0	1.61×10^{-7}	0
6.5	5.44×10^{-7}	8.24×10^{-8}	5.41×10^{-8}	6.22×10^{-8}	0	6.22×10^{-8}	0
7.5	1.68×10^{-7}	3.69×10^{-8}	3.11×10^{-8}	1.99×10^{-8}	0	1.99×10^{-8}	0
8.5	5.91×10^{-8}	1.29×10^{-8}	1.07×10^{-8}	7.23×10^{-9}	0	7.23×10^{-9}	0
9.5	1.92×10^{-8}	7.74×10^{-9}	7.35×10^{-9}	2.42×10^{-9}	0	2.42×10^{-9}	0
11	1.19×10^{-8}	2.90×10^{-9}	2.45×10^{-9}	1.55×10^{-9}	0	1.55×10^{-9}	0
			40–60%				
2.25	9.14×10^{-4}	3.40×10^{-4}	1.03×10^{-4}	3.24×10^{-4}	0	3.24×10^{-4}	0
2.75	1.85×10^{-4}	4.31×10^{-5}	3.25×10^{-5}	2.83×10^{-5}	0	2.83×10^{-5}	0
3.25	7.17×10^{-5}	1.47×10^{-5}	1.25×10^{-5}	7.73×10^{-6}	0	7.73×10^{-6}	0
3.75	2.46×10^{-5}	3.01×10^{-6}	1.47×10^{-6}	2.62×10^{-6}	0	2.62×10^{-6}	0
4.25	9.73×10^{-6}	1.22×10^{-6}	6.23×10^{-7}	1.05×10^{-6}	0	1.05×10^{-6}	0
4.75	4.19×10^{-6}	5.67×10^{-7}	3.27×10^{-7}	4.63×10^{-7}	0	4.63×10^{-7}	0
5.25	1.71×10^{-6}	2.69×10^{-7}	1.95×10^{-7}	1.85×10^{-7}	0	1.85×10^{-7}	0
5.75	9.73×10^{-7}	1.71×10^{-7}	1.33×10^{-7}	1.08×10^{-7}	0	1.08×10^{-7}	0
6.5	3.84×10^{-7}	6.14×10^{-8}	4.29×10^{-8}	4.39×10^{-8}	0	4.39×10^{-8}	0
7.5	1.07×10^{-7}	3.14×10^{-8}	2.87×10^{-8}	1.27×10^{-8}	0	1.27×10^{-8}	0
8.5	3.69×10^{-8}	1.15×10^{-8}	1.06×10^{-8}	4.52×10^{-9}	0	4.52×10^{-9}	0
9.5	1.41×10^{-8}	6.31×10^{-9}	6.06×10^{-9}	1.77×10^{-9}	0	1.77×10^{-9}	0
11	2.56×10^{-9}	2.11×10^{-9}	2.09×10^{-9}	3.35×10^{-10}	0	3.35×10^{-10}	0
			60–88%				
2.25	4.07×10^{-4}	1.54×10^{-4}	5.17×10^{-5}	1.45×10^{-4}	0	1.45×10^{-4}	0
2.75	1.27×10^{-4}	2.64×10^{-5}	1.75×10^{-5}	1.97×10^{-5}	0	1.97×10^{-5}	0
3.25	3.52×10^{-5}	7.72×10^{-6}	6.66×10^{-6}	3.90×10^{-6}	0	3.90×10^{-6}	0
3.75	1.11×10^{-5}	1.45×10^{-6}	7.84×10^{-7}	1.22×10^{-6}	0	1.22×10^{-6}	0
4.25	4.55×10^{-6}	6.09×10^{-7}	3.40×10^{-7}	5.06×10^{-7}	0	5.06×10^{-7}	0
4.75	1.88×10^{-6}	2.71×10^{-7}	1.68×10^{-7}	2.13×10^{-7}	0	2.13×10^{-7}	0
5.25	6.34×10^{-7}	1.21×10^{-7}	9.76×10^{-8}	7.10×10^{-8}	0	7.10×10^{-8}	0
5.75	4.65×10^{-7}	8.14×10^{-8}	6.17×10^{-8}	5.31×10^{-8}	0	5.31×10^{-8}	0
6.5	2.27×10^{-7}	4.27×10^{-8}	3.34×10^{-8}	2.66×10^{-8}	0	2.66×10^{-8}	0
7.5	4.83×10^{-8}	1.17×10^{-8}	1.01×10^{-8}	5.87×10^{-9}	0	5.87×10^{-9}	0
8.5	1.18×10^{-8}	6.61×10^{-9}	6.44×10^{-9}	1.48×10^{-9}	0	1.48×10^{-9}	0
9.5	6.33×10^{-9}	3.76×10^{-9}	3.67×10^{-9}	8.15×10^{-10}	0	8.15×10^{-10}	0

TABLE XV. Invariant yields measured, $(1/2\pi\, p_T)(d^2N_{\rm cent}/d\,p_T dy)$, in Au+Au for different centrality classes, including minimum bias (0–92%) and three centrality classes (0–20, 20–60, 60–92%).

p_T (GeV/c)	Inv. yield	Tot. err.	Sys. err.	Stat. err. + error A	Error B	Error C
			0–92% (MB)			
2.25	1.26×10^{-2}	3.66×10^{-3}	1.84×10^{-3}	3.16×10^{-3}	1.48×10^{-3}	0
2.75	3.90×10^{-3}	1.12×10^{-3}	5.78×10^{-4}	9.61×10^{-4}	4.66×10^{-4}	0
3.25	8.79×10^{-4}	1.70×10^{-4}	1.32×10^{-4}	1.08×10^{-4}	1.07×10^{-4}	0
3.75	2.33×10^{-4}	5.13×10^{-5}	3.53×10^{-5}	3.72×10^{-5}	2.88×10^{-5}	0
4.50	6.44×10^{-5}	1.60×10^{-5}	9.97×10^{-6}	1.25×10^{-5}	8.22×10^{-6}	0
5.50	1.14×10^{-5}	2.57×10^{-6}	1.82×10^{-6}	1.81×10^{-6}	1.52×10^{-6}	0
6.50	2.80×10^{-6}	1.05×10^{-6}	4.59×10^{-7}	9.48×10^{-7}	3.87×10^{-7}	0
7.50	9.60×10^{-7}	2.63×10^{-7}	1.62×10^{-7}	2.07×10^{-7}	1.38×10^{-7}	0
8.50	4.09×10^{-7}	1.84×10^{-7}	7.07×10^{-8}	1.70×10^{-7}	6.09×10^{-8}	0
9.50	1.51×10^{-7}	8.25×10^{-8}	2.67×10^{-8}	7.81×10^{-8}	2.32×10^{-8}	0
			0–20%			
2.25	3.95×10^{-2}	1.24×10^{-2}	5.80×10^{-3}	1.09×10^{-2}	4.65×10^{-3}	0
2.75	1.29×10^{-2}	3.86×10^{-3}	1.91×10^{-3}	3.36×10^{-3}	1.54×10^{-3}	0
3.25	2.23×10^{-3}	5.99×10^{-4}	3.34×10^{-4}	4.97×10^{-4}	2.71×10^{-4}	0
3.75	4.53×10^{-4}	2.07×10^{-4}	6.88×10^{-5}	1.95×10^{-4}	5.61×10^{-5}	0
4.50	1.49×10^{-4}	4.55×10^{-5}	2.30×10^{-5}	3.93×10^{-5}	1.90×10^{-5}	0
5.50	2.74×10^{-5}	8.33×10^{-6}	4.37×10^{-6}	7.09×10^{-6}	3.65×10^{-6}	0
6.50	5.99×10^{-6}	2.73×10^{-6}	9.83×10^{-7}	2.55×10^{-6}	8.30×10^{-7}	0
7.50	2.79×10^{-6}	6.99×10^{-7}	4.71×10^{-7}	5.17×10^{-7}	4.02×10^{-7}	0
8.50	8.42×10^{-7}	4.02×10^{-7}	1.46×10^{-7}	3.75×10^{-7}	1.25×10^{-7}	0
9.50	4.18×10^{-7}	2.18×10^{-7}	7.40×10^{-8}	2.05×10^{-7}	6.43×10^{-8}	0
			20–60%			
2.25	1.21×10^{-2}	3.51×10^{-3}	1.78×10^{-3}	3.03×10^{-3}	1.42×10^{-3}	0
2.75	2.88×10^{-3}	8.52×10^{-4}	4.26×10^{-4}	7.38×10^{-4}	3.43×10^{-4}	0
3.25	8.58×10^{-4}	1.66×10^{-4}	1.29×10^{-4}	1.06×10^{-4}	1.04×10^{-4}	0
3.75	2.54×10^{-4}	5.40×10^{-5}	3.85×10^{-5}	3.78×10^{-5}	3.14×10^{-5}	0
4.50	7.05×10^{-5}	1.74×10^{-5}	1.09×10^{-5}	1.36×10^{-5}	8.99×10^{-6}	0
5.50	1.57×10^{-5}	3.36×10^{-6}	2.51×10^{-6}	2.24×10^{-6}	2.09×10^{-6}	0
6.50	3.30×10^{-6}	1.28×10^{-6}	5.42×10^{-7}	1.16×10^{-6}	4.58×10^{-7}	0
7.50	1.06×10^{-6}	2.65×10^{-7}	1.79×10^{-7}	1.96×10^{-7}	1.53×10^{-7}	0
8.50	3.46×10^{-7}	1.60×10^{-7}	5.99×10^{-8}	1.48×10^{-7}	5.16×10^{-8}	0
9.50	1.54×10^{-7}	7.97×10^{-8}	2.72×10^{-8}	7.49×10^{-8}	2.36×10^{-8}	0
			60–92%			
2.25	1.06×10^{-3}	3.27×10^{-4}	2.41×10^{-4}	2.21×10^{-4}	2.22×10^{-4}	0
2.75	3.34×10^{-4}	1.02×10^{-4}	7.61×10^{-5}	6.83×10^{-5}	7.03×10^{-5}	0
3.25	1.11×10^{-4}	2.34×10^{-5}	1.66×10^{-5}	1.65×10^{-5}	1.34×10^{-5}	0
3.75	4.04×10^{-5}	9.05×10^{-6}	6.13×10^{-6}	6.66×10^{-6}	5.00×10^{-6}	0
4.50	1.16×10^{-5}	3.11×10^{-6}	1.80×10^{-6}	2.54×10^{-6}	1.48×10^{-6}	0
5.50	1.67×10^{-6}	1.07×10^{-6}	2.65×10^{-7}	1.04×10^{-6}	2.22×10^{-7}	0

Using the fit [Eq. (13)] and the π^0 data plotted in Fig. 28 we have obtained the $R_{\eta/\pi^0}(x_p)$ ratio shown in Fig. 29. As seen for the corresponding η/π^0 ratios in hadronic and nuclear collisions, at low values of (scaled) momentum the π^0 production overwhelms that of η (a significant fraction of low-energy pions issues from decay contributions of heavier hadrons), but the ratio increases with x_p. From $x_p \approx 0.35$–0.7, the ratio is consistent with the asymptotic ratio of 0.5 found in hadron and nuclear collisions (dashed curve). This x_p range corresponds to the values of fractional momenta $\langle z \rangle \gtrsim 0.3$–$0.7$ typically carried by the leading high-p_T hadrons produced in high-energy h+p, h+A, and A+A collisions [129,130]. New results on inclusive η and π^0 production above $x_p = 0.6$ in e^+e^- collisions at the B-factories (BELLE and BaBar) would be useful to determine whether the value of the ratio indeed saturates at $R_{\eta/\pi^0} = 0.5$ or keeps increasing with x_p as suggested by Fig. 29.

F. Summary of experimental results

The studies presented here on high-p_T π^0 and η production in the three colliding systems (p+p, d+Au, Au+Au) provide interesting insights on initial- and final-state QCD effects in

TABLE XVI. Nuclear modification factor R_{dA} for η in d+Au collisions for different centrality classes, including minimum bias (0–88%) and four centralities (0–20, 20–40, 40–60, 60–88%).

p_T (GeV/c)	R_{dA}	Tot. err.	Stat. err. + error A	Error B	Error C
		0–88% (MB)			
2.75	1.22	0.435	0.224	0.340	0.134
3.25	1.06	0.233	0.102	0.162	0.117
3.75	1.24	0.220	0.047	0.148	0.137
4.25	1.19	0.201	0.052	0.125	0.131
4.75	1.21	0.205	0.070	0.119	0.133
5.25	1.03	0.183	0.080	0.102	0.114
5.75	1.03	0.191	0.097	0.102	0.114
6.5	1.16	0.220	0.119	0.115	0.128
7.5	0.896	0.215	0.160	0.089	0.099
8.5	1.28	0.406	0.350	0.128	0.142
9.5	1.14	0.400	0.356	0.114	0.126
11	1.51	0.680	0.635	0.151	0.166
		0–20%			
2.75	1.15	0.421	0.231	0.322	0.130
3.25	0.922	0.236	0.150	0.141	0.104
3.75	1.17	0.210	0.057	0.140	0.132
4.25	1.11	0.191	0.060	0.116	0.126
4.75	1.15	0.198	0.078	0.113	0.130
5.25	0.982	0.179	0.087	0.097	0.111
5.75	0.956	0.184	0.103	0.094	0.108
6.5	0.992	0.199	0.120	0.098	0.112
7.5	0.887	0.232	0.184	0.088	0.101
8.5	0.802	0.285	0.254	0.080	0.091
9.5	0.894	0.343	0.312	0.089	0.101
11	1.30	0.626	0.590	0.131	0.148
		20–40%			
2.75	1.22	0.450	0.249	0.342	0.139
3.25	1.07	0.270	0.169	0.163	0.121
3.75	1.14	0.206	0.062	0.136	0.129
4.25	1.06	0.186	0.067	0.111	0.120
4.75	1.05	0.188	0.084	0.104	0.120
5.25	1.10	0.208	0.112	0.109	0.125
5.75	1.02	0.201	0.120	0.100	0.116
6.5	1.07	0.222	0.141	0.106	0.121
7.5	0.953	0.264	0.216	0.095	0.108
8.5	1.30	0.425	0.371	0.129	0.147
9.5	0.750	0.374	0.354	0.075	0.085
11	2.13	0.995	0.934	0.214	0.242
		40–60%			
2.75	0.86	0.338	0.212	0.241	0.102
3.25	1.15	0.305	0.202	0.176	0.136
3.75	1.09	0.201	0.071	0.130	0.128
4.25	1.08	0.192	0.078	0.113	0.127
4.75	1.14	0.210	0.104	0.113	0.135
5.25	0.962	0.198	0.126	0.095	0.114
5.75	1.04	0.234	0.164	0.103	0.123
6.5	1.15	0.246	0.163	0.114	0.136
7.5	0.929	0.314	0.277	0.092	0.110
8.5	1.24	0.490	0.449	0.123	0.146
9.5	0.842	0.451	0.430	0.084	0.099
11	0.704	0.645	0.636	0.071	0.083

TABLE XVI. *(Continued.)*

p_T (GeV/c)	R_{dA}	Tot. err.	Stat. err. + error A	Error B	Error C
			60–88%		
2.75	1.36	0.515	0.301	0.381	0.165
3.25	1.30	0.358	0.248	0.200	0.158
3.75	1.13	0.213	0.085	0.135	0.137
4.25	1.16	0.212	0.095	0.122	0.141
4.75	1.18	0.223	0.119	0.117	0.143
5.25	0.826	0.190	0.138	0.081	0.010
5.75	1.15	0.255	0.177	0.114	0.140
6.5	1.57	0.368	0.269	0.156	0.191
7.5	0.969	0.285	0.239	0.096	0.117
8.5	0.913	0.558	0.538	0.091	0.111
9.5	0.874	0.578	0.561	0.087	0.106

cold nuclear matter (d+Au) and on the properties of the hot and dense medium produced in central Au+Au collisions. The absence of any strong deviation from the pointlike scaling expectations for the p_T-differential π^0 and η yields measured in d+Au relative to $p+p$ (Fig. 18) indicates that the amount of nuclear shadowing and initial-state p_T broadening is a small effect (at the 10% level) at midrapidity at RHIC energies. This is in contrast with results at lower energies that showed a larger Cronin enhancement for high-p_T mesons than observed here. One reason for the difference is likely due to the fact that hadron spectra at lower $\sqrt{s_{NN}}$ have steeper slopes and thus initial-state k_T "kicks" produce a relatively larger net effect than on the harder spectra at RHIC energies. The unsuppressed d+Au yields combined with the observation of strongly depleted yields of η and π^0 in central Au+Au compared to binary-scaled $p+p$ collisions (Fig. 19) indicate that the suppression is a final-state effect in the hot and dense matter produced in the central Au+Au reactions. The consistent values of the η/π^0 ratios measured at high p_T in nuclear (Figs. 25 and 26) as well as in more elementary $p+p$ (Fig. 24) and e^+e^- (Fig. 29) collisions clearly supports the idea that the suppression occurs at the parton level before the fragmentation of the parent quarks and gluons into a given leading meson. In particular, the overall agreement of the η/π^0 ratio measured in Au+Au and e^+e^- collisions suggests that although the fast parent partons lose energy while traversing the system produced in central Au+Au collisions, their relative probability to fragment into a given meson, given by universal fragmentation functions, is preserved as expected for final hadron formation in the vacuum.

V. SUMMARY

In summary, the transverse momentum spectra of η mesons in the range $p_T = 2$–12 GeV/c have been measured at midrapidity by the PHENIX experiment at RHIC in $p+p$, d+Au, and Au+Au collisions at $\sqrt{s_{NN}} = 200$ GeV. The η mesons are reconstructed through their $\eta \to \gamma\gamma$ channel in the three colliding systems, as well as through the $\eta \to \pi^0\pi^+\pi^-$ decay mode in $p+p$ and d+Au collisions. These data provide additional characterization of high-p_T hadroproduction in hadronic and nuclear collisions at RHIC energies. The d+Au yields are largely consistent with the $p+p$ differential cross sections scaled by the number of incoherent nucleon-nucleon collisions ($R_{dA} \approx 1$). No p_T or centrality dependence is observed in the nuclear modification factor within uncertainties. Such an observation indicates a null or very weak p_T

TABLE XVII. Nuclear modification factor $R_{AA}(p_T)$ for η in Au+Au collisions for different centrality classes from most central (0–20%) to most peripheral (60–92%). Note that there is an additional 9.7% normalization uncertainty (Run-3 $p+p$ BBC error, gray box in Fig. 19) not quoted.

p_T (GeV/c)	R_{AA}	Tot. err.	Error C
		0–20%	
2.75	0.532	0.227 (42.6%)	0.036 (6.8%)
3.25	0.318	0.096 (30.2%)	0.022 (6.8%)
3.75	0.178	0.084 (46.9%)	0.012 (6.8%)
4.50	0.234	0.074 (31.7%)	0.016 (6.8%)
5.50	0.199	0.063 (31.6%)	0.014 (6.8%)
6.50	0.160	0.075 (46.9%)	0.011 (6.8%)
7.50	0.215	0.062 (28.9%)	0.015 (6.8%)
8.50	0.250	0.133 (53.0%)	0.017 (6.8%)
9.50	0.222	0.131 (59.3%)	0.015 (6.8%)
		20–60%	
2.75	0.479	0.202 (42.3%)	0.037 (7.8%)
3.25	0.492	0.117 (23.8%)	0.038 (7.8%)
3.75	0.401	0.095 (23.6%)	0.031 (7.8%)
4.50	0.446	0.116 (26.0%)	0.035 (7.8%)
5.50	0.460	0.106 (23.1%)	0.036 (7.8%)
6.50	0.355	0.143 (40.3%)	0.028 (7.8%)
7.50	0.329	0.095 (28.9%)	0.026 (7.8%)
8.50	0.414	0.214 (51.6%)	0.032 (7.8%)
9.50	0.328	0.193 (58.9%)	0.026 (7.8%)
		60–92%	
2.75	0.733	0.315 (43.0%)	0.209 (28.6%)
3.25	0.837	0.211 (25.3%)	0.239 (28.6%)
3.75	0.841	0.208 (24.7%)	0.240 (28.6%)
4.50	0.967	0.271 (28.0%)	0.276 (28.6%)
5.50	0.641	0.415 (64.8%)	0.183 (28.6%)

TABLE XVIII. Ratio of η and π^0 for $p+p$ collisions at $\sqrt{s} =$ 200 GeV.

p_T (GeV/c)	η/π^0	Tot. err.	Stat. err.	Error A	Error B	Error C
2.75	0.440	0.131	0.076	0	0.107	0
3.25	0.421	0.041	0.009	0	0.040	0
3.75	0.446	0.032	0.012	0	0.030	0
4.25	0.473	0.035	0.016	0	0.031	0
4.75	0.468	0.036	0.022	0	0.029	0
5.25	0.510	0.045	0.032	0	0.031	0
5.75	0.561	0.055	0.044	0	0.034	0
6.5	0.540	0.057	0.047	0	0.033	0
7.5	0.596	0.086	0.078	0	0.037	0
8.5	0.426	0.099	0.095	0	0.027	0
9.5	0.588	0.166	0.162	0	0.039	0
11	0.419	0.164	0.162	0	0.029	0

broadening and, in general, a very modest influence of cold nuclear matter effects, such as shadowing of parton distribution functions, Cronin broadening, and/or hadronization by parton recombination, on high-p_T meson production at midrapidity at top RHIC energies. In contrast, the invariant yields measured in Au+Au are increasingly depleted with centrality compared to expectations from binary-scaled $p+p$ collisions, up to a maximum factor of $\sim$5 suppression in central collisions. The magnitude, p_T and centrality dependence of the Au+Au suppression is the same for η mesons and neutral pions. The measured η/π^0 ratio in $p+p$, d+Au, and Au+Au is nearly flat over $p_T = 2$–12 GeV/c and is independent of the reaction centrality. A fit to a constant yields $R_{\eta/\pi^0}(p_T) = 0.4$–0.5, in agreement with the experimental world values at high p_T collected here for hadron-hadron, hadron-nucleus, and nucleus-nucleus collisions in a wide range of center-of-mass energies ($\sqrt{s} \approx 3$–1800 GeV), as well as at high x_p ($x_p \gtrsim 0.35$) in electron-positron annihilations measured at $\sqrt{s} = 91.2$ GeV at LEP. These results indicate that any initial- and/or final-state nuclear effects influence the production of light neutral mesons at large p_T in the same way. The similar suppression pattern of η and π^0 mesons is consistent with the expectations of final-state parton energy loss in the dense medium formed in Au+Au reactions. The approximately constant $\eta/\pi^0 = 0.40 \pm 0.04$ ratio measured in central Au+Au collisions indicates that the attenuated parent partons fragment into leading mesons (η, π^0) in the vacuum according to the same probabilities that govern high-p_T hadron production in more elementary (e^+e^-, $p+p$) collisions.

ACKNOWLEDGMENTS

We thank the staff of the Collider-Accelerator and Physics Departments at Brookhaven National Laboratory and the staff of the other PHENIX participating institutions for their vital contributions. We acknowledge support from the Department of Energy, Office of Science, Office of Nuclear Physics, the National Science Foundation, Abilene Christian University Research Council, Research Foundation of SUNY, and Dean

TABLE XIX. Ratio of η and π^0 for d+Au collisions for different centrality classes, including minimum bias (0–88%), most central (0–20%), and most peripheral (60–88%).

p_T (GeV/c)	η/π^0	Tot. err.	Stat. err. + error A	Error B	Error C
		0–88% (MB)			
2.25	0.420	0.038	0.028	0.025	0
2.75	0.472	0.044	0.033	0.028	0
3.25	0.383	0.045	0.039	0.023	0
3.75	0.472	0.034	0.018	0.028	0
4.25	0.478	0.033	0.017	0.029	0
4.75	0.483	0.035	0.020	0.029	0
5.25	0.465	0.037	0.025	0.028	0
5.75	0.510	0.043	0.030	0.031	0
6.5	0.552	0.048	0.034	0.033	0
7.5	0.478	0.070	0.064	0.029	0
8.5	0.499	0.092	0.087	0.030	0
9.5	0.677	0.118	0.111	0.041	0
11	0.609	0.124	0.119	0.037	0
		0–20%			
2.25	0.386	0.052	0.047	0.023	0
2.75	0.491	0.062	0.054	0.029	0
3.25	0.364	0.066	0.063	0.022	0
3.75	0.494	0.041	0.028	0.030	0
4.25	0.512	0.040	0.026	0.031	0
4.75	0.520	0.043	0.030	0.031	0
5.25	0.508	0.048	0.037	0.030	0
5.75	0.547	0.056	0.045	0.033	0
6.5	0.563	0.063	0.053	0.034	0
7.5	0.579	0.109	0.104	0.035	0
8.5	0.363	0.094	0.091	0.022	0
9.5	0.644	0.159	0.154	0.039	0
11	0.684	0.193	0.188	0.041	0
		20–40%			
2.25	0.416	0.057	0.051	0.025	0
2.75	0.517	0.068	0.060	0.031	0
3.25	0.425	0.077	0.072	0.025	0
3.75	0.467	0.042	0.031	0.028	0
4.25	0.470	0.041	0.029	0.028	0
4.75	0.447	0.043	0.033	0.027	0
5.25	0.524	0.057	0.048	0.031	0
5.75	0.539	0.062	0.053	0.032	0
6.5	0.543	0.069	0.060	0.033	0
7.5	0.545	0.119	0.114	0.033	0
8.5	0.546	0.119	0.115	0.033	0
9.5	0.495	0.206	0.204	0.030	0
11	1.046	0.277	0.269	0.063	0
		40–60%			
2.25	0.489	0.065	0.058	0.029	0
2.75	0.372	0.072	0.069	0.022	0
3.25	0.457	0.091	0.086	0.027	0
3.75	0.439	0.044	0.035	0.026	0
4.25	0.456	0.043	0.033	0.027	0
4.75	0.490	0.053	0.044	0.029	0
5.25	0.466	0.066	0.060	0.028	0
5.75	0.547	0.088	0.082	0.033	0
6.5	0.560	0.078	0.070	0.034	0

TABLE XIX. *(Continued.)*

p_T (GeV/c)	η/π^0	Tot. err.	Stat. err. + error A	Error B	Error C
7.5	0.528	0.160	0.157	0.032	0
8.5	0.598	0.200	0.197	0.036	0
9.5	0.495	0.234	0.232	0.030	0
11	0.243	0.211	0.210	0.015	0
		60–88%			
2.25	0.474	0.070	0.064	0.028	0
2.75	0.558	0.090	0.083	0.033	0
3.25	0.500	0.105	0.101	0.030	0
3.75	0.482	0.051	0.042	0.029	0
4.25	0.490	0.051	0.042	0.029	0
4.75	0.514	0.062	0.053	0.031	0
5.25	0.374	0.068	0.064	0.022	0
5.75	0.569	0.090	0.083	0.034	0
6.5	0.734	0.129	0.121	0.044	0
7.5	0.501	0.123	0.119	0.030	0
8.5	0.362	0.216	0.215	0.022	0
9.5	0.469	0.294	0.293	0.028	0

of the College of Arts and Sciences, Vanderbilt University (USA), Ministry of Education, Culture, Sports, Science, and Technology and the Japan Society for the Promotion of Science (Japan), Conselho Nacional de Desenvolvimento Científico e Tecnológico and Fundação de Amparo à Pesquisa do Estado de São Paulo (Brazil), Natural Science Foundation of China (People's Republic of China), Centre National de la Recherche Scientifique, Commissariat à l'Énergie Atomique, and Institut National de Physique Nucléaire et de Physique des Particules (France), Ministry of Industry, Science and Tekhnologies, Bundesministerium für Bildung und Forschung, Deutscher Akademischer Austausch Dienst, and Alexander von Humboldt Stiftung (Germany), Hungarian National Science Fund, OTKA (Hungary), Department of Atomic Energy (India), Israel Science Foundation (Israel), Korea Research Foundation and Korea Science and Engineering Foundation (Korea), Ministry of Education and Science, Rassia Academy of Sciences, Federal Agency of Atomic Energy (Russia), VR and the Wallenberg Foundation (Sweden), the US Civilian Research and Development Foundation for the Independent States of the Former Soviet Union, the US–Hungarian NSF-OTKA-MTA, and the US–Israel Binational Science Foundation.

TABLE XX. Ratio of η and π^0 in Au+Au collisions for different centrality classes, including minimum bias (0–92%), most central (0–20%), and most peripheral (60–92%).

p_T (GeV/c)	η/π^0	Tot. err.
	0–92% (MB)	
2.25	0.320	0.090 (28.1%)
2.75	0.410	0.120 (29.3%)
3.25	0.340	0.060 (17.6%)
3.75	0.290	0.058 (20.0%)
4.50	0.350	0.083 (23.7%)
5.50	0.350	0.072 (20.6%)
6.50	0.350	0.130 (37.1%)
7.50	0.560	0.100 (17.9%)
8.50	0.480	0.210 (43.8%)
9.50	0.490	0.250 (51.0%)
	0–20%	
2.25	0.400	0.120 (30.0%)
2.75	0.550	0.170 (30.9%)
3.25	0.370	0.110 (29.7%)
3.75	0.240	0.110 (45.8%)
4.50	0.360	0.110 (30.6%)
5.50	0.380	0.110 (28.9%)
6.50	0.350	0.160 (45.7%)
7.50	0.530	0.130 (24.5%)
8.50	0.470	0.240 (51.1%)
9.50	0.490	0.280 (57.1%)
	20–60%	
2.25	0.360	0.100 (27.8%)
2.75	0.340	0.100 (29.4%)
3.25	0.370	0.070 (18.9%)
3.75	0.340	0.066 (19.4%)
4.50	0.410	0.096 (23.4%)
5.50	0.490	0.096 (19.6%)
6.50	0.420	0.160 (38.1%)
7.50	0.430	0.098 (22.8%)
8.50	0.380	0.170 (44.7%)
9.50	0.400	0.200 (50.0%)
	60–92%	
2.25	0.312	0.094 (30.1%)
2.75	0.383	0.110 (28.7%)
3.25	0.404	0.081 (20.0%)
3.75	0.438	0.093 (21.2%)
4.50	0.542	0.139 (25.6%)
5.50	0.404	0.257 (63.6%)

APPENDIX: DATA TABLES

A. Invariant η cross sections ($p+p$, d+Au) and yields (Au+Au)

This appendix collects the data tables of the p_T spectra of η mesons measured at midrapidity in $p+p$, d+Au, and Au+Au collisions at $\sqrt{s_{NN}} = 200$ GeV. The invariant cross sections for η production in MB $p+p$ and d+Au collisions are tabulated in Tables XII and XIII, respectively. The invariant d+Au yields measured in centralities 0–20, 20–40, 40–60, and 60–88% are tabulated in Table XIV. Finally, the invariant yields in Au+Au reactions (MB and centralities 0–20, 20–60, and 60–92%) are presented in Tables XV. The quoted errors are categorized by type:

(i) (**A**) is a point-to-point error uncorrelated between p_T bins,
(ii) (**B**) is p_T correlated, all points move in the same direction but not by the same factor,
(iii) (**C**) is a normalization error in which all points move by the same factor independent of p_T.

B. Nuclear modification factors (d+Au, Au+Au)

We report in Tables XVI and XVII the $R_{AA}(p_T)$ η data tables for various centralities in d+Au and Au+Au collisions. The errors quoted are the point-to-point and absolute normalization ones. Note that there is an additional 9.7% overall normalization uncertainty (Run-3 $p+p$ BBC error, gray box in Fig. 19) not tabulated.

C. η/π^0 ratios ($p+p$, d+Au, Au+Au)

The ratio of η to π^0 invariant yields in $p+p$, d+Au, and Au+Au collisions at $\sqrt{s_{NN}} = 200$ GeV at midrapidity are tabulated in Tables XVIII, XIX, and XX. The data presented here are for minimum bias events and various centrality bins in d+Au and Au+Au collisions.

[1] See, e.g., G. Sterman *et al.* (CTEQ Collaboration), Rev. Mod. Phys. **67**, 157 (1995).
[2] W. M. Geist, D. Drijard, A. Putzer, R. Sosnowski, and D. Wegener, Phys. Rep. **197**, 263 (1990).
[3] G. Bunce, N. Saito, J. Soffer, and W. Vogelsang, Annu. Rev. Nucl. Part. Sci. **50**, 525 (2000).
[4] M. Arneodo, Phys. Rep. **240**, 301 (1994).
[5] N. Armesto, J. Phys. G **32**, R367 (2006).
[6] J. W. Cronin *et al.*, Phys. Rev. D **11**, 3105 (1975); D. Antreasyan, J. W. Cronin, H. J. Frisch, M. J. Shochet, L. Kluberg, P. A. Piroue, and R. L. Sumner, Phys. Rev. D **19**, 764 (1979).
[7] See, e.g., E. Iancu and R. Venugopalan, in *Quark-Gluon Plasma 3*, edited by R. C. Hwa and X. N. Wang (World Scientific, Singapore, 2004).
[8] B. Z. Kopeliovich, J. Nemchik, E. Predazzi, and A. Hayashigaki, Nucl. Phys. **A740**, 211 (2004).
[9] R. C. Hwa and C. B. Yang, Phys. Rev. C **70**, 024905 (2004).
[10] M. Gyulassy and M. Plümer, Phys. Lett. **B243**, 432 (1990); X. N. Wang and M. Gyulassy, Phys. Rev. Lett. **68**, 1480 (1992).
[11] R. Baier, Y. L. Dokshitzer, A. H. Mueller, S. Peigné, and D. Schiff, Nucl. Phys. **B484**, 265 (1997); R. Baier, D. Schiff, B. G. Zakharov, Annu. Rev. Nucl. Part. Sci. **50**, 37 (2000).
[12] M. Gyulassy, P. Lévai, and I. Vitev, Phys. Rev. Lett. **85**, 5535 (2000); Nucl. Phys. **B594**, 371 (2001).
[13] U. A. Wiedemann, Nucl. Phys. **B588**, 30 (2000); C. A. Salgado and U. A. Wiedemann, Phys. Rev. D **68**, 014008 (2003).
[14] S. S. Adler *et al.* (PHENIX Collaboration), Phys. Rev. Lett. **91**, 241803 (2003).
[15] S. S. Adler *et al.* (PHENIX Collaboration), Phys. Rev. Lett. **93**, 202002 (2004); Phys. Rev. Lett. **95**, 202001 (2005).
[16] S. S. Adler *et al.* (PHENIX Collaboration), Phys. Rev. Lett. **91**, 072303 (2003).
[17] S. S. Adler *et al.* (PHENIX Collaboration), nucl-ex/0610036.
[18] K. Adcox *et al.* (PHENIX Collaboration), Phys. Rev. Lett. **88**, 022301 (2002).
[19] S. S. Adler *et al.* (PHENIX Collaboration), Phys. Rev. Lett. **91**, 072301 (2003).
[20] S. S. Adler *et al.* (PHENIX Collaboration), Phys. Rev. Lett. **96**, 202301 (2006).
[21] S. S. Adler *et al.* (PHENIX Collaboration), Phys. Rev. C submitted; nucl-ex/0611007.
[22] S. Albino, B. A. Kniehl, and G. Kramer, Nucl. Phys. **B725**, 181 (2005).
[23] B. Jäger, A. Schäfer, M. Stratmann, and W. Vogelsang, Phys. Rev. D **67**, 054005 (2003); B. Jäger, M. Stratmann, S. Kretzer, and W. Vogelsang, Phys. Rev. Lett. **92**, 121803 (2004); A. Mukherjee, M. Stratmann, and W. Vogelsang, Phys. Rev. D **72**, 034011 (2005).
[24] C. Bourrely and J. Soffer, Eur. Phys. J. C **36**, 371 (2004).
[25] M. Anselmino, M. Boglione, U. D'Alesio, E. Leader, and F. Murgia, Phys. Rev. D **71**, 014002 (2005).
[26] K. J. Eskola, V. J. Kolhinen, and C. A. Salgado, Eur. Phys. J. C **9**, 61 (1999).
[27] D. de Florian and R. Sassot, Phys. Rev. D **69**, 074028 (2004).
[28] B. Z. Kopeliovich, Phys. Rev. C **68**, 044906 (2003).
[29] R. Vogt, Phys. Rev. C **70**, 064902 (2004).
[30] A. Accardi and M. Gyulassy, J. Phys. G **30**, S969 (2004); Phys. Lett. **B586**, 244 (2004).
[31] E. Cattaruzza and D. Treleani, Phys. Rev. D **69**, 094006 (2004).
[32] G. G. Barnaföldi, G. Papp, P. Lévai, and G. Fai, J. Phys. G **30**, S1125 (2004).
[33] J. L. Albacete, N. Armesto, A. Kovner, C. A. Salgado, and U. A. Wiedemann, Phys. Rev. Lett. **92**, 082001 (2004).
[34] E. Iancu, K. Itakura, and D. N. Triantafyllopoulos, Nucl. Phys. **A742**, 182 (2004).
[35] J. Jalilian-Marian and Y. V. Kovchegov, Prog. Part. Nucl. Phys. **56**, 104 (2006).
[36] See, e.g., D. d'Enterria, AIP Conf. Proc. **806**, 252 (2006).
[37] I. Vitev and M. Gyulassy, Phys. Rev. Lett. **89**, 252301 (2002); I. Vitev I, J. Phys. G **30**, S791 (2004).
[38] K. J. Eskola, H. Honkanen, C. A. Salgado, and U. A. Wiedemann, Nucl. Phys. **A747**, 511 (2005).
[39] A. Dainese, C. Loizides, and G. Paic, Eur. Phys. J. C **38**, 461 (2005).
[40] R. C. Hwa and C. B. Yang, Phys. Rev. C **67**, 034902 (2003); R. J. Fries, B. Müller, C. Nonaka, and S. A. Bass, Phys. Rev. Lett. **90**, 202303 (2003); V. Greco, C. M. Ko, and P. Lévai, Phys. Rev. Lett. **90**, 202302 (2003).
[41] S. S. Adler *et al.* (PHENIX Collaboration), Phys. Rev. C **69**, 034910 (2004).
[42] C. Kourkoumelis *et al.* (AFS Collaboration), Phys. Lett. **B84**, 271 (1979); Phys. Lett. **B84**, 277 (1979).
[43] F. Abe *et al.* (CDF Collaboration), Phys. Rev. D **48**, 2998 (1993).
[44] F. Ellinghaus and J. Seele (PHENIX Collaboration), RIKEN Accel. Prog. Rep. 39 (2006); F. Ellinghaus (PHENIX Collaboration), hep-ex/0612031 (to appear in the proceedings of the 17th International Spin Physics Symposium, SPIN 2006).
[45] J. Adams *et al.* (STAR Collaboration), Phys. Rev. Lett. **91**, 172302 (2003).
[46] K. Adcox *et al.* (PHENIX Collaboration), Phys. Rev. Lett. **88**, 192303 (2002); S. S. Adler *et al.* (PHENIX Collaboration), Phys. Rev. C **72**, 024901 (2005); S. S. Adler *et al.* (PHENIX Collaboration), Phys. Rev. Lett. **96**, 032301 (2006); A. Adare *et al.* (PHENIX Collaboration), nucl-ex/0611018.
[47] A. Toia (PHENIX Collaboration), Nucl. Phys. **A774**, 743 (2006).

[48] S. S. Adler *et al.* (PHENIX Collaboration), Phys. Rev. Lett. **94**, 232301 (2005).
[49] S. S. Adler *et al.* (PHENIX Collaboration), Phys. Rev. D **71**, 071102 (2005); S. S. Adler *et al.* (PHENIX Collaboration), Phys. Rev. Lett. **98**, 012002 (2007).
[50] H. Hahn *et al.*, Nucl. Instrum. Methods A **499**, 245 (2003).
[51] K. Adcox *et al.* (PHENIX Collaboration), Nucl. Instrum. Methods A **499**, 469 (2003).
[52] L. Aphecetche *et al.* (PHENIX Collaboration), Nucl. Instrum. Methods A **499**, 521 (2003).
[53] K. Adcox *et al.* (PHENIX Collaboration), Nucl. Instrum. Methods A **499**, 489 (2003).
[54] K. Adcox *et al.*, Nucl. Instrum. Methods A **497**, 263 (2003).
[55] M. Allen *et al.* (PHENIX Collaboration), Nucl. Instrum. Methods A **499**, 549 (2003).
[56] C. Adler *et al.*, Nucl. Instrum. Methods A **470**, 488 (2001).
[57] S. Eidelman *et al.* (Particle Data Group), Phys. Lett. **B592**, 1 (2004).
[58] M. Aizawa *et al.*, Nucl. Instrum. Methods A **499**, 508 (2003).
[59] S. S. Adler *et al.* (PHENIX Collaboration), Phys. Rev. Lett. **94**, 082302 (2005).
[60] K. Adcox *et al.* (PHENIX Collaboration), Phys. Rev. Lett. **86**, 3500 (2001).
[61] S. White, AIP Conf. Proc. **792**, 527 (2005).
[62] F. Carminati *et al.*, GEANT 3.21: Detector Description and Simulation Tool, CERN Program Library Long Writeup W5013, 1993.
[63] S. S. Adler *et al.* (PHENIX Collaboration), Phys. Rev. Lett. **96**, 012304 (2006).
[64] T. Sjöstrand, Comput. Phys. Commun. **82**, 74 (1994).
[65] C. Alff *et al.*, Phys. Rev. Lett. **9**, 325 (1962).
[66] J. S. Danburg *et al.*, Phys. Rev. D **2**, 2564 (1970).
[67] S. Giovanella (KLOE Collaboration), *Proceedings of "La Thuile 2005, Results and perspectives in particle Physics," pp. 241–248, 2005*; hep-ex/0505074.
[68] G. D. Lafferty and T. R. Wyatt, Nucl. Instrum. Methods A **355**, 541 (1995).
[69] V. Guzey, M. Strikman, and W. Vogelsang, Phys. Lett. **B603**, 173 (2004).
[70] S. S. Adler *et al.* (PHENIX Collaboration), Phys. Rev. C **73**, 054903 (2006).
[71] L. E. Gordon and W. Vogelsang, Phys. Rev. D **48**, 3136 (1993); Phys. Rev. D **50**, 1901 (1994); P. Aurenche *et al.*, Phys. Lett. **B140**, 87 (1984); Nucl. Phys. **B297**, 661 (1988).
[72] T. Sjöstrand, P. Eden, C. Friberg, L. Lonnblad, G. Miu, S. Mrenna, and E. Norrbin, Comput. Phys. Commun. **135**, 238 (2001).
[73] D. d'Enterria, J. Phys. G **31**, S491 (2005).
[74] B. Andersson, G. Gustafson, G. Ingelman, and T. Sjöstrand, Phys. Rep. **97**, 31 (1983).
[75] B. Andersson, *The Lund Model* (Cambridge University Press, 1997), p. 1.
[76] T. Sjöstrand, L. Lonnblad, S. Mrenna, and P. Skands, hep-ph/0308153.
[77] M. Bourquin and J.-M. Gaillard, Nucl. Phys. **B114**, 334 (1976).
[78] S. S. Adler *et al.* (PHENIX Collaboration), Phys. Rev. C **74**, 024904 (2006).
[79] G. J. Donaldson *et al.*, Phys. Rev. Lett. **40**, 684 (1978).
[80] M. Bonesini *et al.* (WA70 Collaboration), Z. Phys. C **42**, 527 (1989).
[81] J. Antille *et al.* (UA6 Collaboration), Phys. Lett. **B194**, 568 (1987).
[82] M. Aguilar-Benitez *et al.* (NA27 Collaboration), Z. Phys. C **50**, 405 (1991).
[83] E. Amaldi *et al.*, Nucl. Phys. **B158**, 1 (1979).
[84] L. Apanasevich *et al.* (Fermilab E706 Collaboration), Phys. Rev. D **68**, 052001 (2003).
[85] T. Akesson *et al.* (AFS Collaboration), Phys. Lett. **B158**, 282 (1985).
[86] T. Akesson *et al.* (AFS Collaboration), Phys. Lett. **B178**, 447 (1986).
[87] T. Akesson *et al.* (AFS Collaboration), Z. Phys. C **18**, 5 (1983).
[88] M. Banner *et al.* (UA2 Collaboration), Z. Phys. C **27**, 329 (1985).
[89] J. Povlis *et al.* (Fermilab E629 Collaboration), Phys. Rev. Lett. **51**, 967 (1983).
[90] S. W. Delchamps, FERMILAB-THESIS-1985-35 (1985).
[91] G. Agakishiev *et al.* (TAPS/CERES Collaboration), Eur. Phys. J. C **4**, 249 (1998).
[92] V. Tikhomirov (HELIOS Collaboration), HADRON 95, Proceedings of the 6th International Conference on Hadron Spectroscopy, Manchester, England, 10–14 Jul 1995 (World Scientific Publishing, Singapore, 1995).
[93] G. Alverson *et al.* (Fermilab E706 Collaboration), Phys. Rev. D **48**, 5 (1993).
[94] L. Apanasevich *et al.* (Fermilab E706 Collaboration), Phys. Rev. D **69**, 032003 (2004).
[95] R. Averbeck *et al.* (TAPS Collaboration), Z. Phys. A **359**, 65 (1997).
[96] R. Averbeck, R. Holzmann, V. Metag, and R. S. Simon, Phys. Rev. C **67**, 024903 (2003).
[97] M. M. Aggarwal *et al.* (WA98 Collaboration), nucl-ex/0006007.
[98] R. Albrecht *et al.* (WA80 Collaboration.), Phys. Lett. **B361**, 14 (1995).
[99] R. Hagedorn, Riv. Nuovo Cimento **6N10**, 1 (1984).
[100] K. Adcox *et al.* (PHENIX Collaboration), Nucl. Phys. **A757**, 184 (2005).
[101] R. Witt (STAR Collaboration), nucl-ex/0403021.
[102] T. Peitzmann, nucl-th/0511022.
[103] D. Buskulic *et al.* (ALEPH Collaboration), Phys. Lett. **B292**, 210 (1992).
[104] R. Barate *et al.* (ALEPH Collaboration), Z. Phys. C **74**, 451 (1997).
[105] R. Barate *et al.* (ALEPH Collaboration), Phys. Rep. **294**, 1 (1998).
[106] R. Barate *et al.* (ALEPH Collaboration), Eur. Phys. J. C **16**, 613 (2000).
[107] A. Heister *et al.* (ALEPH Collaboration), Phys. Lett. **B528**, 19 (2002).
[108] W. Adam *et al.* (DELPHI Collaboration), Z. Phys. C **69**, 561 (1996).
[109] B. Adeva *et al.* (L3 Collaboration), Phys. Lett. **B259**, 199 (1991).
[110] O. Adriani *et al.* (L3 Collaboration), Phys. Lett. **B286**, 403 (1992).
[111] M. Acciarri *et al.* (L3 Collaboration), Phys. Lett. **B328**, 223 (1994).
[112] K. Ackerstaff *et al.* (OPAL Collaboration), Eur. Phys. J. C **5**, 411 (1998).

[113] G. Abbiendi *et al*. (OPAL Collaboration), Eur. Phys. J. C **17**, 373 (2000).
[114] G. Wormser *et al*., Phys. Rev. Lett. **61**, 1057 (1988).
[115] S. Abachi *et al*. (HRS Collaboration), Phys. Lett. **B205**, 111 (1988).
[116] W. Bartel *et al*. (JADE Collaboration), Phys. Lett. **B130**, 454 (1983).
[117] W. Bartel *et al*. (JADE Collaboration), Z. Phys. C **28**, 343 (1985).
[118] D. Pitzl *et al*. (JADE Collaboration), Z. Phys. C **46**, 1 (1990); [Erratum-*ibid*. **47**, 676 (1990)].
[119] H. J. Behrend *et al*. (CELLO Collaboration), Z. Phys. C **47**, 1 (1990).
[120] C. Peterson and T. F. Walsh, Phys. Lett. **B91**, 455 (1980).
[121] P. Ball, J. M. Frere, and M. Tytgat, Phys. Lett. **B365**, 367 (1996).
[122] H. Fritzsch, Phys. Lett. **B415**, 83 (1997).
[123] J. Binnewies, B. A. Kniehl, and G. Kramer, Phys. Rev. D **52**, 4947 (1995).
[124] B. A. Kniehl, G. Kramer, and B. Pötter, Nucl. Phys. **B582**, 514 (2000).
[125] S. Kretzer, Phys. Rev. D **62**, 054001 (2000).
[126] L. Bourhis, M. Fontannaz, J. P. Guillet, and M. Werlen, Eur. Phys. J. C **19**, 89 (2001).
[127] M. Greco and S. Rolli, Z. Phys. C **60**, 169 (1993); M. Greco, S. Rolli, and A. Vicini, Z. Phys. C **65**, 277 (1995); S. Rolli, *Proceedings of 31st Rencontres de Moriond: QCD and High-Energy Hadronic Interactions, Les Arcs, France, 23–30 March 1996*; hep-ph/9607480.
[128] D. Indumathi, H. S. Mani, and A. Rastogi, Phys. Rev. D **58**, 094014 (1998). Note that in the second case, the η FF is not explicitly given, but within the framework it could be derived from the FF parameters for other octet mesons.
[129] S. S. Adler (PHENIX Collaboration), Phys. Rev. D **74**, 072002 (2006).
[130] S. Kretzer, Acta Phys. Polon. B **36**, 179 (2005).